

Understanding Device Performance of  
Blue Organic Light-Emitting Diodes  
with Fluorescent and Phosphorescent  
Emitters

UNDERSTANDING DEVICE PERFORMANCE  
OF BLUE ORGANIC LIGHT-EMITTING  
DIODES WITH FLUORESCENT AND  
PHOSPHORESCENT EMITTERS

BY  
BO MI LEE, B.S.E.

A thesis  
Submitted to the School of Graduate Studies  
in Partial Fulfilment of the Requirements  
for the Degree of  
Doctor of Philosophy

McMaster University  
© Copyright by Bo Mi Lee, Dec 2019

Doctor of Philosophy (2019)

McMaster University

(Engineering Physics)

Hamilton, Ontario

**TITLE:** Understanding Device Performance of Blue Organic  
Light- Emitting Diodes with Fluorescent and  
Phosphorescent Emitters

**AUTHOR:** Bo Mi Lee  
B.S.E., (Hoseo University)

**SUPERVISOR:** Dr. Peter Mascher

**NUMBER OF PAGES:** xix, 149

*This work is dedicated to my family*

# Abstract

This thesis proposes blue organic light-emitting diodes (OLEDs) composed of fluorescent and phosphorescent emitting layers (EMLs) and the study was accomplished by engineering device architecture and dopant distribution in the EMLs. We investigated the electrical and optical properties when both types of emitters are applied as EMLs into a single device and determined the emission ratio and contribution between fluorescent and phosphorescent emitters by deconvoluting electroluminescent spectra with Gaussian fitting. The fluorescent EML is composed of 4,4'-bis(2,2'-diphenylvinyl)-1,1'-diphenyl (DPVBi) doped with 4,4'-bis(9-ethyl-3-carbazovinylene)-1,1'-biphenyl (BCzVBi) while Bis[2-(4,6-difluorophenyl)pyridinato-C<sub>2</sub>,N](picolinato)iridium(III) (FIrpic) is doped into 1,3-Bis(N-carbazolyl)benzene (mCP) for the phosphorescent EML.

Firstly, dual-EML blue OLEDs are introduced and differentiated by doping styles, doping concentration and device structure to study the operating principles and changes in the efficiency and color characteristic in blue OLEDs. When both types of EMLs are used, the predominant emission is phosphorescence and the relative intensity of fluorescent and phosphorescent emission is controlled by the fluorescent doping concentration. With the incorporation of a step-graded doping profile in the EMLs, the trend of device performance is indicative of the effect of the location of the non-doped area. Blue OLEDs with the step-controlled doping concentration showed higher device efficiency and strengthened emission from fluorescence compared to the uniformly doped devices.

Secondly, triple-EML blue OLEDs with the various combinations of EML host configurations were studied. The electroluminescent spectra of the devices were deconvoluted by Gaussian peak fitting to understand the origin of blue emission. The device performance is strongly influenced by the location of the n-type host material. Furthermore, effects of interlayer and EML thickness variation in devices were investigated to optimize device efficiency and color emission.

# Acknowledgements

I would like to express my sincere gratitude to all those who supported my research.

I would like to firstly thank my supervisor, Dr. Peter Mascher, for all his support and encouragement. Your guidance and advice helped me to develop the direction for research.

I would like to thank my supervisory committee members, Dr. John Preston and Dr. Asye Turak for their helpful advice and feedback for my research work. I also would like to thank Dr. Kim for giving me warm words and supporting experiments in Korea. I also want to acknowledge my research group members and collaborators in Dr. Kim's lab. I would like to thank all the past and present members of Mascher's research group for inspiring me and sharing their valuable experience with me, which was helpful during my PhD program.

My sincere thanks goes to my friends. I am very fortunate to have wonderful friends who I can share a lot of thoughts in many different but good ways. My special thanks goes to my boyfriend, Geoff White. Without you my life in Canada would not be easy. Your love and all the good words let me stay strong.

During my long journey at school my family was one of my motivations and encouraged me to keep running to the end. I always thank my family for their unconditional love and support. I would not be able to make this accomplishment without your support and encouragement. Last but not least, thank God for being with me all the time.

# Contents

<b>List of Figures</b> .....	<b>xi</b>
<b>List of Tables</b> .....	<b>xviii</b>
<b>1. Introduction and Thesis Overview</b> .....	<b>1</b>
<b>1.1 Introduction</b> .....	<b>1</b>
<b>1.2 History of OLEDs</b> .....	<b>4</b>
<b>1.3 Objectives and Outline of the Thesis</b> .....	<b>6</b>
<b>1.4 Contributions to Knowledge</b> .....	<b>9</b>
1.4.1 Peer reviewed Journal Papers .....	10
1.4.2 Conference Proceeding Papers.....	11
1.4.3 Conference Presentations .....	12
<b>2. Fundamental Principles of Organic Light Emitting Diodes</b> .....	<b>13</b>
<b>2.1 Electronic Properties of Organic Materials</b> .....	<b>14</b>
<b>2.2 Working Principles of OLEDs</b> .....	<b>16</b>
<b>2.3 Excitons</b> .....	<b>18</b>
<b>2.4 Photophysical Processes in OLEDs</b> .....	<b>20</b>
2.4.1 Jablonski Diagram .....	20
2.4.2 Non-radiative Transitions .....	21
2.4.3 Radiative Transitions .....	21
2.4.4 Energy Transfer .....	22



2.4.4.1 Förster Energy Transfer .....	23
2.4.4.2 Dexter Energy Transfer.....	26
<b>2.5 Exciton Quenching Mechanism .....</b>	<b>26</b>
<b>2.6 Electrical Properties of OLEDs .....</b>	<b>27</b>
2.6.1 Charge Carrier Injection .....	28
2.6.2 Charge Carrier Transport .....	30
2.6.3 Charge Trapping .....	33
2.6.4 Recombination of Excitons .....	33
<b>3. Experimental Methods and Performance Metrics.....</b>	<b>34</b>
<b>3.1 Sample Preparation .....</b>	<b>34</b>
3.1.1 Cleaning ITO glasses .....	34
3.1.2 Plasma Treatment for ITO Glass Substrates .....	36
<b>3.2 Thermal Evaporation of Organic Layers .....</b>	<b>37</b>
3.2.1 Organic Material Deposition.....	37
3.2.2 Metal Deposition.....	38
3.2.3 Encapsulation.....	39
<b>3.3 Measurements of Electrical and Optical Properties .....</b>	<b>39</b>
3.3.1 UV-Vis Absorption and Photoluminescence .....	39
3.3.2 J-V-L Characteristics and Electroluminescence .....	41
<b>3.4 Efficiency Metrics .....</b>	<b>42</b>
<b>3.5 CIE Color Coordinates .....</b>	<b>44</b>
<b>4. Material Selection and Material Properties of Fluorescent and Phosphorescent Emitters.....</b>	<b>47</b>
<b>4.1 Materials Selection for OLED Device Fabrication .....</b>	<b>48</b>

<b>4.2 Materials Properties of Blue Emitting Materials .....</b>	<b>51</b>
4.2.1 4,4 -bis(2,2 -diphenylvinyl)-1,1 –diphenyl (DPVBi).....	51
4.2.2 4 ,4'-Bis(2-(9-ethyl-9H-carbazol-3-yl)vinyl)-1,1'-biphenyl (BCzVBi) .....	53
4.2.3 Bis[2-(4,6-difluorophenyl)pyridinato-C2,N](picolinato)iridium(III) (FIrpic)	
.....	56
<b>5. Blue OLEDs with Either Uniformly or Step-Controlled Doping Strategies in</b>	
<b>Double EMLs.....</b>	<b>59</b>
<b>5.1 Introduction .....</b>	<b>60</b>
<b>5.2 Uniformly Doped EMLs for Blue OLEDs .....</b>	<b>62</b>
5.2.1 Device Fabrication: Device Structures and Doping Profiles .....	62
5.2.2 Effects of Fluorescent Doping Concentrations .....	65
5.2.2.1 Characterizations of the F-P EML Structure .....	66
5.2.2.2 Characterizations of the P-F EML Structure .....	73
5.2.3 Effects of Different Electron Transport Layers (ETLs).....	82
5.2.4 Brief Summary of Blue OLEDs with Uniformly Doped Double EMLs.....	85
<b>5.3 Step-Controlled Doped EMLs for Blue OLEDs .....</b>	<b>86</b>
5.3.1 Device Fabrication: Device Structures and Doping Profiles .....	86
5.3.2 Analysis of Electroluminescent Spectra .....	88
5.3.3 Electrical and Optical Properties .....	95
5.3.4 Brief Summary of Blue OLEDs with Step-controlled Doping Profiles.....	103
<b>6. Various Host Combinations in Triple Emitting Layers for Blue OLEDs .....</b>	<b>104</b>
<b>6.1 Introduction .....</b>	<b>105</b>
<b>6.2 Device Fabrication: Device Structures and Doping Profiles .....</b>	<b>106</b>
<b>6.3 Characterization of Devices with Various Host Combinations .....</b>	<b>107</b>

6.3.1 Deconvoluted EL Spectra for Understanding the Origin of Emission .....	107
6.3.2 Electrical and Optical Properties .....	114
6.3.3 Effects of Different EML Thicknesses in the p-F-n EML Structure .....	118
6.3.4 Effects of mCP Interlayers in the p-F-n EML Structure .....	119
<b>6.4 Summary .....</b>	<b>121</b>
<b>7. Conclusions and Suggestions for Future Study.....</b>	<b>122</b>
<b>7.1 Conclusions .....</b>	<b>122</b>
<b>7.2 Suggestions for Future Study.....</b>	<b>124</b>
7.2.1 Device Characterization Relative to the Presented Research .....	124
7.2.2 Material Selection .....	125
7.2.3 The Adoption for White OLEDs .....	127

## **References**

# List of Figures

Figure 1.1	Various OLED applications available in the marketplace: (a) 55-inch OLED television, (b) screens for mobile phones and (c) smart watches (photo credit: LG Display, Samsung and Apple).	3
Figure 1.2	(a) Schematic diagram of the first double-layered OLED device structure and molecular structures of the organic materials used. The detailed structure of the device consists of indium tin oxide (ITO) (120 nm)/ Diamine (75 nm)/ Alq <sub>3</sub> (60 nm)/ Mg:Ag (100 nm). (b) Schematic diagram of the first PLED and the molecular structure of the conjugated polymer. The detailed device structure consists of ITO/ PPV (70 nm)/ Al.	5
Figure 2.1	Configurations of sp <sup>2</sup> hybridization in ethene showing $\sigma$ and $\pi$ bonding between the two neighboring carbon atoms.	14
Figure 2.2	Formation of bonding and anti-bonding molecular orbitals and energy bands.	15
Figure 2.3	Schematic illustration of a three-layer bottom emitting OLED and its operating mechanism under a forward bias: (1) electrons and holes are injected from the cathode and anode, respectively. (2) Electrons and holes are transported toward the EML by hopping between molecules. (3) Electrons and holes recombine and create excitons at the EML and (4) excitons radiatively decay as photons which are extracted at the anode side. $\Phi_C$ and $\Phi_A$ are cathode and anode work functions, respectively.	17
Figure 2.4	Schematic illustrations of three types of excitons from the spatial size viewpoint: (1) Frenkel exciton, (2) Wannier-Mott exciton and (3) intermediate charge-transfer exciton.	18
Figure 2.5	Spin states for singlet and triplet excitons with total spin quantum numbers (S) and magnetic quantum numbers (M <sub>s</sub> ).	19

Figure 2.6	Jablonski diagram showing vibrational and electronic energy states and possible transitions in an organic molecule. Each sublevel of vibrational states corresponds to a manifold of rotational and translational levels with $\sim 0.01$ eV spacing.	20
Figure 2.7	Schematic representations of (a) Förster and (b) Dexter energy transfer.	25
Figure 2.8	Schematic illustrations of (a) the energy barrier height ( $\phi_B = E_{\text{LUMO}} - E_f$ ) without any effects at the interface (b) Richardson-Schottky model with image force lowering ( $E_b = \phi_b - \Delta\varphi$ ) and (c) Fowler-Nordheim model. $E_f$ is the Fermi-level of the metal, $\Delta\varphi = \sqrt{q^3 F(0) /4\pi\epsilon}$ and $x$ is the tunneling distance.	29
Figure 2.9	Schematic illustrations for charge transport models: (a) band transport model for highly ordered inorganic materials, and (b) hopping model for highly disordered organic materials.	30
Figure 2.10	Log J-log V characteristics in three different regimes dependent on the applied voltage.	32
Figure 3.1	Schematic diagrams of the top view of the device in order of fabrication: (a) pre-coated ITO glass, (b) after organic material deposition on the ITO, (c) the metallic cathode layer deposition and (d) fabricated device with 4 emissive pixels.	35
Figure 3.2	(a) OLED fabrication system and (b) the internal feature of the organic deposition chamber.	38
Figure 3.3	The (a) front and (b) back side of the completed OLED device.	39
Figure 3.4	The absorption and PL spectra of red emitting material, 5,6,11,12-tetraphenyltetracene (Rubrene).	40
Figure 3.5	(a) J-V-L measurement setup, (b) jig to hold samples and (c) an emissive device when the voltage is applied.	42
Figure 3.6	The color matching functions of the CIE 1931 color system.	45

Figure 3.7	CIE 1931 chromaticity diagram of the common standard illuminants. The solid line indicates monochromatic colors with the corresponding wavelengths. The standard white emission is represented at (0.33, 0.33).	46
Figure 4.1	The absorption and PL spectra of DPVBi and an EL spectrum from a DPVBi-based device (ITO/ NPB (70 nm)/ DPVBi (30 nm)/ BPhen (30 nm)/ Liq/ Al).	52
Figure 4.2	Absorption and PL spectra of BCzVBi and PL spectrum of DPVBi.	53
Figure 4.3	The EL spectrum of a BCzVBi-doped device with the structure of ITO/NPB (70 nm)/ DPVBi:BCzVBi (15 %, 30 nm)/ BPhen (30 nm)/ Liq/ Al.	54
Figure 4.4	(a) Power efficiency and (b) luminous efficiency of DPVBi-based and BCzVBi-doped devices. The structure of the DPVBi-based device is ITO/ NPB (70 nm)/ DPVBi (30 nm)/ BPhen (30 nm)/ Liq/ Al and that of the BCzVBi-doped device is ITO/ NPB (70 nm)/ DPVBi:BCzVBi (15 %, 30 nm)/ BPhen (30 nm)/ Liq/ Al.	55
Figure 4.5	PL quantum efficiency as a function of dopant concentration in CBP:FIrpic [filled squares] and mCP:FIrpic [open squares] films. The inset shows PL spectra of CBP:FIrpic measured at given dopant concentrations from 1.4 ~74 mol%.	57
Figure 4.6	The absorption and PL spectra of FIrpic and the mCP PL spectrum. The inset shows possible energy transfer processes between mCP and FIrpic.	58
Figure 5.1	Energy level diagrams of organic layers in the blue OLEDs with BA1q as the ETL (a) F-P structure and (b) P-F structure. The dashed line indicates the energy levels of dopant materials and the numbers are HOMO and LUMO energy levels of given materials.	63

Figure 5.2	Various hopping cases in disordered host-dopant (guest) system. (a) Hopping between host molecules (no influence of dopant molecules), (b) hopping via host molecules coexisting with a small portion of dopant molecules (trap-limited transport), (c) hopping via both host and dopant molecules, and (d) hopping mainly via dopant molecules. The densities of states (DOS) of host (solid lines) and dopant (dotted lines) are also shown (left side of each panel).	66
Figure 5.3	Current density and luminance of device set A1 as a function of voltage.	67
Figure 5.4	Luminous efficiency from device set A1 as a function of current density. The reference luminous efficiency is achieved from the blue fluorescent OLED with a single EML (DPVBi:BCzVBi (15 %)) as given in Figure 4.5 (b).	69
Figure 5.5	(a) EL spectra of device set A1 at 6 V (the inset is plotted from 420 nm to 456 nm) and (b) EL spectra of device A1-4 as a function of voltage (the inset is the normalized EL intensity at 448 nm of device set A1 as a function of voltage).	71
Figure 5.6	(a) CIE <sub>x</sub> and (b) CIE <sub>y</sub> color coordinates as a function of bias voltage and (c) CIE <sub>xy</sub> changes from 5 V to 10 V of devices A1-1 to A1-4.	72
Figure 5.7	(a) Current density and (b) luminance of devices B1-1 to B1-4 as a function of the applied voltage.	74
Figure 5.8	Luminous efficiency of devices B1-1 to B1-4 as a function of current density (Inset: luminous efficiency at current densities higher than 5 mA/cm <sup>2</sup> on a Log scale). The reference luminous efficiency is achieved from the blue fluorescent OLED with the single EML (DPVBi:BCzVBi (15 %)) as shown in Figure 4.5 (b).	76
Figure 5.9	(a) EL spectra of devices B1-1 to B1-4 at 6 V (inset is plotted from 420 nm to 456 nm) and (b) EL spectra of device B1-4 as a function of voltage (The top and bottom insets are the EL intensity at 448 nm and 496 nm, respectively).	78

Figure 5.10	(a) CIE <sub>x</sub> and (b) CIE <sub>y</sub> color coordinates as a function of bias voltage of devices B1-1 to B1-4.	79
Figure 5.11	(a) Current density and luminance of devices A1-4 and B1-4 as a function of the driving voltage and (b) luminous efficiency of devices A1-4 and B1-4 as a function of current density.	82
Figure 5.12	(a) J-V-L characteristics, (b) luminous efficiency (on a semi-log scale), (c) EL spectra at 6 V and (d) CIE <sub>xy</sub> color coordinates of devices with different electron transport materials, TPBi (black) and BAlq (red).	84
Figure 5.13	(a) Energy level diagrams of organic layers in blue OLEDs and (b) doping profiles of the P-EML in devices C1-1 to C1-6.	86
Figure 5.14	EL spectra at 8 V from fluorescent (a) and phosphorescent (b) blue OLEDs. The inset are schematic diagrams of device structures of the fluorescent and phosphorescent OLEDs and whose EML compositions are DPVBi doped with BCzVBi (15 %) and mCP doped with FIrpic (8 %), respectively. Their common emission peak lies at 472 nm.	89
Figure 5.15	EL spectra of devices C1-1 to C 1-6 under the different applied voltages.	90
Figure 5.16	CIE color coordinates of devices C1-1 to C1-6 and BCzVbi- and FIrpic-doped devices at 6 V. The BCzVbi- and FIrpic-doped device structures are given in Figure 5.13.	92
Figure 5.17	EL spectra of devices (a) C1-1 and (b) C1-2 at 8 V. The blue dashed lines are cumulative spectra of fluorescent and phosphorescent reference devices.	94
Figure 5.18	Current density as a function of applied voltage from reference samples 1 and 2 (the reference devices have the same device structure: ITO/ NPB/ mCP:FIrpic (0 % or 8 %)/ DPVBi:BCzVBi/ TPBi/ Liq/ Al)	96
Figure 5.19	(a) Current density and (b) luminance versus the applied voltage of devices C1-1 to C1-6.	97



Figure 5.20	Luminous efficiency as a function of (a) current density and (b) luminance (The dotted vertical lines indicate 50 mA/cm <sup>2</sup> , 1,000 and 6,000 cd/m <sup>2</sup> )	100
Figure 6.1	The deconvoluted EL spectrum by Gaussian peak fitting of (a) a FIrpic-doped OLED with the structure: ITO/ NPB (70 nm)/ mCP:FIrpic (30 nm, 8 %)/ TPBi (30 nm)/ Liq (2 nm)/ Al.	108
Figure 6.2	The deconvoluted EL spectrum by Gaussian peak fitting of a BCzVBi-doped OLED with the structure: ITO/ NPB (70 nm)/ DPVBi:BCzVBi (30 nm, 15 %)/ TPBi (30 nm)/ Liq (2 nm)/ Al.	109
Figure 6.3	(a)-(d) EL spectra of devices E1-1 to E1-4 at 6, 8 and 10 V, respectively and (e)-(h) Gaussian peak fitting of each device at 10 V. The dotted lines in the Gaussian peak fitting indicate the Gaussian peaks at 6 V.	110
Figure 6.4	(a) PL spectra of NPB and NPB:TPBi (1:1) films and EL spectrum of the device whose structure is ITO /NPB (30 nm) /NPB:TPBi (35 nm)/ TPBi (35 nm)/LiF (1 nm)/Al(100 nm). (b) Time-resolved spectra from NPB:TPBi (1:1) film excited with 355 nm pulsed laser and recorded with gated intensified charged coupled device (iCCD) camera. Indicated numbers are camera opening times after excitation in nanoseconds (delay time), the integration times are ~1/10th of the delay time.	111
Figure 6.5	Comparison of EL spectra between the phosphorescent emitter only devices and E1-4. The EML structure of Ref. 1 is mCP:FIrpic (8 %)/ CBP:FIrpic (8 %)/ TPBi:FIrpic (8 %) while that of Ref. 2 is TPBi:FIrpic (8 %)/ CBP:FIrpic (8 %)/ mCP:FIrpic (8 %).	112
Figure 6.6	(a) CIE <sub>x</sub> and (b) CIE <sub>y</sub> color coordinates as a function of bias voltage and (c) CIE <sub>xy</sub> changes from 5 V to 10 V of devices E1-1 to E1-4.	113
Figure 6.7	Current density and luminance as a function of voltage from devices E1-1 to E1-4.	115
Figure 6.8	Luminous efficiency of devices E1-1 to 1-4 and Ref. 1. The EML structure of Ref. 1 is given in Figure 6.5.	117

Figure 6.9	(a) J-V-L characteristics, (b) luminous efficiency (c) EL spectra at 6 and 10 V and (d) CIE <sub>xy</sub> coordinates as a function of voltage of devices with even EML thickness (black) and E1-1 (red).	118
Figure 6.10	(a) J-V-L characteristics, (b) luminous efficiency and (c) EL spectra at 8 V and (d) CIE <sub>xy</sub> coordinates of devices E1-1 with (red) or without (black) the interlayer, mCP.	120
Figure 7.1	(a) Schematic energy level diagram of CCT tunable white OLED by Jou's group and (b) EL spectra of the given device from 4 V to 9 V on 1 V interval (The CCT changed from 1,500 K to 4,200 K).	129

## List of Tables

Table 2.1	Available energy transfer processes between the host and dopant molecules. The excited state is denoted with an asterisk (*) and the number represents spin multiplicities.	25
Table 4.1	List of organic materials that have been employed in this work for OLED fabrication.	49
Table 4.2	Summary of spectral data of DPVBi.	52
Table 4.3	Current density and device efficiency of DPVBi-based and BCzVBi-doped devices at 6 V.	55
Table 5.1	Doping profiles of blue OLEDs with F-P (devices A) and P-F (devices B) EML structures.	64
Table 5.2	J-V-L results and efficiencies of device set A1 (w/ F-P EML structure). The values of current density and luminance were measured at 10 V.	68
Table 5.3	CIE <sub>xy</sub> color coordinates of device set A1 at 6 V and their variations when the voltage changes from 5 V to 10 V.	73
Table 5.4	J-V-L characteristics and efficiencies of devices in set B1 (w/ P-F EML structure). The values of current density and luminance were measured at 10 V.	75
Table 5.5	CIE <sub>xy</sub> color coordinates of device set B1 at 6 V and their changes when the voltage changes from 5 to 9 V and 9 to 10.5 V.	80
Table 5.6	EL performance of blue OLEDs with the BA1q and TPBi.	83
Table 5.7	The step-controlled doping profiles in each device.	87
Table 5.8	The EL intensity at 448 nm and CIE <sub>xy</sub> coordinates of each device at 6 and 10 V.	91
Table 5.9	Fraction of fluorescence ( $C_F$ ) and phosphorescence ( $C_P$ ) of devices C1-1 to C1-4 at 8 V.	95
Table 5.10	Average and standard deviations in device performance including current density, turn-on and operating voltages and luminance.	98

Table 5.11	Summary of luminous efficiency and roll-off in luminous efficiency for devices C1-1 to C1-6.	99
Table 6.1	List of triple EML structures.	107
Table 6.2	J-V-L characteristics and device efficiency of devices E1-1 to E1-4.	115

# **Chapter 1.**

## **Introduction**

### **and Thesis Overview**

#### **1.1 Introduction**

Organic semiconductors have been utilized in many opto-electronic devices such as organic light emitting diodes (OLEDs), organic photovoltaics (or so called organic solar cells), organic field effect transistors, organic photodetectors and organic lasers. Among these known applications, OLEDs have gained a lot of attention as the next generation of display applications and solid-state lighting due to several advantages in physical and electronic features. OLEDs have a wide viewing angle of nearly 170°, wide color gamut and low power consumption. In contrast to conventional display applications such as liquid crystal displays, there is no need for OLEDs to have a backlight behind a screen because they are self-emissive, enabling thinner and lighter production. In 2015, LG Display showcased a 55-inch OLED panel that was 0.97 mm thick and 1.9 kg in weight, so it was possible to stick the TV panel to a wall with a magnetic mat as shown in Figure 1.1 (a). In addition, OLEDs offer high contrast because each pixel is completely switched on and off

without light leakage. OLEDs can be flexible and foldable when they are fabricated onto plastic substrates by solution processing techniques like spin coating, roll-to-roll and inkjet printings. As a light source, OLEDs are surface lights unlike light emitting diodes (LEDs) and fluorescent lamps so that they are more diffusive and can be configured on a large scale and in various shapes. OLED lighting is also energy efficient. To gain the upper hand, however, over conventional lighting in the marketplace, OLEDs must still come down in price.

These interesting aspects of OLEDs have motivated both academia and industry for the last few decades, bringing about the rapid development in OLED technologies. Consequently, OLED panels became the mainstream for various display applications in televisions, mobile displays and smart watches. Figure 1.1 shows various consumer products using OLEDs. The following sections will cover the history of OLEDs, and the objectives and outline of this thesis.



**Figure 1.1:** Various OLED applications available in the marketplace: (a) 55-inch OLED television, (b) screens for mobile phones and (c) smart watches (photo credit: LG Display, Samsung and Apple).

## 1.2 History of OLEDs

The first observation of electroluminescence (EL) by an organic single crystal, anthracene, was reported by Pope et al. in 1963 [1]. The operating voltage of the device was very high, over 400 V. The subsequent remarkable discovery in OLED technology was the double-layered OLED demonstrated by Tang and Van Slyke from Eastman Kodak in 1987 [2]. The reported OLED was composed of a hole transport material, diamine, and emitting and electron transport material, Tris-(8-hydroxyquinoline) aluminum ( $\text{Alq}_3$ ). This device structure with a heterojunction allowed effective carrier confinement for recombination. As a result, a high luminance over  $1000 \text{ cd/m}^2$  and  $\sim 1\%$  of external quantum efficiency (EQE) under 10 V at room temperature were achieved [2]. This revolutionary accomplishment has paved the way for a new chapter in OLED technology and led to various successive researches for OLEDs. Afterwards, the first polymer light-emitting diodes (PLEDs) with Poly(p-phenylene vinylene) (PPV) were introduced by Burroughs et al. of the University of Cambridge in 1990 [3]. Figure 1.2 displays the schematic diagrams of device structures of the first heterojunction OLED and PLED and molecular structures of the materials used for the devices.



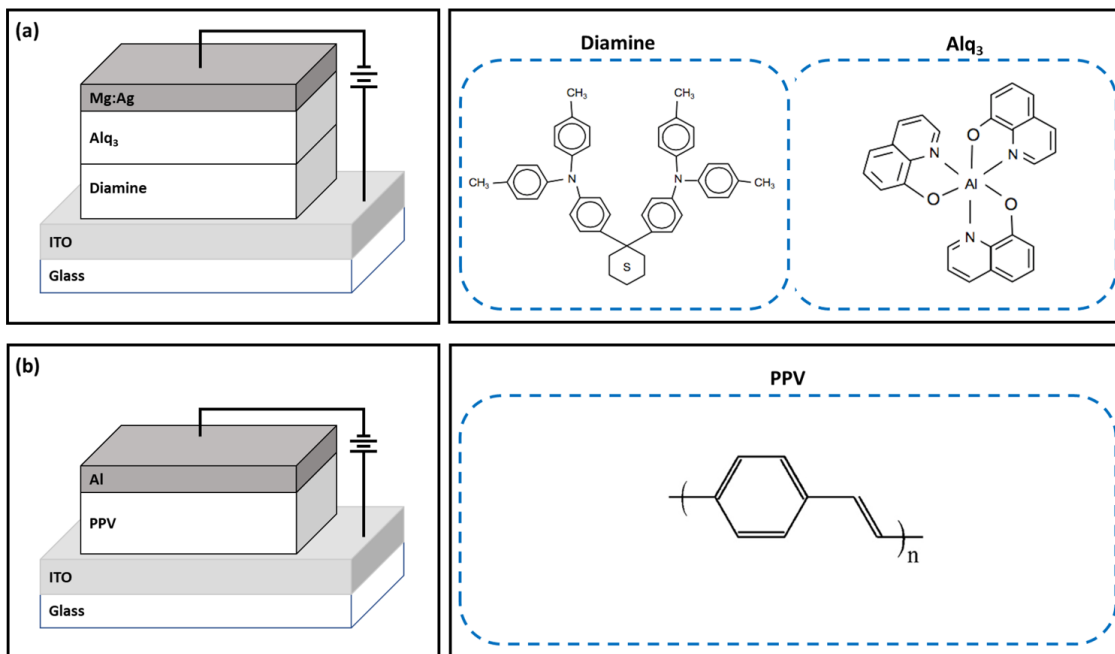


**Figure 1.2:** (a) Schematic diagram of the first double-layered OLED device structure and molecular structures of the organic materials used. The detailed structure of the device consists of indium tin oxide (ITO) (120 nm)/ Diamine (75 nm)/ Alq<sub>3</sub> (60 nm)/ Mg:Ag (100 nm). (b) Schematic diagram of the first PLED and the molecular structure of the conjugated polymer. The detailed device structure consists of ITO/ PPV (70 nm)/ Al.

Another noteworthy accomplishment in OLED technology was the introduction of phosphorescent materials by Forrest and Baldo in 1998 [4]. Most works at the early stage of OLED development focused on fluorescent emitting materials whose internal quantum efficiency (IQE) was limited to 25 % based on spin statistics. From this discovery the theoretical IQE reached up to nearly 100 % by harvesting triplet excitons. The insertion of heavy metal complexes such as Pt or Ir into molecules enables the mixing of singlet and triplet states via strong spin-orbit coupling, allowing intersystem crossing (ISC) to the triplet states, thereby enabling phosphorescent emission. Afterwards, state-of-the-art

thermally activated delayed fluorescence (TADF) was reported by Endo et al. in 2011 [5], which allowed OLED technology to go one more step further. This type of material has a near zero gap between the lowest singlet and triplet energy states; therefore, 100% of the theoretical IQE of fluorescence is achievable via reverse ISC (up-conversion) from the lowest triplet state to the lowest singlet state.

Based on the successive developments in materials the first commercial OLED was released by Pioneer Corporation in 1997. This product was a green emissive passive-matrix OLED for car audio systems. A decade later, Samsung Mobile Display firstly used the active-matrix OLED for mobile phones and the first commercial OLED lighting was introduced by Lumiotec in 2011. After the introduction of the first commercial OLED, various applications of OLEDs with many different sizes have been released and are easily found in our daily life.

### **1.3 Objectives and Outline of the Thesis**

Tremendous research and development in OLED technology have brought various applications into the marketplace in many different manners. Among the three primary colors, blue is an essential element for both full color display applications and solid-state lighting. The first multi-layered fluorescent blue OLED was reported by Adachi et al. in 1990 and its maximum luminance was  $700 \text{ cd/m}^2$  with a power efficiency of  $0.22 \text{ lm/W}$  at  $10 \text{ V}$  [6]. In 2001, Adachi's group demonstrated the first phosphorescent blue OLED with a maximum EQE of  $5.7 \%$  and power efficiency of  $6.3 \text{ lm/W}$  [7]. Research for blue OLEDs has been continuously going on; however, research progress and accomplishments

regarding blue emitting materials lag behind compared to other two primary colors, red and green. Among these three colors, blue emission has the shortest wavelength and highest photon energy. Considering that blue emitters need to have a wide energy bandgap, particularly in the case of blue phosphorescent emitters, it is difficult to engineer emitting materials to simultaneously satisfy requirements such as good stability and short exciton lifetime. Host and charge transport materials possessing a sufficiently large triplet energy are required to confine triplet excitons in blue phosphorescent emitters [8] and to prevent triplet exciton quenching [9]. Emitting regions consisting of a combination of fluorescent and phosphorescent emitters have been widely used for white OLEDs; however, for blue OLEDs, most of the research has been focused on fluorescent materials.

In this thesis, however, the emitting region for blue OLEDs is comprised of fluorescent and phosphorescent emitters in common. The introduced devices have different designs of emitting regions by controlling doping profiles and by switching combinations of emitting materials.

Based on the design concept of using both fluorescent and phosphorescent emitting materials for blue OLEDs, the objectives of this thesis are as follows:

- 1) Investigating how device performance changes when both types of emitters are adopted into the emitting region compared to purely fluorescent and/or phosphorescent blue OLEDs.
- 2) Understanding the origin and ratio of fluorescence and phosphorescence from blue OLEDs

- 3) Understanding the effects of different doping concentrations and different doping configurations on the electrical and optical properties of devices

The first chapter of this thesis is comprised of an introduction to organic semiconductors, the history of OLEDs, and the objectives of this thesis. The following chapter (Chapter 2) talks about fundamental principles of organic materials and OLED mechanisms, which are the foundation to a better understanding of OLEDs. Subsequently, photo-physics and electrical properties of OLEDs are explained. Chapter 3 presents the experimental details regarding device fabrication, including substrate preparation, material deposition and techniques for device characterization. Chapter 4 discusses the organic materials used for devices and the blue emitting materials' electrochemical properties, which are strongly related to device performance in terms of color. In the following chapter (Chapter 5), double emitting layered blue OLEDs with both fluorescent and phosphorescent emitting materials are proposed. The chapter is divided into two parts in accordance with different approaches to the spatial distribution in emitting materials, either uniformly or step-graded controlled. The first part of Chapter 5 covers the blue OLEDs' electrical and optical properties when varying the doping concentrations and switching the location of two emitting layers (EMLs). Afterwards, blue OLEDs with step-controlled doping profiles will be introduced. The phosphorescent doping concentration is step-controlled by 0, 4 and 8 % while the fluorescent one is fixed so that the effect of step-controlled doping profile can be explored. Chapter 6 describes electrical and optical properties of blue OLEDs with various combinations of triple EMLs. In addition, the origin

of blue emission will be investigated by resolving the EL spectra of the devices. The relation between the dependence of fluorescence and phosphorescence on EML configurations as well as the effect of an interlayer will be addressed. Finally, Chapter 7 covers the conclusion of the research work and suggestions for future research in blue OLEDs. The suggestions for future research provide some complementary experimental approaches, material optimization and a suggested path to adopting the presented research to white OLEDs with tunable color temperatures by controlling the voltage for the blue intensity.

#### **1.4 Contributions to Knowledge**

The research results in this thesis have been published in three peer-reviewed journal papers and two conference proceedings. Blue fluorescent OLEDs based on a host-dopant system have been reported in B. M. Lee et al., *Journal of Photonics for Energy*, 3(2013), 033598 and B. M. Lee et al., *Proceedings Volume 8412, Photonics North 2012*; 841221 (2012). The study showed the electrical and optical properties of blue fluorescent materials and how device performance changed when devices have different structures with single or double EMLs and a host-dopant system. Part of this work became a preliminary study of the main research work on blue OLEDs with fluorescent and phosphorescent emitters and is presented in Chapter 4 to explain the material properties of blue fluorescent emitters.

The dual-EML blue OLEDs with fluorescent and phosphorescent emitters were first published in B. M. Lee et al., *MRS Proceedings*, vol. 1567, pp. mrss13–1567-jj13–77

(2013). It mainly discussed the devices with various fluorescent doping concentrations to see what the impact of the fluorescent dopant is and how device characteristics change with different doping concentrations. The continuation of the work, which was published in B. M. Lee et al., *Journal of Luminescence*, 148 (2014) 72–78, provided expanded understanding of the dual-EML blue OLEDs by comparing different EML structures when the fluorescent and phosphorescent EMLs were switched. The journal publication of B. M. Lee et al., *Optical Materials*, 86 (2018) 498–504 gave a different approach to the dopant distribution in the dual-EML blue OLEDs and so this study explained the effect of step-controlled phosphorescent doping concentrations. Unlike the former research, another project focused on the triple-EML blue OLEDs and investigated the effect of different host material combinations, interlayers, and different EML thicknesses. This part of this project was published in B. M. Lee et al., *Science of Advanced Materials*, 8 (2016) 301-306.

#### 1.4.1 Peer reviewed Journal Papers

1. **B. M. Lee**, H. H. Yu, Y. H. Kim, N. H. Kim, J. A. Yoon, W.Y. Kim, P. Mascher, “*Highly efficient blue organic light-emitting diodes using dual emissive layers with host-dopant system*,” *Journal of Photonics for Energy*, 3(2013), 033598.  
[<https://doi.org/10.1117/1.JPE.3.033598>]
2. **B. M. Lee**, N. H. Kim, J. A. Yoon, S. E. Lee, Y. K. Kim, W.Y. Kim, P. Mascher, “*Luminescence Characteristics of Hybrid Dual Emitting Layers in Blue Organic Light-emitting Diodes by Controlling the Fluorescent Doping Concentration*,” *Journal of Luminescence*, 148 (2014) 72–78.

[<http://dx.doi.org/10.1016/j.jlumin.2013.11.065>]

3. **B. M. Lee**, S. I. Yoo, J. S. Kang, J. A. Yoon, W. Y. Kim, P. Mascher, “*Hybrid Blue Organic Light Emitting Diodes with Fluorescent and Phosphorescent Emitters along with an Interlayer*,” *Science of Advanced Materials*, 8 (2016) 301-306. [<https://doi.org/10.1166/sam.2016.2483>]
4. **B. M. Lee**, J. Kim, G. J. Yun, W. Y. Kim, P. Mascher, “*Study on hybrid blue organic light emitting diodes with step controlled doping profiles in phosphorescent emitting layer*,” *Optical Materials*, 86 (2018) 498–504. [<https://doi.org/10.1016/j.optmat.2018.09.039>]

#### **1.4.2 Conference Proceeding Papers**

1. **B. M. Lee**, H. H. Yu, Y. H. Kim, N. H. Kim, J. A. Yoon, P. Mascher, W.Y. Kim, “*Highly efficient blue organic light-emitting diodes using dual emissive layers with host-dopant system*,” *Proceedings Volume 8412, Photonics North 2012*; 841221 (2012). [<https://doi.org/10.1117/12.2001394>]
2. **B. M. Lee**, N. H. Kim, J. A. Yoon, W.Y. Kim, P. Mascher, “*Characterization of Hybrid Dual Emitting Layers in Blue Organic Light-Emitting Diodes by Controlling the Fluorescent Doping Concentration*,” *MRS Proceedings*, vol. 1567, pp. mrss13–1567-jj13–77 (2013). [<https://doi.org/10.1557/opl.2013.625>]

### **1.4.3 Conference Presentations**

1. Photonics North 2012, 2012, Montréal, Canada – Oral Presentation
2. Nano Ontario Conference 2012, 2012, Waterloo, Canada – Poster Presentation
3. MRS Spring Meeting & Exhibition, 2013, San Francisco, USA – Poster Presentation
4. Photonics North 2013, 2013, Ottawa, Canada – Oral Presentation
5. Nano Ontario Conference 2013, 2013, Kingston, Canada – Poster Presentation
6. Photonics North 2014, 2014, Montréal, Canada – Oral Presentation
7. Nano Ontario Conference 2014, 2014, Winsor, Canada – Poster Presentation
8. DVCE 2014: Display Valley Conference & Exhibition, 2014, Asan, Korea – Poster Presentation
9. The 17<sup>th</sup> Canadian Semiconductor Science and Technology Conference (CSSTC), 2015, Sherbrooke, Canada – Poster Presentation



# **Chapter 2.**

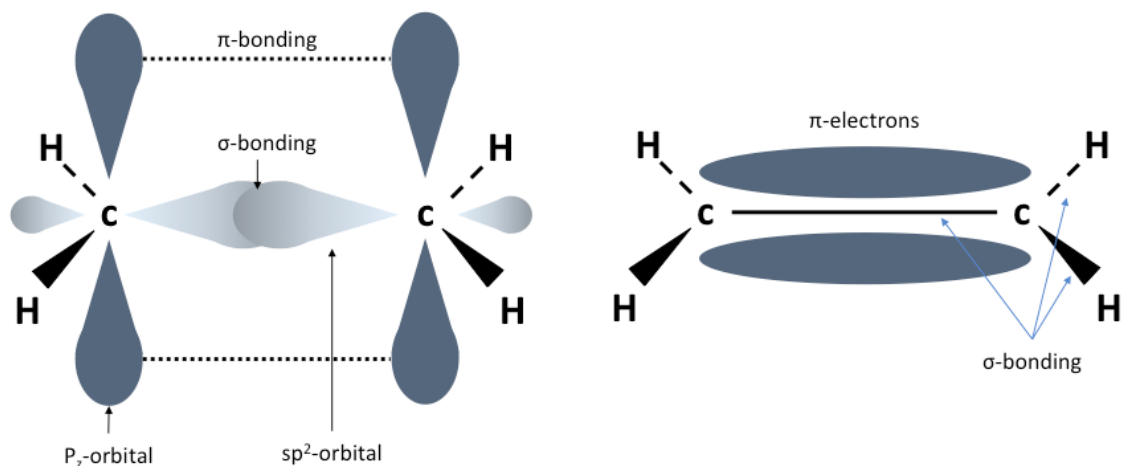
## **Fundamental Principles of Organic Light Emitting Diodes**

Organic materials show unique electronic properties, becoming a source of state-of-the-art electronic devices. For better understanding of OLEDs, this chapter focuses on the basic physical fundamentals of organic semiconductors. To be specific, section 2.1 gives an overview of the electronic properties of organic materials and then the operating mechanism of OLEDs will be discussed in section 2.2. Subsequent sections will discuss photophysical processes and the electrical properties of OLEDs.

## 2.1 Electronic Properties of Organic Materials

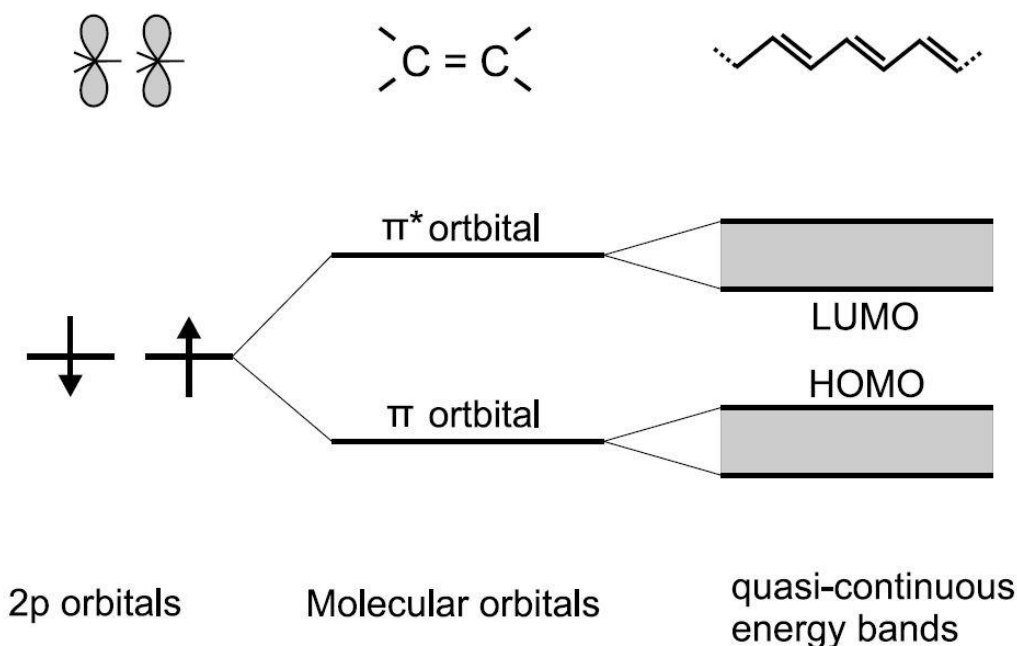
Organic semiconductors are made of carbon-based materials, so their characteristics are strongly affected by the material properties of carbon. The electronic configuration of a single carbon atom in the ground state is  $1s^2 2s^2 2p^2$ . When a carbon atom combines with another atom, hybrid orbitals are formed. Depending on how many atomic p-orbitals there are in each carbon atom contributing to hybridization, the possible cases are so-called  $sp$ ,  $sp^2$ , and  $sp^3$  hybridizations. In the case of  $sp^2$  hybridization, three  $sp^2$  hybrid orbitals are formed by the combination of the  $2s$  orbital and two of the three  $p$ -orbitals. These three  $sp^2$  hybrid orbitals form three  $\sigma$ -bonds, while the remaining  $p_z$ -orbitals which are orthogonal to the plane of the  $sp^2$  hybridization create a  $\pi$ -bond by overlapping each other. Delocalized electrons can move freely over the entire molecule via the  $\pi$ -orbital.

Figure 2.1 shows the configuration of  $sp^2$  hybridization in ethene ( $C_2H_4$ ).



**Figure 2.1:** Configurations of  $sp^2$  hybridization in ethene showing  $\sigma$  and  $\pi$  bonding between the two neighboring carbon atoms.

When two carbon atoms combine, the two p-orbitals form a new set of orbitals by splitting into  $\pi$ - (bonding) and  $\pi^*$ - (anti-bonding) orbitals. When the number of carbon atoms is increased for the formation of a molecule, more degenerations in the  $\pi$ - and  $\pi^*$ - orbitals are generated. If the number of atoms goes to infinity, energy bands are created as shown in Figure 2.2. The  $\pi$ -orbital corresponds to the highest occupied molecular orbital (HOMO) while the  $\pi^*$ -orbital is referred to as the lowest unoccupied molecular orbital (LUMO). These orbitals conceptually correspond to the valence and conduction bands in inorganic semiconductors, respectively. An energy difference between HOMO and LUMO is defined as the energy gap of the material and can be varied by the size of the molecule (delocalization). The gap decreases with the increase of the delocalization and spans the range of 1.5 – 4 eV for visible or near-UV emission.



**Figure 2.2:** Formation of bonding and anti-bonding molecular orbitals and energy bands (reprinted with permission from [10]).

## 2.2 Working Principles of OLEDs

An OLED is an electroluminescent device, meaning that luminescence is achieved by energy conversion from electrical to optical energy. It is made up of a stack of organic materials, with a thickness of a few hundred nanometers on average, between the anode and cathode. For light extraction either the anode or cathode should be transparent. The anode must have a high work function (such as ITO) while a low work function is required for the cathode (such as Al, Mg, Ca or Ag). When a voltage is applied, electrons and holes are injected from the cathode and anode, respectively. In this step, charge carriers need to overcome energy barriers between the electrodes and their neighbouring organic materials. Therefore, it is important to choose suitable materials to minimize the energy difference with the electrode. In OLEDs, a greater number of layers is used compared to inorganic LEDs owing to lower carrier mobilities and several orders of magnitude different mobilities between electrons and holes. So, in effect, electron/hole injection and transport layers are utilized to facilitate carrier flows. The injected electrons and holes migrate toward the opposite electrodes by hopping through neighbouring molecules and recombining with each other, creating excitons at an EML. The excitons relax to the ground state either radiatively or non-radiatively (by heat dissipation). EMLs can be designed based on the concept of a host-dopant system. The incorporation of dopant materials which are highly emissive in the visible spectral range into a host material can improve device efficiency. The color of emission in OLEDs is determined by the energy gaps of emitting materials where a recombination zone is generated. A depiction of the simplified structure of an

OLED and its operating process for emission are shown in Figure 2.3. The denoted numbers are the sequence of the operating processes in OLEDs.

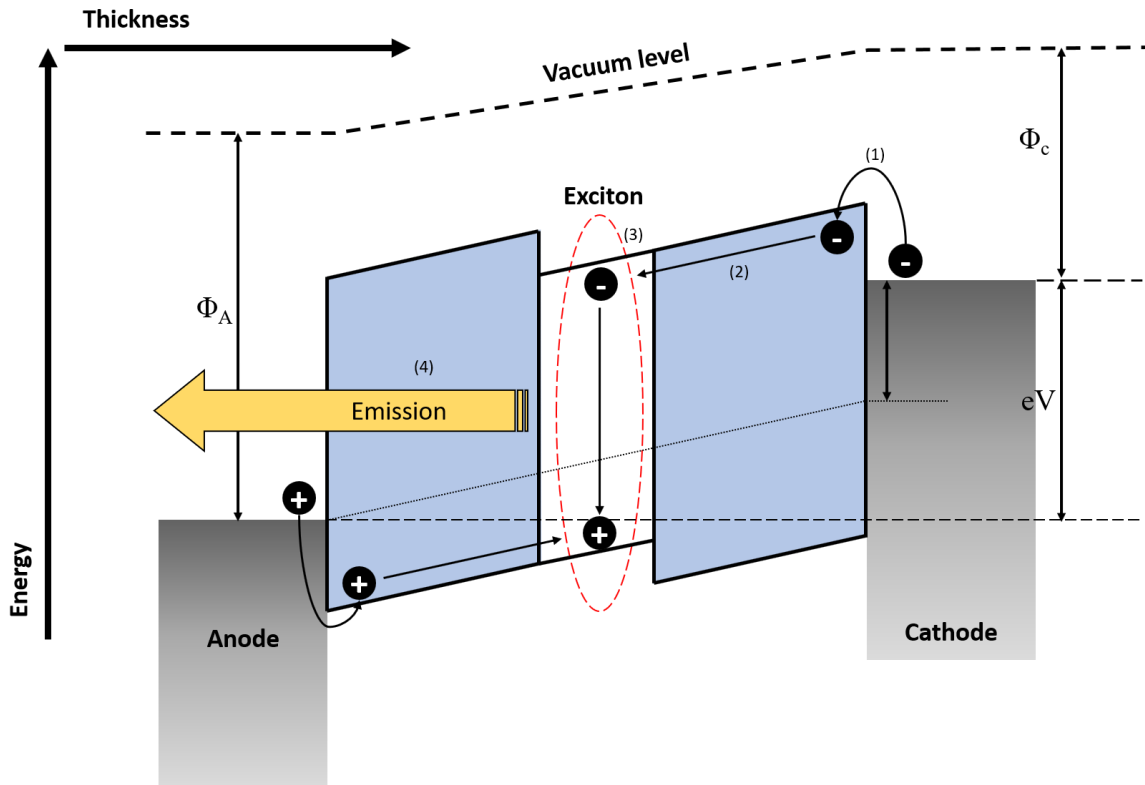


**Figure 2.3:** Schematic illustration of a three-layer bottom emitting OLED and its operating mechanism under a forward bias: (1) electrons and holes are injected from the cathode and anode, respectively. (2) Electrons and holes are transported toward the EML by hopping between molecules. (3) Electrons and holes recombine and create excitons at the EML and (4) excitons radiatively decay as photons which are extracted at the anode side.  $\Phi_C$  and  $\Phi_A$  are cathode and anode work functions, respectively.

## 2.3 Excitons

Excitons are electron and hole pairs bound by Coulomb forces and are electrically neutral. Excitons are classified in two different ways depending on spatial sizes and spin multiplicity. In the former case, excitons can be divided into three different types: Frenkel, Wannier-Mott and charge transfer excitons. The dielectric constant in organic materials is relatively low ( $\epsilon_r \sim 3$ ) compared to that of inorganic materials ( $\epsilon_r \sim 11-16$ ) so excitons in organic materials are highly localized with a large binding energy (0.1-1 eV) and small radius ( $< 5 \text{ \AA}$ ), which is called a Frenkel exciton. On the other hand, the excitons generally found in inorganic materials are called Wannier-Mott excitons. They have a large radius, usually larger than the lattice constant, due to a high dielectric constant. The electron-hole pairs are loosely bound with a small binding energy. Lastly, charge transfer excitons are found where electrons and holes are located nearby molecules or lattice sites with sufficiently strong coupling. The schematic illustrations of the three different types of excitons in spatial size are shown in Figure 2.4.

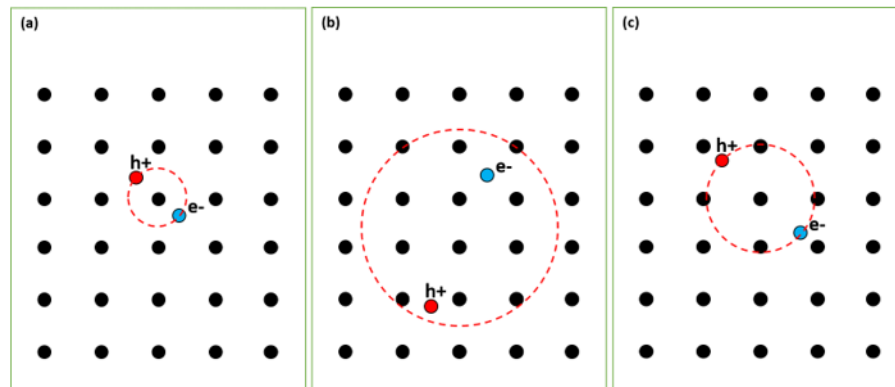


**Figure 2.4:** Schematic illustrations of three types of excitons from the spatial size viewpoint: (1) Frenkel exciton, (2) Wannier-Mott exciton and (3) intermediate charge-transfer exciton.

From the point of view of spin multiplicity ( $M = 2S + 1$ ), there are two types of excitons; singlet and triplet excitons. Electrons as fermions follow the Pauli exclusion principle, meaning that two electrons with opposite spins can occupy each orbital. The spin states of electrons are  $S = \pm \frac{1}{2}$  so that electron-hole pairs have four possible configurations. To be specific, when the spins of the electron-hole pair are anti-parallel, the total spin angular momentum is  $S = 0$  and is called a singlet exciton. On the other hand, if the total spin is  $S = 1$  with a set of parallel spins, the pair is called a triplet exciton. Under electrical excitation, the ratio of singlet to triplet excitons is 1:3 based on the spin statistics. Figure 2.5 shows the four different possible quantum states, creating singlet and triplet excitons.

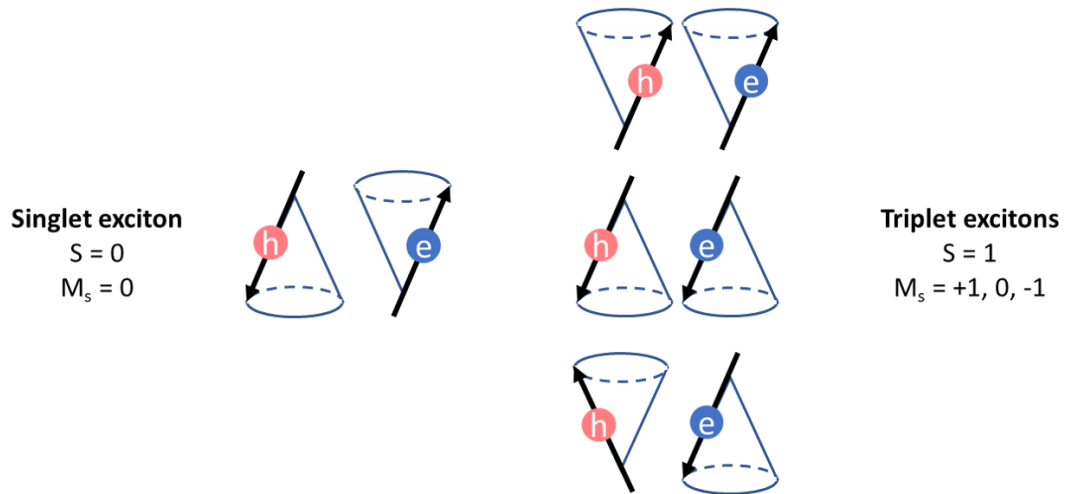


**Figure 2.5:** Spin states for singlet and triplet excitons with total spin quantum numbers ( $S$ ) and magnetic quantum numbers ( $M_s$ ).

## 2.4 Photophysical Processes in OLEDs

### 2.4.1 Jablonski Diagram

Excited electrons go through several transition paths. The Jablonski diagram is an illustration to explain various possible transitions for light emission and quenching in molecular compounds and the diagram is introduced in Figure 2.6. There exist several energy states such as electronic, vibrational, rotational and translational states. The thick solid lines are electronic energy states and the thin ones are vibrational states. The capital letters imply a spin multiplicity: S for singlet and T for triplet states. The subscript numbers represent the level of electronic energy states; therefore,  $S_0$  denotes the ground state and larger numbers mean higher states.

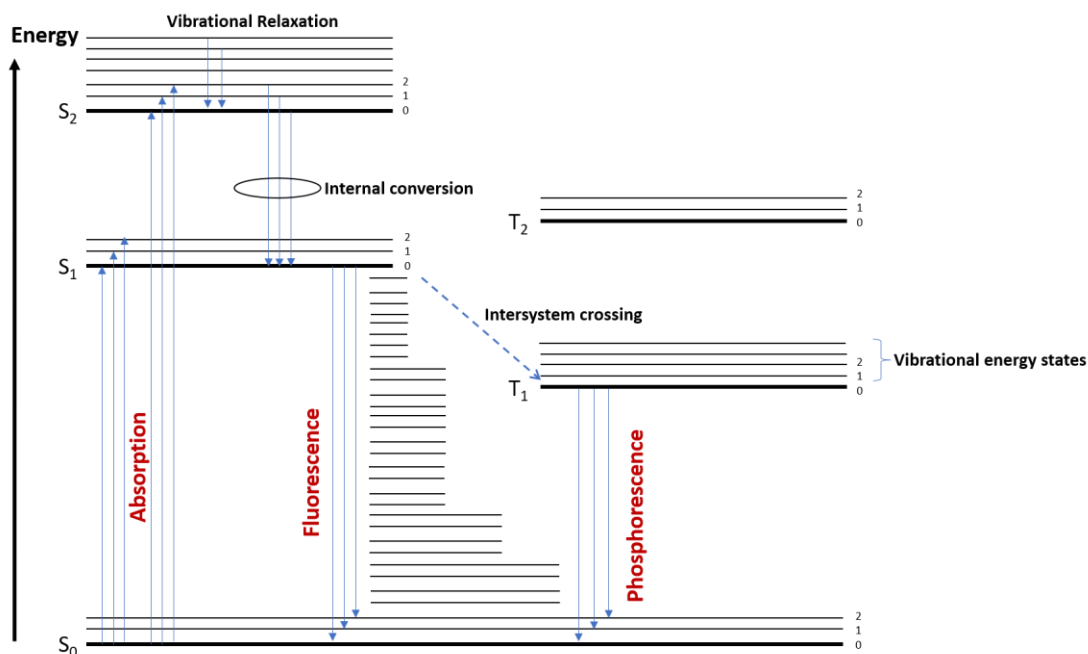


**Figure 2.6:** Jablonski diagram showing vibrational and electronic energy states and possible transitions in an organic molecule. Each sublevel of vibrational states corresponds to a manifold of rotational and translational levels with  $\sim 0.01$  eV spacing.



### 2.4.2 Non-radiative Transitions

After an electron in the ground state is either optically or electrically excited, it undergoes radiative or non-radiative processes until relaxing back to the ground state. Relaxation between vibrational states, to the corresponding lowest vibrational state, is called vibrational relaxation. Internal conversion (IC) is another non-radiative transition from a higher to a lower electronic state within the same multiplicity. During the radiationless transition, heat may be dissipated, equivalent to the magnitude of the relaxation. ISC is also a non-radiative transition but it happens between the different multiplicities from singlet to triplet energy states. Although this is a forbidden transition, the transition can be allowed due to spin-orbit coupling, for example by heavy metal atoms.

### 2.4.3 Radiative Transitions

There exist two different luminescence processes: fluorescence and phosphorescence, which are differentiated by transition time and multiplicity of the initial state in the case of luminescence. Singlet excited states can go through either radiative relaxation to the ground state or move to the triplet excited state via ISC. The radiative relaxation directly from the lowest singlet excited state ( $S_1$ ) to the ground state ( $S_0$ ) is called fluorescence. In this process, the spin multiplicities of the initial and final states are the same and the relaxation is very fast within  $10^{-9}\sim 10^{-8}$  s. In fluorescent OLEDs, only singlet excitons can be involved for luminescence, so the internal quantum yield is limited to 25 %. Emission by triplet excitons is forbidden, hence triplet excitons are “wasted” in fluorescent OLEDs.

For phosphorescence, on the other hand, after ISC, electrons radiatively decay from the lowest triplet excited state ( $T_1$ ) to the ground state ( $S_0$ ), meaning that there is a change in spin multiplicity. The transition time for the phosphorescence process is much longer ( $10^{-6}\sim 10^2$  s) than for fluorescence. In phosphorescent OLEDs, triplet excitons can be harvested by spin-orbit coupling due to the existence of heavy metal complexes such as Pt or Ir. The strength of spin orbit coupling is proportional to the forth power of the atomic number of the metal, so stronger spin orbit coupling can be achieved by the use of heavier metals, leading to improved emission efficiency [11]. The theoretical IQE of nearly 100 % is attributed to the utilization of both singlet and triplet excitons for luminescence.

As depicted in Figure 2.6, the singlet excited states ( $S_n$ ) are higher in energy than the triplet excited states ( $T_n$ ). This can be explained by the Pauli exclusion principle. In singlet excitons, electrons with an antiparallel spin pair are in proximity to each other so a strong overlap in wave functions is permitted, leading to a larger Coulombic repulsive energy. That is why the energy of singlet states is larger than that of triplet ones.

#### **2.4.4 Energy Transfer**

The host-dopant system has been widely utilized to enhance device efficiency through an effective energy transfer between the host (donor) and dopant (acceptor) molecules. The two main non-radiative exciton energy transfers mechanisms are called Förster [12] and Dexter energy transfers [13].

### 2.4.4.1 Förster Energy Transfer

Förster energy transfer is a non-radiative transfer process via a long-range dipole-dipole coupling interaction between two molecules and occurs when the intermolecular distance is typically less than 100 Å. The process is represented in Figure 2.7 and allowed energy transfer reactions of Förster and Dexter energy transfer are shown in Table 2.1. At the initial stage, the host molecule is excited while the dopant molecule stays in the ground state. The host molecule relaxes to the ground state and the electron in the dopant molecule is excited by the energy transfer. The rate constant of Förster energy transfer ( $k_{FET}$ ) [12] is given by:

$$k_{FET} = \frac{1}{\tau_H} \left( \frac{R_0}{R_{HD}} \right)^6 \quad \text{Eq. 2.1}$$

where  $\tau_H$  is the fluorescence lifetime of the host in the absence of the dopant,  $R_{HD}$  is the intermolecular distance between the host and dopant molecules and  $R_0$  is the Förster radius.

$R_0$  can be calculated by the following equation:

$$R_0 = \left( \frac{9000\kappa^2 \ln 10 \phi_{PL}}{128 \pi^5 n^4 N_A} \int f_H(\nu) \varepsilon_D(\lambda) d\lambda \right)^{\frac{1}{6}} \quad \text{Eq. 2.2}$$

where  $f_H(\nu)$  is the normalized PL spectrum of the host material,  $\varepsilon_D(\nu)$  is the absorption spectrum of the dopant material (the molar absorption coefficient of the dopant),  $\lambda$  is wavelength,  $\kappa$  is an orientation factor,  $\phi_{PL}$  is the absolute fluorescence quantum yield of the host material,  $n$  is the refractive index of the material, and  $N_A$  is Avogadro's number.

When combining Eq. 2.1 and Eq. 2.2, the rate constant of Förster energy transfer ( $k_{FET}$ ) can be expressed as:

$$k_{FET} = \frac{9000\kappa^2 \ln 10 \phi_{PL}}{128 \pi^5 n^4 N_A \tau_H R_{HD}^6} \int \lambda^4 f_H(\nu) \varepsilon_D(\lambda) d\lambda \quad \text{Eq. 2.3}$$

From Eq. 2.3 one can identify several important contributors to an efficient Förster energy transfer. Firstly, the degree of a spectral overlap between the absorption of the dopant and the PL of the host determines the transfer rate constant. Larger overlap means more efficient energy transfer between molecules. The energy transfer rate also is dependent on the intermolecular distance between host and dopant molecules ( $\sim(R_{HD})^{-6}$ ) but it should be less than 100 Å. A large absorption coefficient of the dopant material is beneficial to having efficient energy transfer.

The energy transfer efficiency ( $E_{ET}$ ) [12] is defined as:

$$E_{ET} = \frac{R_0^6}{R_0^6 + (R_{HD})^6} \quad \text{Eq. 2.4}$$

When the Förster radius ( $R_0$ ) is equal to the distance between host and dopant molecules ( $R_{HD}$ ), the energy transfer efficiency is 50 % and the rate constant of the energy transfer ( $k_{FET}$ ) is  $1/\tau_H$  which is equivalent to the emission rate of the host molecule [10].

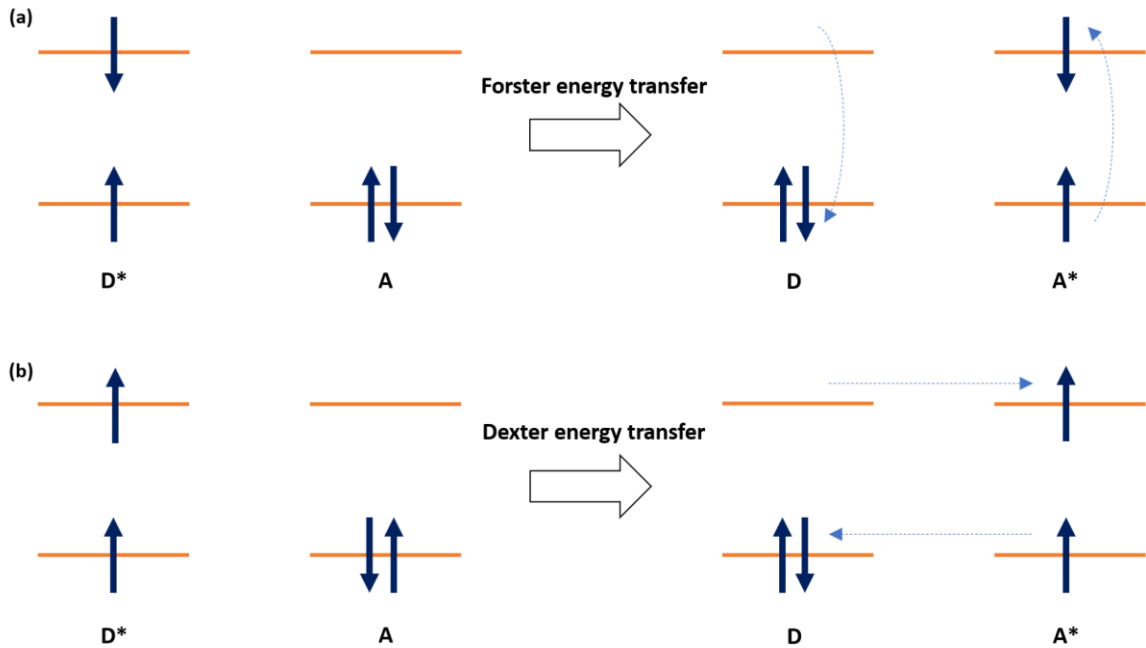


**Figure 2.7:** Schematic representations of (a) Förster and (b) Dexter energy transfer.

**Table 2.1:** Available energy transfer processes between the host and dopant molecules. The excited state is denoted with an asterisk (\*) and the number represents spin multiplicities.

Förster Energy Transfer	Dexter Energy Transfer
${}^1H^* + {}^1D \rightarrow {}^1H + {}^1D^*$ Singlet $\rightarrow$ Singlet	${}^1H^* + {}^1D \rightarrow {}^1H + {}^1D^*$ Singlet $\rightarrow$ Singlet
${}^3H^* + {}^3D \rightarrow {}^3H + {}^3D^*$ Triplet $\rightarrow$ Triplet	${}^3H^* + {}^1D \rightarrow {}^3H + {}^3D^*$ Triplet $\rightarrow$ Triplet

#### 2.4.4.2 Dexter Energy Transfer

Dexter energy transfer is a short-range interaction by exchanging electrons from host to dopant molecules. Figure 2.7 (b) shows the process of Dexter energy transfer and possible Dexter energy transfer processes are shown in Table 2.1. The electron in the excited state in the donor molecule transfers to the donor excited state. Simultaneously, the electron in the ground state in the dopant molecule moves to the host molecule. This energy transfer can be achieved when the host and dopant molecules are in close proximity, typically up to  $\sim 10 \text{ \AA}$ , because this process requires the overlap of the wave functions between host and dopant molecules. The transfer rate constant of the Dexter energy transfer ( $k_{DEX}$ ) [13] is obtained by

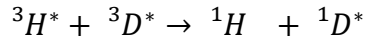
$$k_{DEX} = \left(\frac{2\pi}{h}\right) K \exp\left(-\frac{2R}{L}\right) \int \lambda^4 f_H(\nu) \varepsilon_D(\lambda) d\lambda \quad \text{Eq. 2.5}$$

where  $h$  is Planck's constant,  $K$  is a constant proportional to the orbital overlap between two molecules,  $R$  is a distance between host and dopant molecules, and  $L$  is the sum of the Van der Waals radii of the two molecules. Like Förster energy transfer, the rate constant is strongly related to the overlap of host PL and dopant absorption spectra and the distance between the host and dopant molecules.

### 2.5 Exciton Quenching Mechanism

The annihilation of an exciton with another exciton or polaron is called quenching. The quenching process is typically found at a high current density and is dominated by either Förster or Dexter energy transfer.

When two triplet excitons interact, one of them is promoted to the singlet excited state ( $S_n$ ) and the other one relaxes to the ground state ( $S_0$ ). This process is called triplet-triplet annihilation (TTA).



Considering that the TTA happens in a fluorescent-based device, the singlet exciton can be radiatively relaxed, resulting in delayed fluorescence. However, in a phosphorescent-based device, the singlet exciton created by the TTA can move back to the triplet excited state via ISC, which implies the loss of one exciton and lowers device efficiency. This is a main cause of efficiency roll-off under the high population of triplet excitons in phosphorescent OLEDs because of the long lifetime of triplet excitons, on the order of microseconds to milliseconds. Triplet excitons can also interact with polarons, called Triplet-polaron annihilation. This annihilation occurs under a high current density and gives rise to efficiency roll-off, similar to TTA.

## 2.6. Electrical Properties of OLEDs

Unlike crystalline inorganic materials with periodic lattice structures, organic materials are amorphous and have disordered energy states. Due to the different material properties, in organic semiconductors, charge carriers are transported via “hopping” between distinct localized states. In OLEDs, carrier flows including injection and transport is affected by the electrode/organic and organic/organic (bulk) interfaces.

### 2.6.1 Charge Carrier Injection

The operation of OLEDs begins with charge carrier injection under applied forward bias. Electrons are injected from the cathode to the adjacent organic layer, either an electron injection layer (EIL) or an electron transport layer (ETL). Similarly, hole injection occurs from the anode to the neighboring layer, either a hole injection layer (HIL) or a hole transport layer (HTL), depending on device structures.

There are two models to describe carrier injection: The Fowler-Nordheim model [14] involving tunneling and the Richardson-Schottky model involving thermionic emission. Although these two models were designed for inorganic semiconductors without the consideration of energetic disordered structures in organic materials, they are still useful to conceptually understand the injection process at the metal-organic interface in organic devices.

The Richardson-Schottky model [15], [16] explains charge carrier injection by thermionic emission, electrons need to carry sufficient thermal energy to overcome the potential barrier. The injection characteristic of the Richardson-Schottky model are given as:

$$J_{RS} = \frac{4\pi q m^* k^2}{h^3} T^2 \exp\left(-\frac{E_b}{k_B T}\right) \quad \text{Eq. 2.6}$$

where  $q$  is the electric charge,  $m^*$  is the effective mass of either electron or hole,  $k_B$  is the Boltzmann constant,  $h$  is Planck's constant,  $T$  is temperature,  $E_b$  is the interfacial energy barrier and  $V$  is an applied voltage. The first term of the equation is the Richardson constant. The interfacial energy barrier ( $E_b$ ) varies under the electric field at the interface:



$$E_b = \phi_B - \sqrt{\frac{q^3 |F(0)|}{4\pi\epsilon}} \quad \text{Eq. 2.7}$$

Where  $\phi_B$  is the Schottky energy barrier at zero field and  $|F(0)|$  is the electric field at the interface. This phenomenon showing the reduction of the Schottky barrier height is called image force lowering as shown in Figure 2.8 (b).

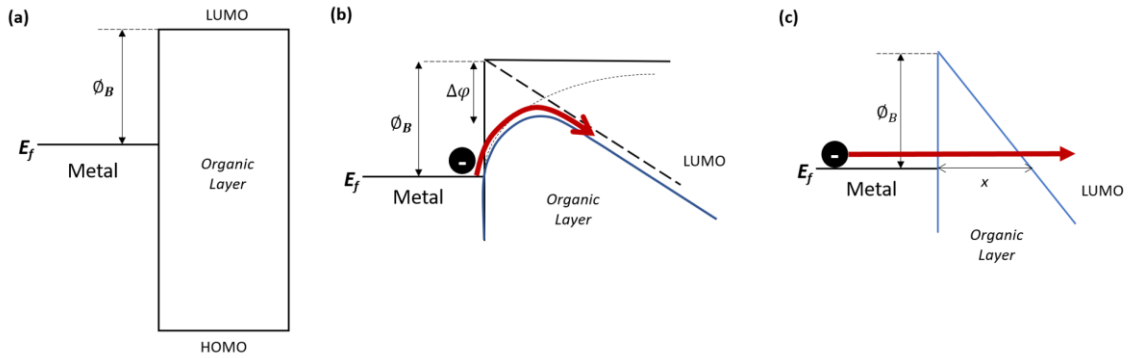


**Figure 2.8:** Schematic illustrations of (a) the energy barrier height ( $\phi_B = E_{\text{LUMO}} - E_f$ ) without any effects at the interface (b) Richardson-Schottky model with image force lowering ( $E_b = \phi_b - \Delta\phi$ ) and (c) Fowler-Nordheim model.  $E_f$  is the Fermi-level of the metal,  $\Delta\phi = \sqrt{q^3 |F(0)| / 4\pi\epsilon}$  and  $x$  is the tunneling distance.

Another way to explain charge injection from the metal is by the Fowler-Nordheim model through a tunneling process by the electric field as displayed in Figure 2.8 (c). The electrons are injected from the contact via a triangular potential barrier. The temperature independent Fowler-Nordheim model yields an injection current  $J_{FN}$ :

$$J_{FN} = \left( \frac{q^3 V^2 m_0}{8\pi h \phi_B m^*} \right) \exp \left( - \frac{4(2m^*)^{0.5} \phi_B^{1.5}}{3hqV} \right) \quad \text{Eq. 2.8}$$

where  $m_0$  is the mass of a free electron.

## 2.6.2 Charge Carrier Transport

Crystalline inorganic semiconductor materials show highly ordered structures, which causes delocalization of carriers moving through the energy band limited only by the scattering through lattice vibrations [10], called the band transport model. On the other hand, organic materials have weak electronic coupling between molecules via Van der Waals interactions. Because of this unique property carriers tend to move molecule-to-molecule by hopping rather than by band transport. Figure 2.9 depicts band transport in crystalline inorganic materials and hopping transport in disordered organic materials.

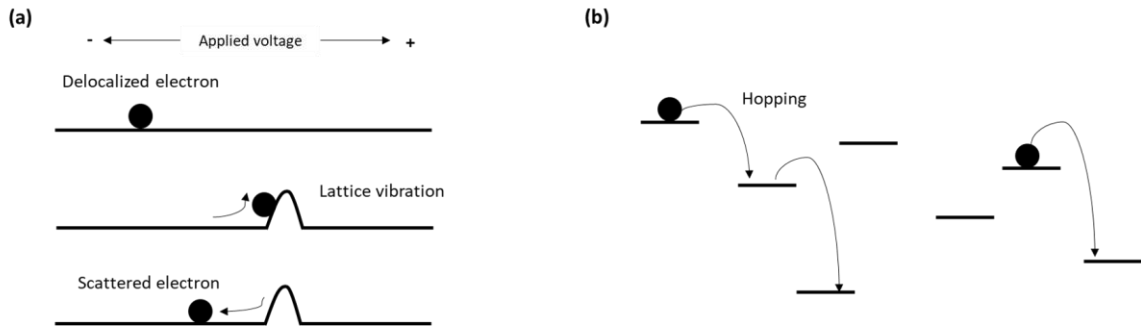


**Figure 2.9:** Schematic illustrations for charge transport models: (a) band transport model for highly ordered inorganic materials, and (b) hopping model for highly disordered organic materials.

After carrier injection into the organic layers, carriers are transported toward the opposite electrodes. In a very low electric field regime, the current is linearly proportional to voltage and is given by:

$$J_{ohmic} = en_0\mu \frac{V}{d} \quad \text{Eq. 2.9}$$

Where  $e$  is the electric charge,  $n_0$  is the electron density,  $\mu$  is the carrier mobility,  $V$  is the applied voltage, and  $d$  is the organic layer thickness. When the applied voltage further

increases, the number of injected carriers increases more and more and then at some point, it is possible for devices to have a higher density of injected carriers than that of thermally activated ones. In this case, the current is limited by space charges. The space charge-limited current (SCLC) can be described by the Mott-Gurney law:

$$J_{SCLC} = \frac{9}{8} \varepsilon \varepsilon_0 \mu \left( \frac{V^2}{d^3} \right) \quad \text{Eq. 2.10}$$

Where  $\varepsilon$  is the relative dielectric constant,  $\varepsilon_0$  is the permittivity of free space and  $\mu$  is the electric field-independent mobility. The Mott-Gurney law is applied for a unipolar trap-free device with an Ohmic contact.

It has been well known, however, that most organic semiconductors have a field-dependent mobility. If an electric field is applied, the external potential is superimposed on the Coulomb potential of the hopping sites, so the carrier mobility is modified by the applied electric field. When the field-dependent mobility given by the Poole-Frenkel effect is applied to the SCLC, an approximation of the SCLC for a field-dependent mobility is given by [17]:

$$J_{SCLC} = \frac{9}{8} \varepsilon \varepsilon_0 \mu(F) \exp\left(0.89\beta \sqrt{\frac{V}{d}}\right) \left(\frac{V^2}{d^3}\right) \quad \text{Eq. 2.11}$$

where  $\mu(F) = \mu_0 \exp(\beta\sqrt{F})$ ,  $\mu_0$  is the zero-field mobility,  $\beta$  is the field activation factor, which is temperature dependent, and  $F$  is the electric field. In all organic semiconductors, structural defects (traps) impact the charge carrier transport. The trap charge-limited current (TCLC) is limited by filling traps with carriers and is expressed by [18]:

$$J_{TCLC} = N_{eff} q \mu \left( \frac{\epsilon_r \epsilon_0}{q n_t(E_t)} \right)^l \left( \frac{2l+1}{l+1} \right)^{l+1} \left( \frac{l}{l+1} \right)^l \left( \frac{V^{l+1}}{d^{2l+1}} \right) \quad \text{Eq. 2.12}$$

Where  $N_{eff}$  is the effective density of states in the band,  $n_t(E_t)$  is an exponential distribution of the density of traps, and  $l$  is the trap distribution parameter ( $l = T_c/T$ ) and is greater than 1.  $T_c$  is the characteristic temperature of the trap distribution ( $T_c = E_t/k_B$ ).

The density of traps in the exponential distribution  $n_t(E_t)$  is

$$n_t(E_t) = \frac{N_t}{k_B T_c} \exp\left(-\frac{E_t}{k_B T_c}\right) \quad \text{Eq. 2.13}$$

where  $N_t$  is the total density of the traps, and  $E_t$  is the trap energy with respect to the LUMO/ HOMO energy levels. The TCLC shows a power-law dependence and turns to the SCLC if all the traps are filled. Figure 2.10 shows Ohmic, SCL and TCL current characteristics.

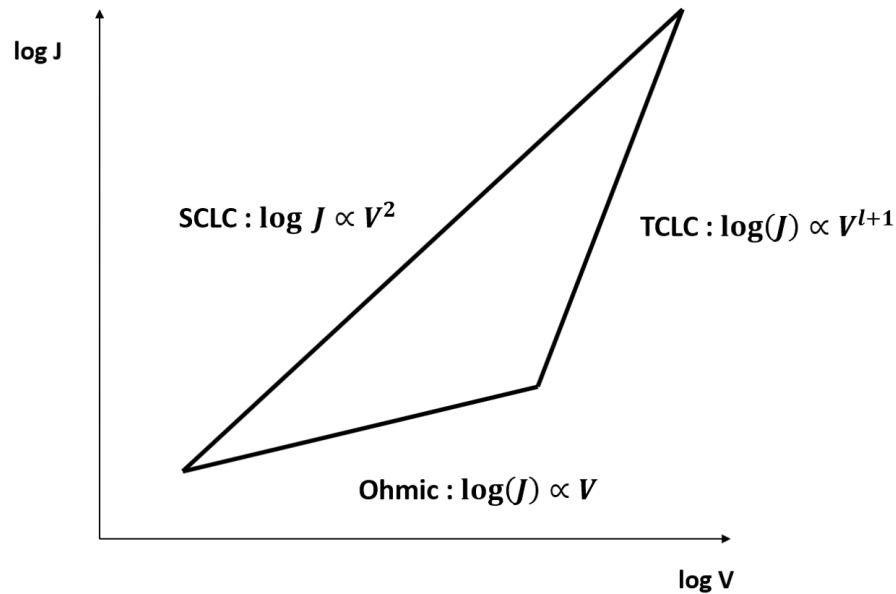


**Figure 2.10:** Log J-log V characteristics in three different regimes dependent on the applied voltage.

### 2.6.3 Charge Trapping

When dopant materials are introduced into a host material, the dopant molecules can be trap sites which have an influence on carrier transport as well as play a role as direct recombination sites. Since the injected carriers tend to fill the trap sites, the presence of traps may result in higher threshold and operating voltages and drastic increases in current density. Trap types are determined by the alignment of the HOMO and LUMO energy levels of the dopant materials with respect to those of a host material. Three main cases of carrier trapping are found in the host-dopant systems such as electron trapping, hole trapping, and both electron and hole trappings.

### 2.6.4 Recombination of Excitons

When electrons and holes move toward opposite sides after injection, they can recombine and create excitons. Based on the Langevin theory, excitons are generated when electrons and holes are placed within the Coulomb capture radius. The Langevin recombination rate ( $R$ ) is given by:

$$R = \frac{q(\mu_e + \mu_h)}{\varepsilon \varepsilon_0} np \quad \text{Eq. 2.14}$$

$$= \gamma n p \quad \text{Eq. 2.15}$$

Where  $\mu_e$  and  $\mu_h$  are the electron and hole mobilities, respectively,  $n$  and  $p$  are the electron and hole densities, respectively, and  $\gamma$  is the Langevin recombination coefficient.

Electron and hole recombination can take place at trap sites.

# **Chapter 3.**

## **Experimental Methods and Performance Metrics**

This chapter describes and discusses the experimental details for OLED fabrication, organized into three parts: sample preparation, sample fabrication, and characterization techniques. Firstly, the sample preparation and organic material depositions by means of thermal evaporation are covered. The subsequent sections describe measurement techniques and metrics used to characterize the fabricated OLED devices.

### **3.1 Sample Preparation**

#### **3.1.1 Cleaning ITO glasses**

For bottom emitting OLEDs, ITO is widely utilized for the anode because of its high conductivity and transparency. The dimensions of the substrates were  $25 \times 25 \text{ mm}^2$  and 0.7 mm thick. The ITO film thickness was 1800 Å and its sheet resistance was  $20 \Omega/\square$ . The pre-coated ITO glasses were patterned by photolithography. Each substrate has 4 emissive

pixels and its active area is  $3 \times 3 \text{ mm}^2$ . Figure 3.1 is the top view layout of fabricated devices in the sequence of fabrication.

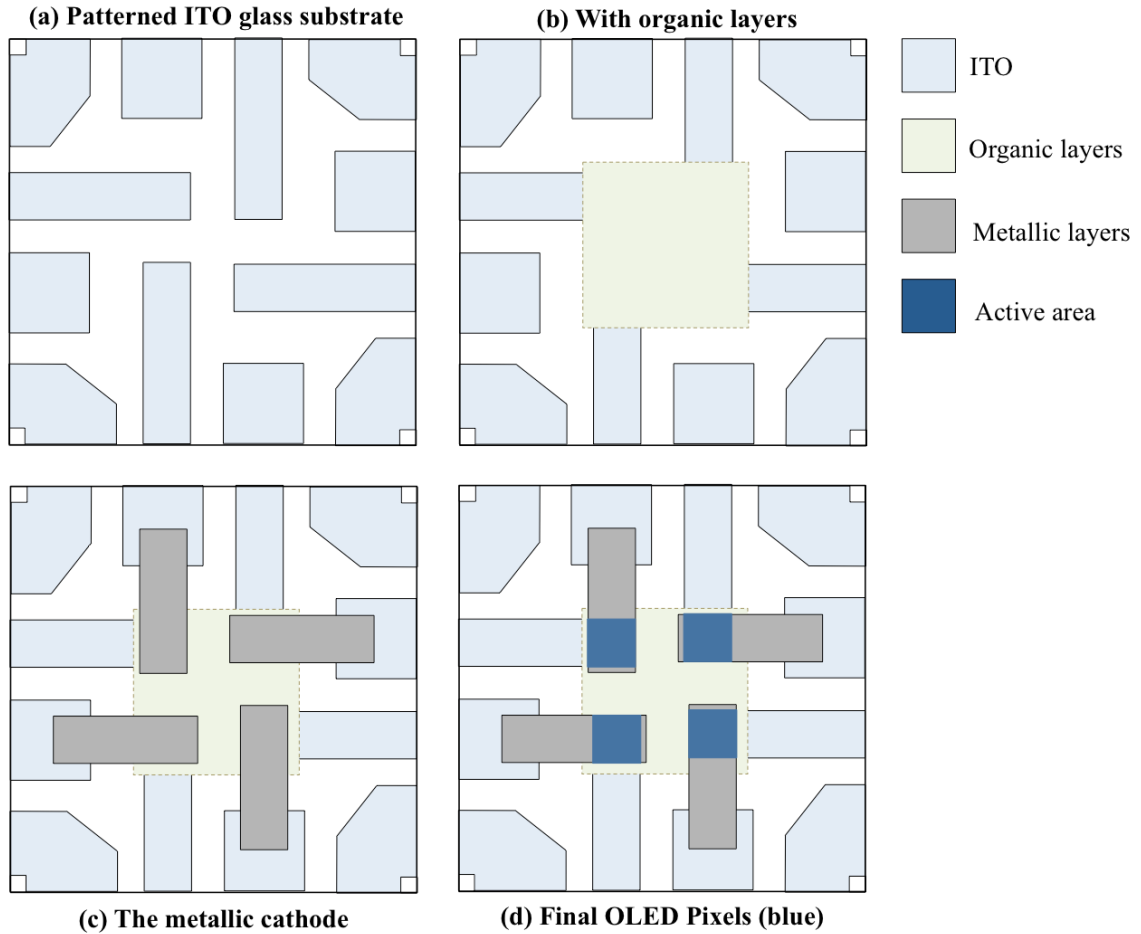


**Figure 3.1:** Schematic diagrams of the top view of the device in order of fabrication: (a) pre-coated ITO glass, (b) after organic material deposition on the ITO, (c) the metallic cathode layer deposition and (d) fabricated device with 4 emissive pixels.

It is known that the surface characteristics of ITO substrates impact device performance because any contaminants on the substrates may cause defects. So, substrate cleaning is a vital step to enhance device performance. The ITO substrates were chemically cleaned with acetone and isopropanol in an ultrasonic bath for 15 min each and then rinsed with

deionized water. This cleaning step is to remove organic contaminants on ITO substrates. Any particles or contaminants on the ITO surface may cause poor device performance such as electrical shorts or defects. After drying with nitrogen ( $N_2$ ) gas, the clean substrates were placed into a load-lock chamber for oxygen plasma treatment and organic material deposition.

### **3.1.2 Plasma Treatment for ITO Glass Substrates**

The typical work function of ITO is in the range of 4.5-4.8 eV [19] and the HOMO energy level of a common HTL material, NPB, is - 5.4 eV so injected holes encounter a large energy barrier which hinders carrier flows toward the adjacent layer. Pretreatment of ITO is one of the ways to resolve the problem by enhancing its work function. The widely used pretreatment methods are UV-ozone and oxygen plasma treatment. The adsorption or desorption of oxygen on the ITO surface greatly influences the work function of ITO. To be specific, increasing the oxygen content of the ITO surface results in an increase in the work function. Some reports showed that the work function increased by about 0.3 eV from untreated ITO with 4.5 eV work function [20]–[24]. In this work, oxygen plasma treatment was carried out. Oxygen gas is injected at 3 SCCM (standard cubic centimeters per minute) until the chamber pressure reaches  $5.0 \times 10^{-2}$  Torr and then 200 W of RF power is applied for 2 min for the  $O_2$  plasma treatment. In addition, the oxygen plasma treatment makes the surface smoother. The pretreated ITO substrates were transported to the deposition chamber without exposure to the air.



## 3.2 Thermal Evaporation of Organic Layers

### 3.2.1 Organic Material Deposition

There are two techniques for OLED fabrication according to the types of organic materials used: (1) wet coating (spin coating) for polymers, and (2) thermal evaporation for small molecular materials. In this thesis, only thermal evaporation will be covered because all devices were fabricated with small molecular materials. Thermal evaporation is one of the physical vapor deposition methods. Organic materials in crucibles are evaporated by resistive heat. To prevent the exposure of organic materials to water and oxygen, the deposition process should take place in an ultra-high vacuum ( $\sim 8.0 \times 10^{-7}$  Torr) environment. The deposition rate and film thickness of organic materials were monitored by quartz crystal microbalances. This allows devices to have multiple layers of accurately controlled thickness. The deposition rates of host and dopant materials were monitored separately so that doping concentrations can be controlled by varying the relative deposition rates between host and dopant materials. The typical deposition rate for organic materials was  $1 \text{ \AA/s}$ . The substrates were situated on a rotating stage at the top of the vacuum chamber, which enables the formation of a uniformly thick films. The deposition system and the internal part of the organic deposition chamber are shown in Figure 3.2. The thermal evaporation system used to fabricate all devices for the present studies is located at Hoseo University in Asan, Korea.

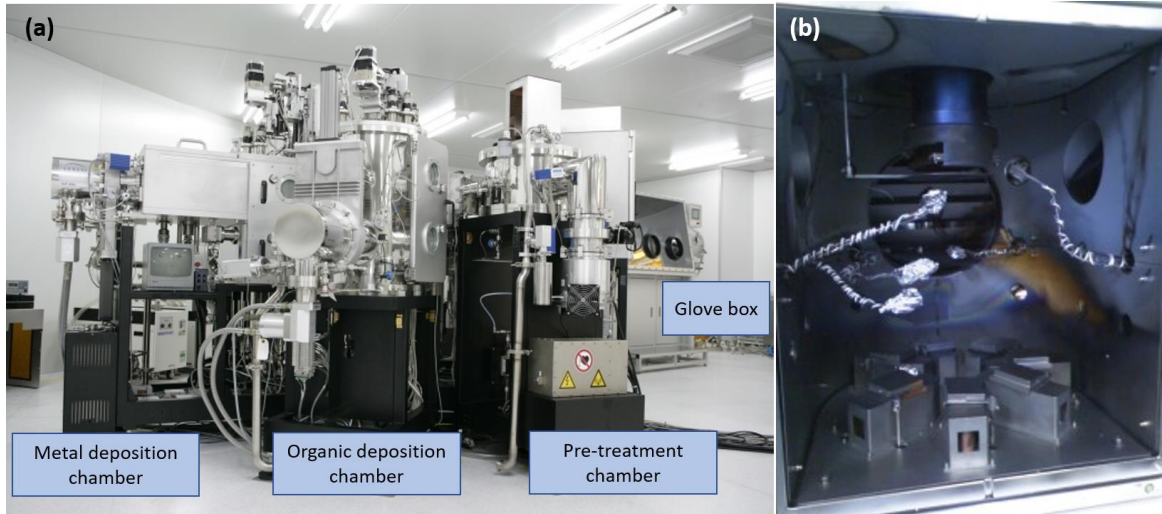


**Figure 3.2:** (a) OLED fabrication system and (b) the internal feature of the organic deposition chamber.

### 3.2.2 Metal Deposition

Metal deposition took place in a separate chamber to prevent additional contaminations by residual organic materials when the deposition occurred in the same chamber. The deposition rate for the cathode was  $\sim 10 \text{ \AA/s}$ . After the metal deposition process, devices cooled down to room temperature and then were transferred to the glove box for encapsulation. The cathode is strongly reactive in the presence of oxygen and/or water. The reaction results in the formation of insulating metal oxides as dark spots that degrades luminescence. That is why encapsulation is important to protect devices from permeating water and oxygen.

### 3.2.3 Encapsulation

The typical method for encapsulation is sealing the edge of devices with a cover glass and UV-cured epoxy resin. However, in this work 3M double-sided tapes were used. For this process, a desiccant powder of Barium Oxide (BaO) was applied on the substrate and then covered with the cover glass. This process took place in a glove box filled with nitrogen and the fabricated devices were stored in the glove box until the measurement started. The front and back side views of the completed OLED samples is shown in Figure 3.3.

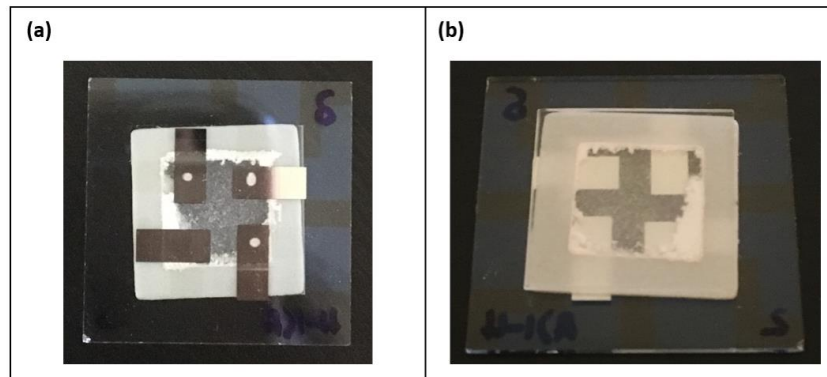


**Figure 3.3:** The (a) front and (b) back side of the completed OLED device.

## 3.3 Measurements of Electrical and Optical Properties

### 3.3.1 UV-Vis Absorption and Photoluminescence

Photoluminescence (PL) is a radiative phenomenon in a molecule triggered by photoexcitation. When incident radiation has the equivalent or larger energy of electronic states in the molecule, electrons are excited to one of the higher excited states. These photo-excited electrons radiatively decay with a peak emission wavelength corresponding to the

energy difference between the ground and the excited states of the compound. For the absorption measurement, organic materials were dissolved into chloroform ( $\text{CHCl}_3$ ) in a quartz cuvette and were excited by a Xenon lamp. The intensity of absorbance and luminescence as a function of wavelength is recorded, whose spectroscopic results are useful to understand intrinsic optical properties of materials and the degree of energy transfer between host and dopant materials. The spectral scan for absorption and PL was carried out in the UV/Vis range from 220 nm to 800 nm.

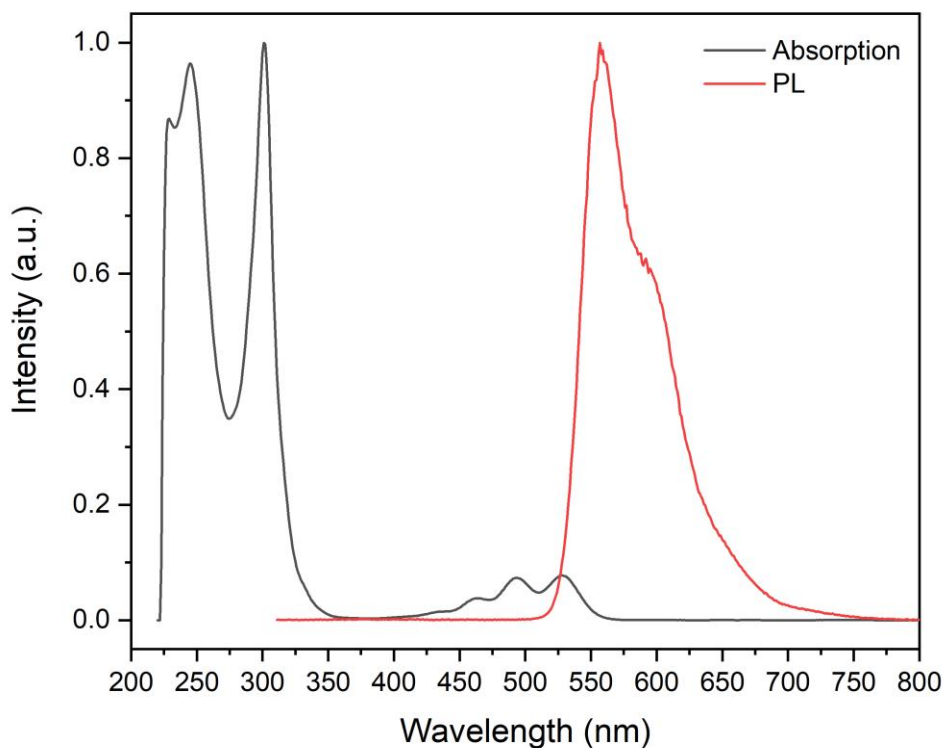


**Figure 3.4:** The absorption and PL spectra of red emitting material, 5,6,11,12-tetraphenyltetracene (Rubrene).

### 3.3.2 J-V-L Characteristics and Electroluminescence

The current density-voltage-luminance (J-V-L) measurement of OLEDs is simplest but the most important to understand a device's semiconducting characteristics. When a forward voltage was applied to a device, current and luminance were detected concurrently. The applied voltage was controlled by a Keithley 238 and the luminescence and spectral analysis were collected by LMS PR-650 SpectraScan colorimeter. With the calculation of these experimental values, luminous, power and external efficiencies of OLEDs were determined. The J-V-L measurement setup and devices mounted onto the jig are shown in Figure 3.5.

EL spectral results give insight into the luminescent characteristics of a given device as a function of wavelength, similar to PL, however, the electrons are excited electrically, which differentiates between the two spectroscopic methods. The luminescence from OLEDs is attributed to the energy conversion from electrical to optical energy so, EL spectroscopy is a source to understand the optical properties of devices. All measurements were carried out at room temperature under ambient conditions.

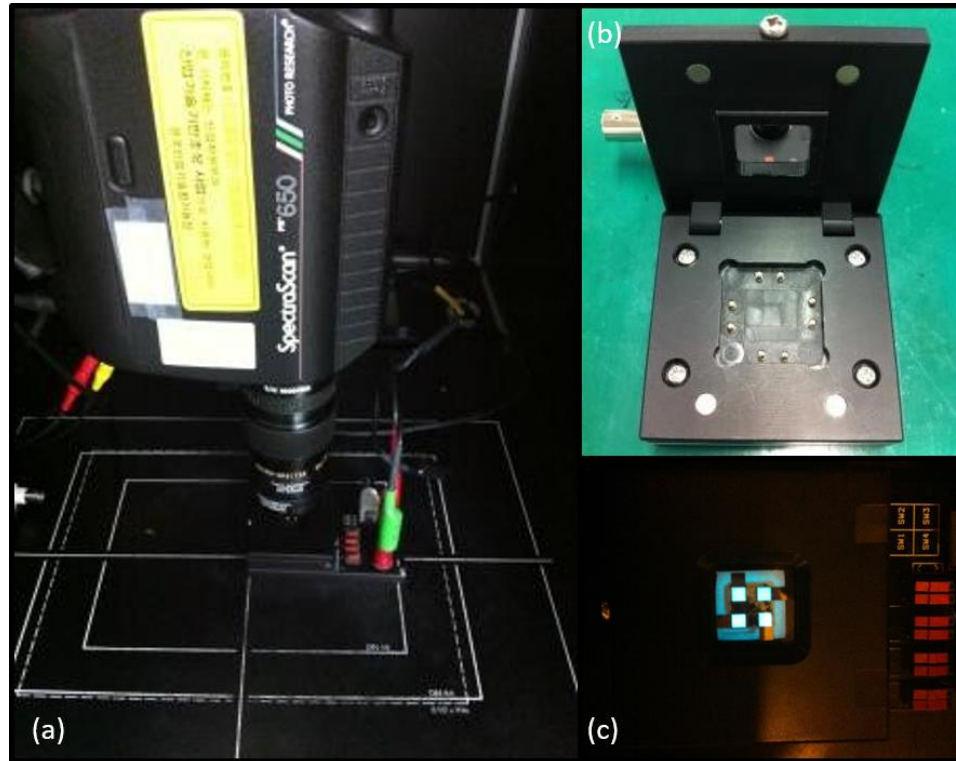


**Figure 3.5:** (a) J-V-L measurement setup, (b) jig to hold samples and (c) an emissive device when the voltage is applied.

### 3.4 Efficiency Metrics

Device efficiency is an important performance factor to evaluate display applications and lighting. OLED performance can be characterized by several efficiency metrics such as luminous, power, and external quantum efficiencies.

Firstly, luminous efficiency ( $\eta_{LE}$ ) is the most widely used parameter and its unit is candelas per ampere (cd/A). This quantity is determined by the relation of measured luminance ( $L_0$ ) with current density passing ( $J_p$ ) through a given device. The luminous efficiency is given by the following equation:

$$\eta_{LE} = \frac{L_0}{J_p} [cd/A] \quad \text{Eq. 3.1}$$

Power efficiency ( $\eta_{PE}$ ) is the ratio of the light output ( $L_p$ ) in the forward direction and the total input electrical power in a device ( $I_{OLED}V$ ) and its unit is lumen per watt (lm/W).

$$\eta_{PE} = \frac{L_p}{I_{OLED}V} [lm/W] \quad \text{Eq. 3.2}$$

EQE ( $\eta_{ext}$ ) is defined as a fraction of the number of extracted photons to the number of injected electrons and is calculated as follows:

$$\begin{aligned} \eta_{ext} &= \frac{\# \text{ of extracted photons out of device}}{\# \text{ of injected electrons into device}} \quad \text{Eq. 3.3} \\ &= \eta_{int} \times \eta_{outcoupling} \\ &= \gamma \times \phi_{PL} \times r_{st} \times \eta_{outcoupling} \end{aligned}$$

Here, IQE ( $\eta_{int}$ ) indicates the total number of photons generated inside a device per the number of injected electrons, so this term shows how efficiently photons are created in a device. The factors that determine the IQE of devices are the charge carrier balance ( $\gamma$ ), the PL quantum yield of a given material ( $\phi_{PL}$ ), and the fraction of the overall exciton formation ( $r_{st}$ ). The fraction of radiative exciton formation ( $r_{st}$ ) differs by emitter types; for example, it is 0.25 from fluorescent emitters and unity from phosphorescent and TADF emitters. The PL quantum yield ( $\phi_{PL}$ ) and the fraction of radiative excitons ( $r_{st}$ ) are related to material properties. The charge balance ( $\gamma$ ) on the other hand, is related to device structures, indicating the ratio of injected electrons and holes in organic layers. This factor

can be increased up to unity by reducing the injection barriers at the electrode/organic or organic/organic interfaces and by matching the mobility of the holes and electrons. In addition to IQE, EQE is a parameter obtained by combining IQE and the out-coupling efficiency ( $\eta_{outcoupling}$ ). Since EQE represents the number of photons extracted from a device per number of injected electrons, it implies how many photons can escape from the device. Due to the total internal reflection caused by different indices between an organic material and an electrode, photons are potentially trapped inside the device.

### 3.5 CIE Color Coordinates

Perceiving colors is a psychological response of the human eye, so a numerical description of colors is required to characterize device performance in color. Because any color is a combination of the three primary colors, red, green and blue, the Commission Internationale de L'Eclairage (CIE) system that is based on spectral response of light in three different wavelength regions is widely used as the standard for color specification.

The color coordinates  $x$ ,  $y$  and  $z$  are defined by

$$\begin{aligned} x &= \frac{X}{X + Y + Z} \\ y &= \frac{Y}{X + Y + Z} \\ z &= \frac{Z}{X + Y + Z} = 1 - x - y \end{aligned} \quad \text{Eq. 3.4}$$

The color coordinates of  $(x, y)$  are used to characterize colors of OLEDs. The tristimulus values ( $X$ ,  $Y$  and  $Z$ ) for a color are calculated by integrating the spectral irradiance ( $s(\lambda)$ ) and color matching functions denoted as  $\bar{x}(\lambda)$ ,  $\bar{y}(\lambda)$  and  $\bar{z}(\lambda)$ :



$$X = \int s(\lambda)\bar{x}(\lambda)d\lambda \quad \text{Eq. 3.5}$$

$$Y = \int s(\lambda)\bar{y}(\lambda)d\lambda$$

$$Z = \int s(\lambda)\bar{z}(\lambda)d\lambda$$

The color matching functions are displayed in Figure 3.6 and represent sensitivities of the human eye to each color of light. Particularly,  $\bar{y}(\lambda)$  is the normalized photopic response and its peak is placed at 555 nm. The CIE chromaticity chart is shown in Figure 3.7.

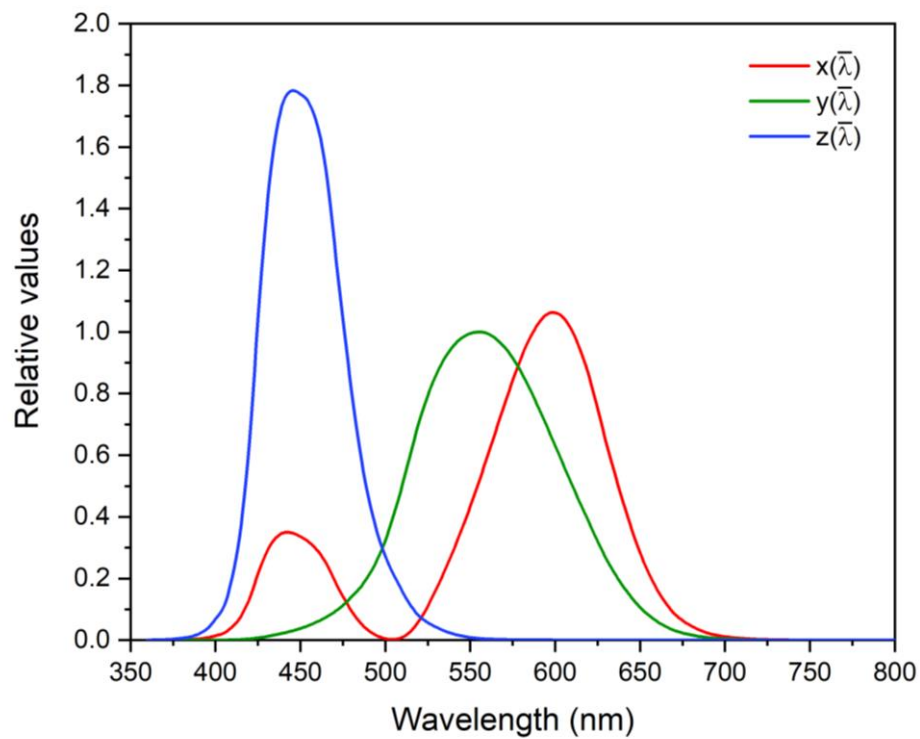


**Figure 3.6:** The color matching functions of the CIE 1931 color system.

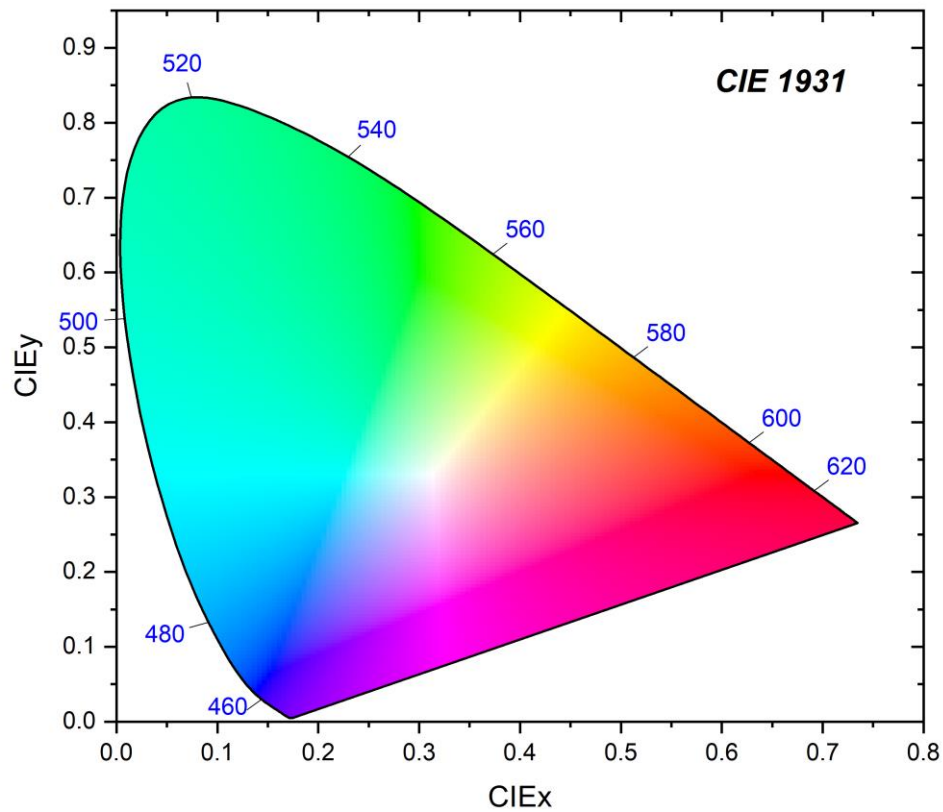


**Figure 3.7:** CIE 1931 chromaticity diagram of the common standard illuminants. The solid line indicates monochromatic colors with the corresponding wavelengths. The standard white emission is represented at (0.33, 0.33).

## **Chapter 4.**

# **Material Selection and Material Properties of Fluorescent and Phosphorescent Emitters**

As one of three primary colors, blue emission is an indispensable component to produce both full-color displays and white light sources and requires balanced device performance with red and green emission in efficiency, stability and color purity for high quality applications. However, for blue emitters there are difficulties in material development and in finding suitable host materials to satisfy energy transfer because of their intrinsic wide energy bandgap. In addition, low-lying HOMO and high-lying LUMO energy levels for deep blue emission hinder carrier injection, resulting in inefficient carrier injection into emitting region and a high operating voltage. The deep blue PHOLED is defined as having a CIE coordinate  $y < 0.15$  along with  $x+y < 0.30$  [25] and the color coordinates of the National Television System Committee (NTSC) for standard blue are (0.14, 0.08). In this chapter we discuss the organic materials used for the research work,

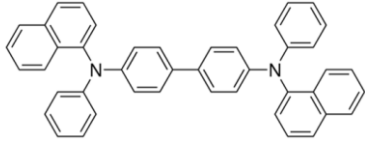
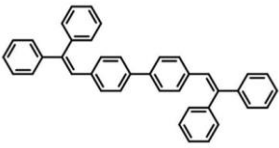
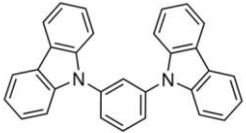
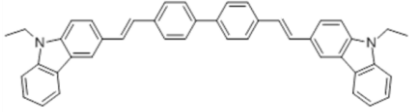
with their energy levels and functions in the device, and provide the materials properties of the three organic emitting materials created the EMLs.

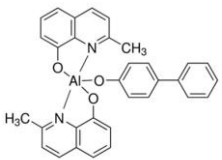
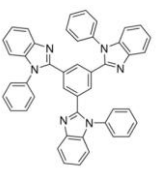

#### **4.1 Materials Selection for OLED Device Fabrication**

OLED devices are typically composed of multiple organic layers for the improvement in their performance. The molecular structures, chemical names and abbreviations of the organic materials used in the research work are summarized in Table 4.1. Their corresponding HOMO/LUMO energy levels, triplet energy levels, and functions are also included.

For hole transport materials, both a low ionization potential for facilitating hole injection as well as a high hole mobility are required. All of the OLEDs introduced in this thesis have the same hole transport material, NPB (see Table 4.1). Widely known and used as a hole transporting material, its HOMO energy level is -5.4 eV and its hole mobility is  $2.7 \times 10^{-4} \text{ cm}^2/\text{Vs}$  at  $0.3 \text{ MV}/\text{cm}^2$  [26]. Hole mobility in organic materials, in general, is one order of magnitude higher than electron mobility so carrier imbalance in potential emitting regions hinders effective exciton creation. One of approaches to achieving carrier balance is the use of a blocking layer that prevents leakage toward the electrodes. Generally, charge transport layers play a role as blocking layers with deep lying HOMO/LUMO energy levels. In this research work, two different materials, TPBi and BAlq (see Table 4.1) were used for this function. The electron mobilities of TPBi and BAlq are  $3.3 \times 10^{-5} \text{ cm}^2/\text{Vs}$  at  $0.47 \text{ MV}/\text{cm}^2$  [27] and  $3.1 \times 10^{-5} \text{ cm}^2/\text{Vs}$  [28] at  $1.0 \text{ MV}/\text{cm}^2$ , respectively.

**Table 4.1:** List of organic materials that have been employed in this work for OLED fabrication.

Organic Material	HOMO (eV)	LUMO (eV)	E <sub>s</sub> (eV)	E <sub>T</sub> (eV)	Ref.
 <p>N,N'-Di(1-naphthyl)-N,N'-diphenyl-(1,1'-biphenyl)-4,4'-diamine (<b>NPB</b>)</p> <p><b>HTL</b></p>	-5.4	-2.4	2.9	2.3	[29], [30]
 <p>4,4-bis(2,2-diphenylvinyl)-1,1-diphenyl (<b>DPVBi</b>)</p> <p><b>F-host</b></p>	-5.9	-2.8	3.08	2.2	[31]
 <p>1,3-Bis(N-carbazolyl)benzene (<b>mCP</b>)</p> <p><b>P-host</b></p>	-5.9	-2.4	-	2.9	[32], [33]
 <p>4,4'-Bis(9-ethyl-3-carbazovinyleno)-1,1'-biphenyl (<b>BCzVBi</b>)</p> <p><b>F-dopant</b></p>	-5.4	-2.4	2.98	1.81	[31], [34]

Organic Material	HOMO (eV)	LUMO (eV)	E <sub>s</sub> (eV)	E <sub>T</sub> (eV)	Ref.
 <p>Bis(8-hydroxy-2-methylquinoline)-(4-phenylphenoxy)aluminum (<b>BAIq</b>)</p> <p><b>ETL</b></p>	-5.9	-3.0	2.6	2.18	[35]
 <p>2,2',2''-(1,3,5-Benzinetriyl)-tris(1-phenyl-1H-benzimidazole) (<b>TPBi</b>)</p> <p><b>ETL/ P-host</b></p>	-6.2	-2.7	-	2.73	[36]
 <p>Bis[2-(4,6-difluorophenyl)pyridinato-C2,N](picolinato)iridium(III) (<b>Firpic</b>)</p> <p><b>P-dopant</b></p>	-5.8	-2.9	-	2.62	[7]

- F- and P- represent fluorescent- and phosphorescent-, respectively.

## 4.2 Materials Properties of Blue Emitting Materials

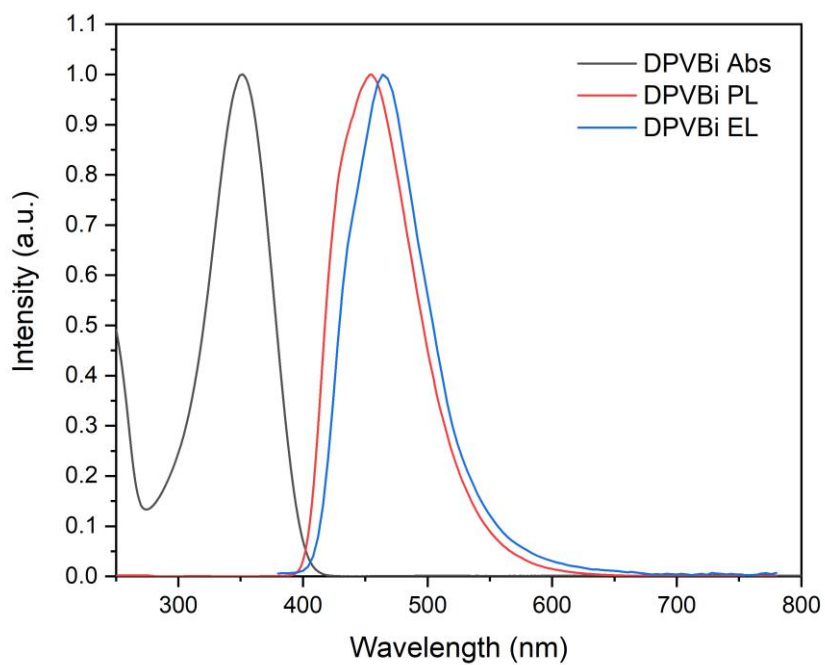
Besides the charge transporting materials, all the devices contained the same blue emitting materials. All the EMLs are created based on the host-dopant system. For the fluorescent EML, DPVBi was used as a host material and doped with a dopant material, BCzVBi. Flrpic was adopted as a dopant for the phosphorescent EML, into mCP. This section describes in more detail the properties of two blue fluorescent materials, DPVBi and BCzVBi, and one phosphorescent one, Flrpic, that have great influence on the performance of the blue OLEDs in this thesis.

### 4.2.1 4,4 -bis(2,2 -diphenylvinyl)-1,1 -diphenyl (DPVBi)

DPVBi is a well-known blue fluorescent emitting material and is used as the host material in this work. It is one of distyrylarylene (DSA) derivatives which is the most promising blue emitting material and was first reported by Hosokawa et al. [37]–[39]. The molecular structure with two nonplanar phenyl rings at both ends prevents forming exciplex and charge transfer complexes at the charge transport layer and EML [31], [40]. The HOMO/ LUMO energy levels of DPVBi are -5.9 eV/ -2.8 eV, respectively as shown in Table 4.1. The luminescent spectra and the corresponding data of DPVBi are shown in Figure 4.1 and Table 4.2, respectively.

**Table 4.2:** Summary of spectral data of DPVBi

$\lambda_{\max}$ (nm)			FWHM (nm)
Abs	PL	EL	
351	455	464	$72.8 \pm 1.4$

**Figure 4.1:** The absorption and PL spectra of DPVBi and an EL spectrum from a DPVBi-based device (ITO/ NPB (70 nm)/ DPVBi (30 nm)/ BPhen (30nm)/ Liq/ Al).



#### 4.2.2 4,4'-Bis(2-(9-ethyl-9H-carbazol-3-yl)vinyl)-1,1'-biphenyl (BCzVBi)

In addition to DPVBi, another fluorescent emitting material, BCzVBi, is employed as a dopant. The material is a DSA amine dopant, containing carbazoyl groups at both ends of the molecules so that its hole mobility is as large as  $10^{-3} \text{ cm}^2/\text{Vs}$  (at 1-3 MV/cm) as obtained by EL transient measurements from the structure: ITO/ BCzVBi (120 nm)/ Mg:Ag [40], [41]. When BCzVBi is doped into DPVBi, the emission mainly originates from the energy transfer process. As explained in the previous chapter, fluorescent doped devices realize higher luminescent efficiency via Förster energy transfer which is strongly dependent on the spectral overlap between the PL of host material and the absorption of dopant material. The absorption and PL spectra of these two materials are shown in Figure 4.2 and the following figure shows the EL spectrum of BCzVBi-doped devices.

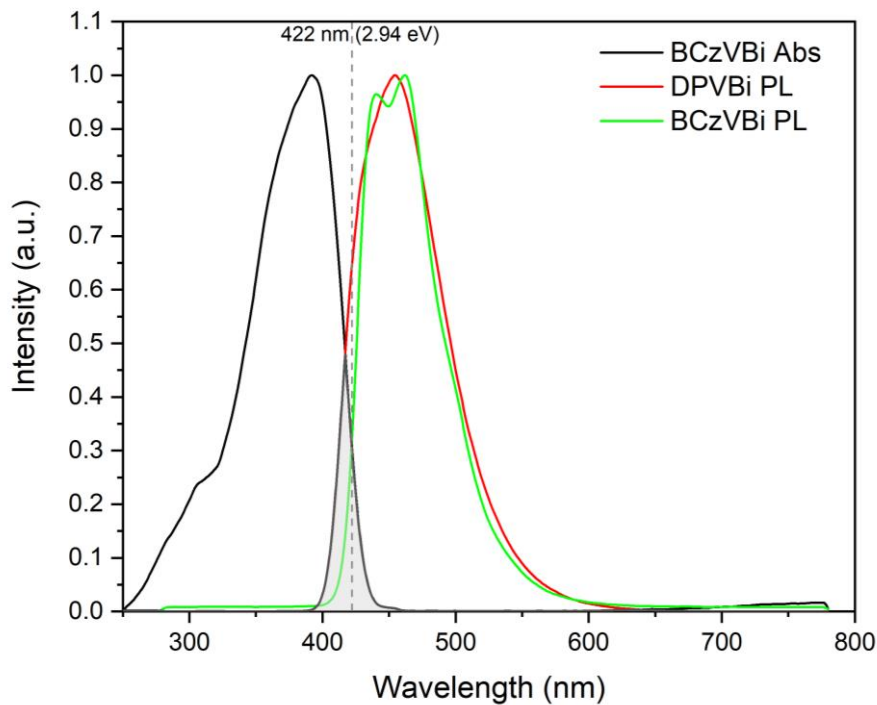


**Figure 4.2:** Absorption and PL spectra of BCzVBi and PL spectrum of DPVBi.

In the EL spectrum there are two distinct peaks and one shoulder peak; the main peak at 472 nm, the secondary peak at 448 nm and the shoulder peak at 508 nm, as seen in Figure 4.3. Neng Liu et al. reported that the intensity of the short-wavelength peak decreases as the BCzVBi doping concentration increases [42] and is related to energy transfer according to the report by Du et al. [43].

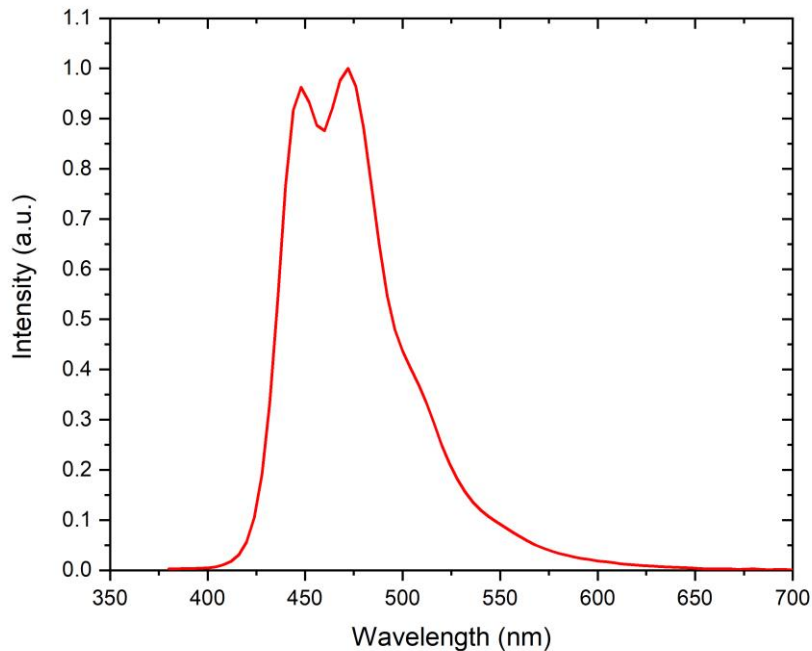


**Figure 4.3:** The EL spectrum of a BCzVBi-doped device with the structure of ITO/ NPB (70 nm)/ DPVBi:BCzVBi (15%, 30 nm)/ BPhen (30 nm)/ Liq/ Al.

A previous report by Hosokawa et al. showed that the device with the use of amino-substituted DSA dopant has a factor of 2 higher device efficiency (1.5 lm/W) than the non-doped device (DPVBi only, 0.7~0.8 lm/W) [31]. The experimental results also showed that

the presence of one of the DSA-amine dopants (BCzVBi) in the DPVBi layer enhanced the power and luminous efficiencies as shown in Figure 4.4.

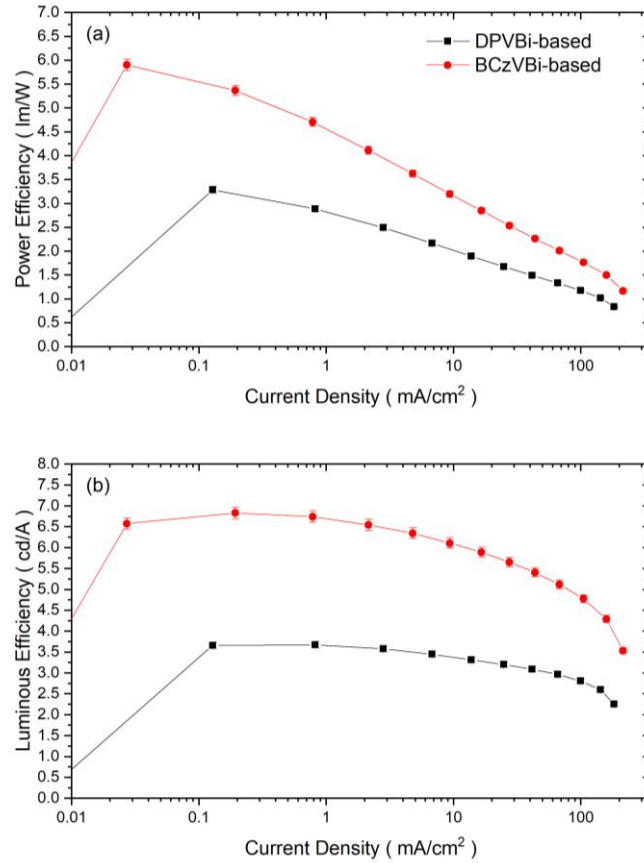


**Figure 4.4:** (a) Power efficiency and (b) luminous efficiency of DPVBi-based and BCzVBi-doped devices. The structure of the DPVBi-based device is ITO/ NPB (70 nm) /DPVBi (30 nm)/ BPhen (30 nm)/ Liq/ Al and that of the BCzVBi-doped device is ITO/ NPB (70 nm)/ DPVBi:BCzVBi (15 %, 30 nm)/ BPhen (30 nm)/ Liq/ Al. Adapted from [44], [45].

**Table 4.3:** Current density and efficiency of DPVBi-based and BCzVBi-doped devices at 6 V.

	J (mA/cm <sup>2</sup> )	L (cd/m <sup>2</sup> )	LE (cd/A)	PE (lm/W)
DPVBi-based	24.9	795	3.20	1.68
BCzVBi-doped	9.33	570	6.10	3.20

### **4.2.3 Bis[2-(4,6-difluorophenyl)pyridinato-C2,N](picolinato)Iridium(III)**

#### **(FIrpic)**

FIrpic is a bis-cyclometalated Iridium complex and most widely used as a sky-blue phosphorescent dopant. The emission color of Iridium complex phosphorescent emitters can be adjusted by changing ligands. In fact, as a modified molecule from Ir(ppy)<sub>3</sub>, FIrpic is created by the introduction of the electron withdrawing fluorine complex, leading to lowering the HOMO level for high triplet energy [7], [46] and by a change of the ancillary ligand to the picolinate (pic) one. The different ancillary ligands impact emission color and quantum efficiency. As can be seen in Table 4.1 FIrpic has HOMO and LUMO energy levels of -5.8 eV and -2.9 eV, respectively and has a triplet energy level of 2.62 eV [7].

For the realization of high luminescence from FIrpic, a host material needs to have a higher triplet energy level and its PL spectrum a significant overlap with FIrpic's absorption spectrum. Previous work by Kawamura et al. [47] demonstrated that the PL quantum efficiency improved when FIrpic was doped into mCP by preventing non-radiative decay via back energy transfer to CBP whose triplet energy level is lower than FIrpic's and the maximum PL quantum yield of the mCP:FIrpic films reaches nearly 100 % [47] as displayed in Figure 4.5.

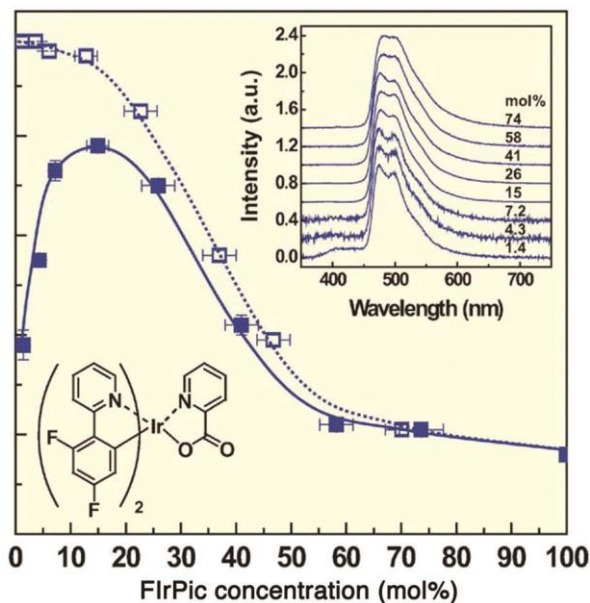


**Figure 4.5:** PL quantum efficiency as a function of dopant concentration in CBP:FIrpic [filled squares] and mCP:FIrpic [open squares] films. The inset shows PL spectra of CBP:FIrpic measured at given dopant concentrations from 1.4 ~74 mol%. Reprinted with permission from [47].

The phosphorescent EML in this thesis was composed of FIrpic doped into mCP, whose triplet energy level is 2.9 eV [33], which makes possible exothermic energy transfer to FIrpic. This can be achieved by the large spectral overlap between the fluorescent band of the  $^1\text{LC}$  (ligand-centered) state of mCP and the absorption bands of both  $^1\text{MLCT}$  (singlet metal-to-ligand charge transfer) and  $^3\text{MLCT}$  (triplet metal-to-ligand charge transfer) states from FIrpic [48]. The absorption and PL spectra of FIrpic and mCP are given in Figure 4.6. The excitonic energy transfer can occur from the lowest singlet excited state in mCP to either the lowest triplet-excited states or the lowest singlet excited state in FIrpic [48]. In the latter case, further transition to the lowest triplet excited state in FIrpic occurs through ISC and those energy transfer processes are represented by Förster energy transfer via Coulomb interaction [35], [48], [49]. In addition, previous work [50] showed that the

phosphorescent spectrum of mCP is centered at around 430 nm and overlaps with the absorption band of  $^3\text{MLCT}$ s in FIrpic, resulting in Dexter energy transfer [51].

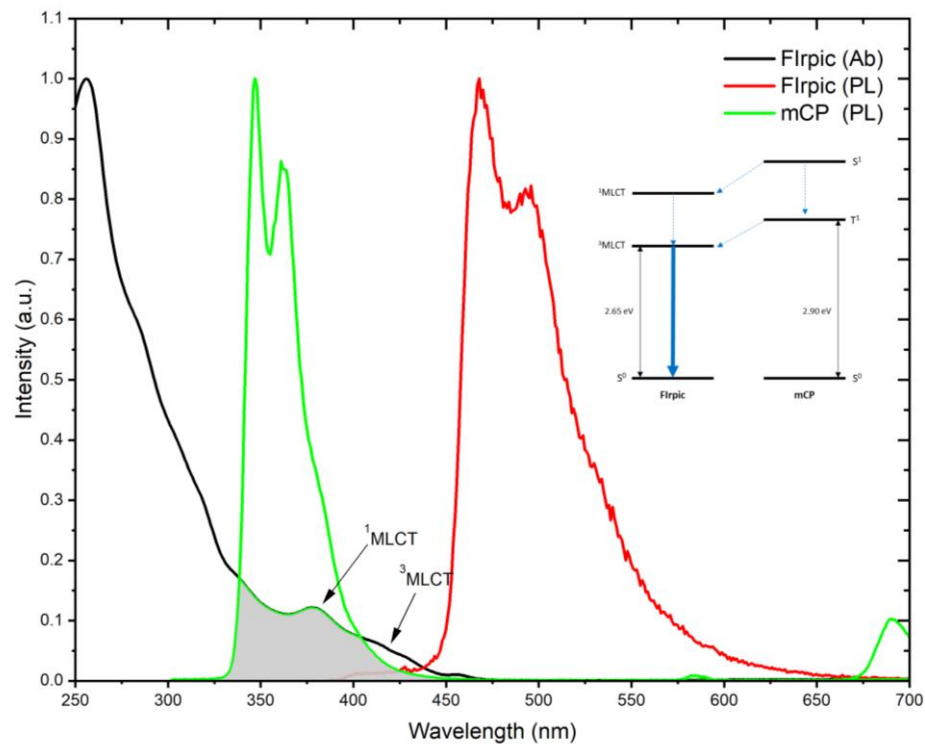


**Figure 4.6:** The absorption and PL spectra of FIrpic and the mCP PL spectrum. The inset shows possible energy transfer processes between mCP and FIrpic.

## **Chapter 5.**

# **Blue OLEDs with Either Uniformly or Step-Controlled Doping Strategies in Double EMLs**

The research work described in this chapter concerns blue OLEDs consisting of double EMLs which are individually doped with fluorescent and phosphorescent emitters. We aim to determine how the emitters and various doping strategies influence the electrical and optical properties of blue OLEDs. For this study, the layer arrangements and doping concentrations in the emitting region are regulated. This chapter is divided into two parts according to how the doping concentrations are controlled in the EMLs; either uniformly or step-controlled.

The work has been published in a peer-reviewed paper entitled “*Luminescence Characteristics of Hybrid Dual Emitting Layers in Blue Organic Light-emitting Diodes by Controlling the Fluorescent Doping Concentration,*” *Journal of Luminescence*, Volume 148, April 2014, Pages 72-78 [<http://dx.doi.org/10.1016/j.jlumin.2013.11.065>] and in a proceedings paper

entitled “*Characterization of Hybrid Dual Emitting Layers in Blue Organic Light-emitting Diodes (OLEDs) by Controlling the Fluorescent Doping Concentration,*” Cambridge (2013) MRS Spring Meeting, 2013 [<https://doi.org/10.1557/opl.2013.625>]. The study on the step-controlled doping profile has been published in a peer-reviewed paper entitled “*Study on Hybrid Blue Organic Light Emitting Diodes with Step Controlled Doping Profiles in Phosphorescent Emitting Layer,*” *Optical Materials* Volume 86, 2018 Pages 498-504 [<https://doi.org/10.1016/j.optmat.2018.09.039>].

## 5.1 Introduction

Considering the determining factors in IQE (of OLEDs), the intrinsic fluorescent quantum yield ( $\phi_{PL}$ ), and the fraction of radiative excitons ( $r_{st}$ ) correlate with material properties while the charge carrier balance factor ( $\gamma$ ) is dependent on material properties as well as a device’s structural design. The balance factor represents how well-balanced the electron and hole population is in an effective emitting region, which strongly correlates with the probability of exciton creation in a given device. Several approaches to engineering device structures have been reported to improve device efficiency; for example, utilizing mixed-host structures [52], [53], multiple EMLs [52] including quantum well structures [54], [55], and step-graded [56]–[59] or linearly graded EML [60] structures. Among these device design approaches the latter two example cases are based on the host-dopant system for EMLs created by co-evaporating a certain portion of a dopant material into a suitable host material. This particular type of layering is capable of transferring the excitonic energy from the host material to the highly emissive and stable dopant emitter, which prevents non-radiative decay, ultimately resulting in the enhancement of device



efficiency. In addition, it is useful to generate desired colors by adjusting dopant materials and their concentrations.

According to spin statistics, there are two possible pathways for luminescence in organic materials: fluorescence and phosphorescence. These two luminescent pathways are differentiated by not only a different radiative relaxation process upon excitation but also distinct performance characteristics in color, efficiency etc. On the one hand, the theoretical IQE of phosphorescent materials reaches 100 % based on the harvest of both singlet and triplet excitons [8], [61], [62]. In contrast to the beneficial aspect in efficiency, phosphorescent materials are challenged by efficiency roll-off by triplet-triplet or triplet-polaron annihilations due to the long lifetime of triplet excitons [63] in particular, one of the challenges that remains to be overcome in the engineering of blue phosphorescent emitters [9], [61] is the color quality due to the fact that these materials require a high triplet energy level for blue emission [8]. On the other hand, blue fluorescent materials show deeper blue emission although their IQE is limited to 25 % by collecting only singlet excitons for emission [64], [65]. Because of these distinct characteristics between the two different types of emitters, a hybrid EML structure has been widely utilized for white OLEDs with a combination of red and green phosphorescent and blue fluorescent emitters. With regard to blue OLEDs, most research has been carried out and focused on either fluorescent or phosphorescent emitters only. Unlike hybrid white OLEDs, few studies on blue OLEDs with both fluorescent and phosphorescent emitting materials have been reported [66]–[73].

In this chapter we propose and discuss blue OLED devices with double EMLs doped with both fluorescent and phosphorescent emitting materials and explore device performance from the point of view of the variation in doping profiles and different EML configurations. The chapter is divided into two main parts in accordance with doping strategies, either uniformly or step-graded controlled. The effects of dopants, EML structures and step-controlled doping distributions are studied for a better understanding of the device physics for blue OLEDs with both types of emitters.

## 5.2 Uniformly Doped EMLs for Blue OLEDs

### 5.2.1 Device Fabrication: Device Structures and Doping Profiles

All devices were fabricated by thermal evaporation and measured by the techniques mentioned in Chapter 3. Organic layers were deposited in a vacuum chamber under high vacuum condition,  $\sim 10^{-7}$  Torr and the measurement was carried out at room temperature after encapsulation.

All the fabricated devices have a common standard device structure and are differentiated by EML configurations and various doping distributions. The standard device structure of blue OLEDs introduced in this chapter is as follows: *ITO / NPB* (70 nm)/ *double EMLs* (30 nm)/ *BAIq (or TPBi)* (30 nm)/ *Liq* (2 nm)/ *Al* (100 nm). The blue OLEDs are structurally classified into two types in accordance with the EML configurations, or more specifically depending on the order of fluorescent (F) and phosphorescent (P) EMLs from the anode side; F-P and P-F EMLs. The F-EML used DPVBi incorporated with BCzVBi and mCP doped with FIrpic for the P-EML. The

schematic energy level diagrams of organic layers in the OLED devices are displayed in Figures 5.1.

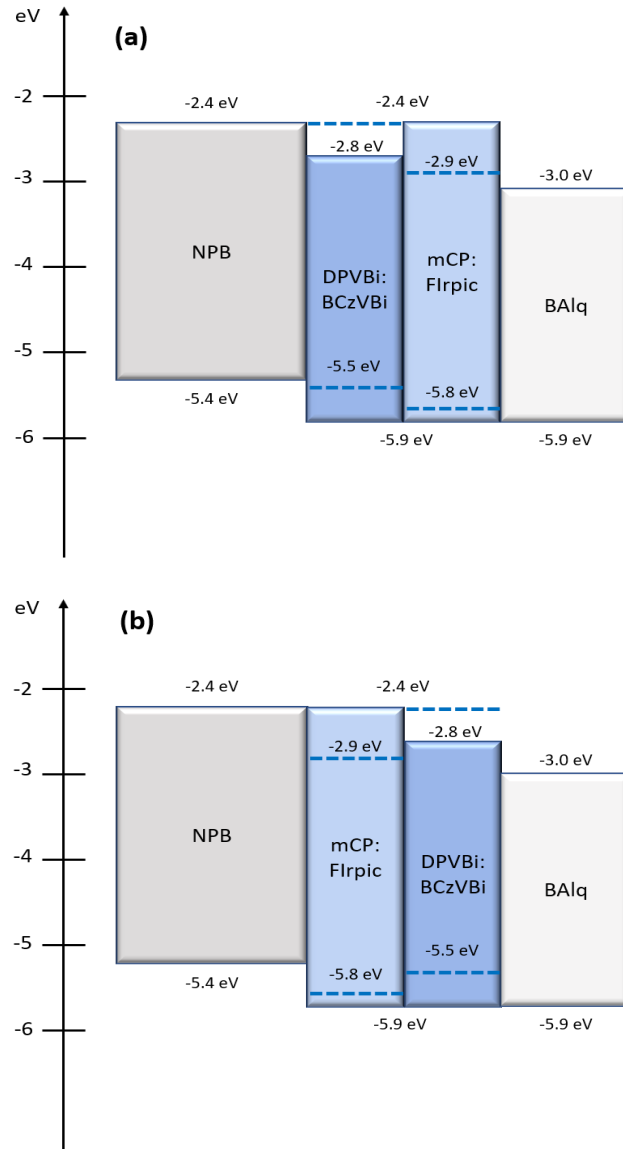


**Figure 5.1:** Energy level diagrams of organic layers in the blue OLEDs with BALq as the ETL (a) F-P structure and (b) P-F structure. The dashed line indicates the energy levels of dopant materials and the numbers are HOMO and LUMO energy levels of given materials. The triplet energy levels of the given organic materials are given in Table 4.1.

Apart from the different EML configurations, each device has a different doping concentration to study the effect of various fluorescent doping concentrations in the blue OLEDs. Devices are divided into two sets and are labelled as F-controlled F-P structures and P-F structures. When the fluorescent doping concentration changed from 15 % to 5 %, the phosphorescent one was fixed at 10 %. The dopant compositions of the EMLs in each device are summarized in Table 5.1.

**Table 5.1:** Doping profiles of blue OLEDs with F-P (devices A) and P-F (devices B) EML structures.

Device #	Devices A (F-P structure)		Devices B (P-F structure)		Note
	F-EML	P-EML	P-EML	F-EML	
1-1	15%	10%	10%	15%	<i>Fluorescent doping- controlled</i>
1-2	12%			12%	
1-3	8%			8%	
1-4	5%			5%	

- The dopants are uniformly distributed in the EMLs, with the indicated doping concentrations.

### **5.2.2 Effects of Fluorescent Doping Concentrations**

The presence of dopant materials enables new charge transporting mechanisms as additional channels for carrier movement in organic layers, which can be described either by hopping or by trapping at the organic molecules [74], [75]. To be specific, these transporting characteristics are determined by the relative energy level offset between host and dopant materials. Direct carrier trapping at dopant sites could be found when there is a significant difference in HOMO and LUMO energy levels between host and dopant materials. Carrier hopping generally occurs via shallow states [76]–[78] and can be influenced by the doping concentration in a host material, which influences the distance between hopping sites. The possible hopping regimes in host-dopant system as per dopant concentration are described in Figure 5.2.

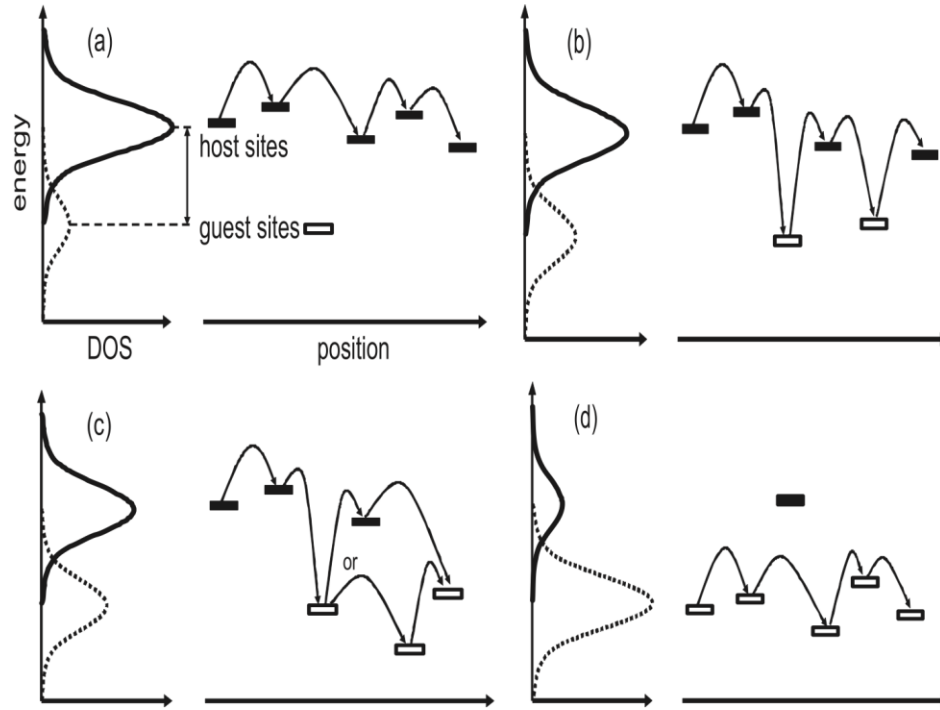


**Figure 5.2:** Various hopping cases in disordered host-dopant (guest) system. (a) Hopping between host molecules (no influence of dopant molecules), (b) hopping via host molecules coexisting with a small portion of dopant molecules (trap-limited transport), (c) hopping via both host and dopant molecules, and (d) hopping mainly via dopant molecules. The densities of states (DOS) of host (solid lines) and dopant (dotted lines) are also shown (left side of each panel). Reprinted with permission from [79].

### 5.2.2.1 Characterizations of the F-P EML Structure

As shown in Figure 5.1(a), the energy barrier between NPB and DPVBi is 0.5 eV where the large HOMO energy barrier results in limited hole injection into DPVBi molecules. Holes are favorably injected through the BCzVBi molecules because the energy barrier between NPB and BCzVBi is low, only 0.1 eV. The J-V-L characteristics of the F-P structured blue OLEDs with different fluorescent doping concentrations are plotted in

Figure 5.3 and Table 5.2 summarizes the performance of the devices at given conditions. It is found that the current density of the F-P EML structured devices are strongly dependent on the BCzVBi doping concentration and more specifically, the current density increases with increasing doping concentration owing to the reduced hopping distance between dopant molecules. Enhanced hole transport via hopping between BCzVBi molecules results in a better balance of electrons and holes in the EMLs so the luminance increases with increasing fluorescent doping ratio. The luminance of devices A1-1 and A1-2 shows little difference despite the increased doping concentration. When the doping concentration exceeds 12 %, devices tend to show increased non-radiative decay because of concentration quenching effects, resulting from dopant aggregation.

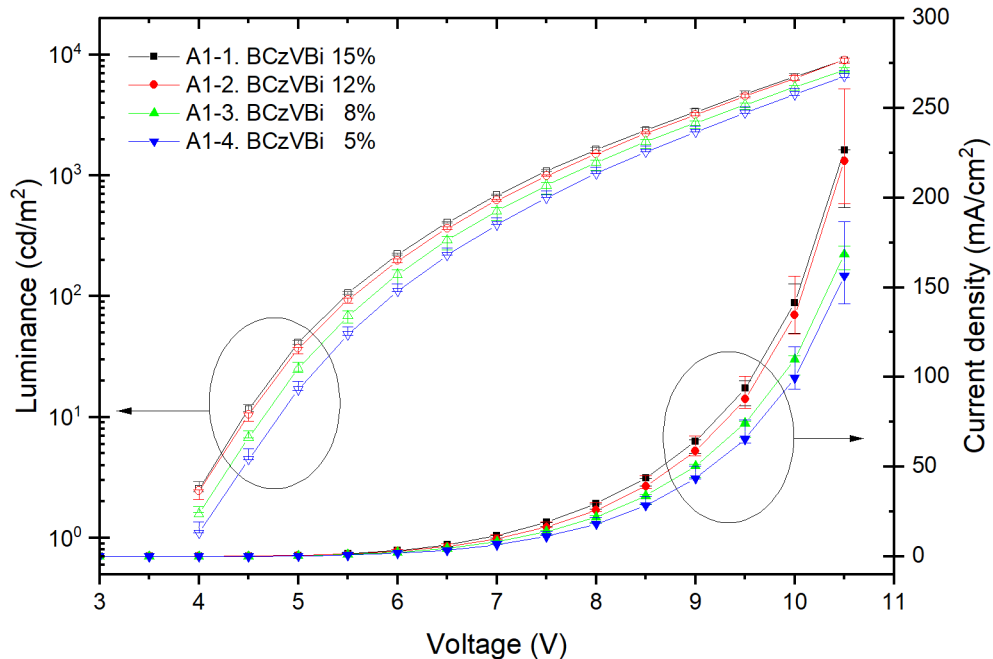


**Figure 5.3:** Current density and luminance of device set A1 as a function of voltage.

**Table 5.2:** J-V-L results and efficiencies of device set A1 (w/ F-P EML structure). The values of current density and luminance were measured at 10 V.

Device	J (mA/cm <sup>2</sup> )	L (×10 <sup>3</sup> cd/m <sup>2</sup> )	Max LE (cd/A)
A1-1	142	6.58	7.78
A1-2	135	6.40	8.11
A1-3	110	5.70	7.28
A1-4	99.6	6.58	6.75

Figure 5.4 shows the luminous efficiencies of devices A1-1 to A1-4 versus current density. The maximum luminous efficiency, 8.11 cd/A, was obtained from device A1-2. The luminous efficiency increased with increasing doping concentration and decreased at 15 % doping concentration. With increasing current density, the difference in luminous efficiency between the devices is reduced and becomes insignificant. The decrease in efficiency in device A1-1 with 15 % doping concentration is due to concentration quenching and carrier imbalance within the recombination zone, which leads to efficiency degradation at higher doping concentrations.



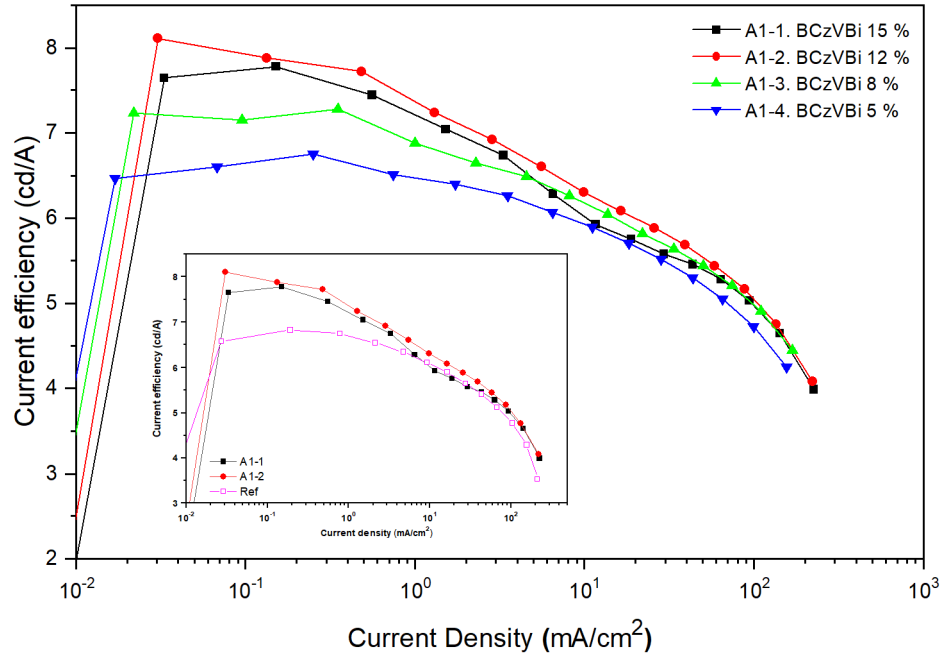


**Figure 5.4:** Luminous efficiency from device set A1 as a function of current density. The reference luminous efficiency is achieved from the blue fluorescent OLED with a single EML (DPVBi:BCzVBi (15 %)) as given in Figure 4.5 (b).

The EL mechanisms in OLEDs based on host-dopant system can be classified as either energy transfer between host and dopant materials or carrier trapping at the dopant sites [80], [81]. The EL spectra for devices with different BCzVBi doping concentrations are displayed in Figure 5.5 (a) and show major and shoulder peaks at 448, 472 and 496 nm, which mainly originate from BCzVBi and FIrpic. The EL peaks at 448 and 496 nm varied as a function of the BCzVBi doping concentration. More specifically, with increasing doping concentration, the intensity of the peak at 448 nm, originating from the F-EML, decreases while the intensity of the phosphorescence-related peak at 496 nm increases. This

indicates that the recombination zone for blue emission is spread over the interface of the F- and P-EMLs and is biased toward the P-EML with increasing doping concentrations and driving voltages due to hole transport via BCzVBi molecules. In other words, at low doping concentrations, charge carriers are more likely to be trapped at the dopant molecules, so this tendency causes the recombination for light emission to occur at the dopant sites. However, with increasing doping concentrations hole transport toward the neighboring layer is facilitated by hopping between the dopant molecules, resulting in an increased probability to form excitons in the neighboring layer. Also, hole injection and transport are facilitated by the hole transport type of the host materials, mCP and DPVBi in addition to the additional transport channels of BCzVBi. The normalized fluorescent intensity at 448 nm of each device decreases with increasing doping concentration and applied voltage and is saturated under forward as shown in the inset of Figure 5.5 (b).

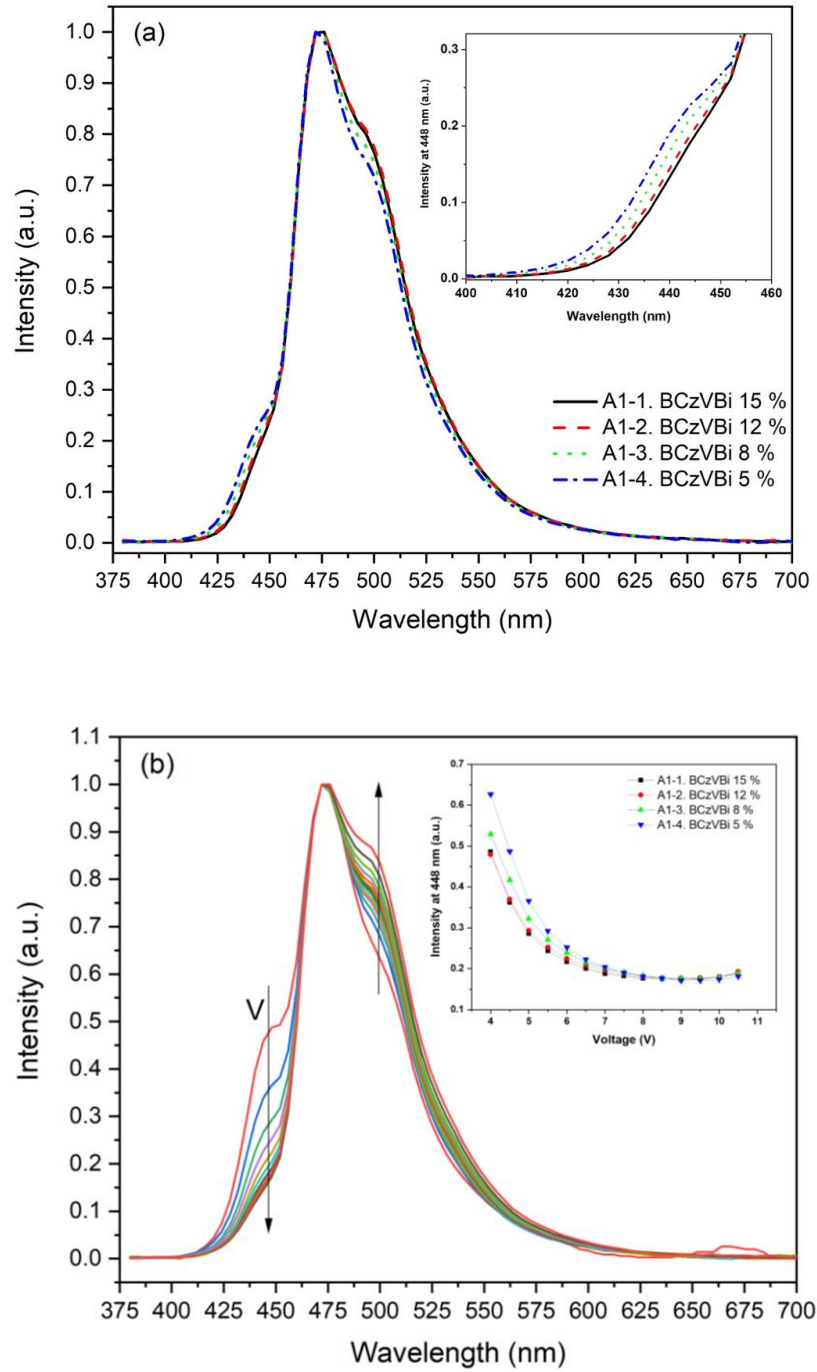


**Figure 5.5:** (a) EL spectra of device set A1 at 6 V (the inset is plotted from 420 nm to 456 nm) and (b) EL spectra of device A1-4 as a function of voltage (the inset is the normalized EL intensity at 448 nm of device set A1 as a function of voltage)

The CIE<sub>xy</sub> color coordinates of devices A1-1 to A1-4 are shown in Figure 5.6. The CIE x-coordinates of the fabricated blue OLEDs show little change at the different doping concentrations and as a function of the driving voltage, while the values of the CIE y-coordinates increase, which indicates emission in the longer wavelength region due to the predominant recombination at the phosphorescent EML. In terms of color purity, the color coordinates for device A1-4 with 5 % BCzVBi doping indicate the best blue emission among the devices in set A1, but their variation with voltage is the most significant. Table 5.3 shows CIE<sub>xy</sub> coordinates at 6 V and their changes with voltages.

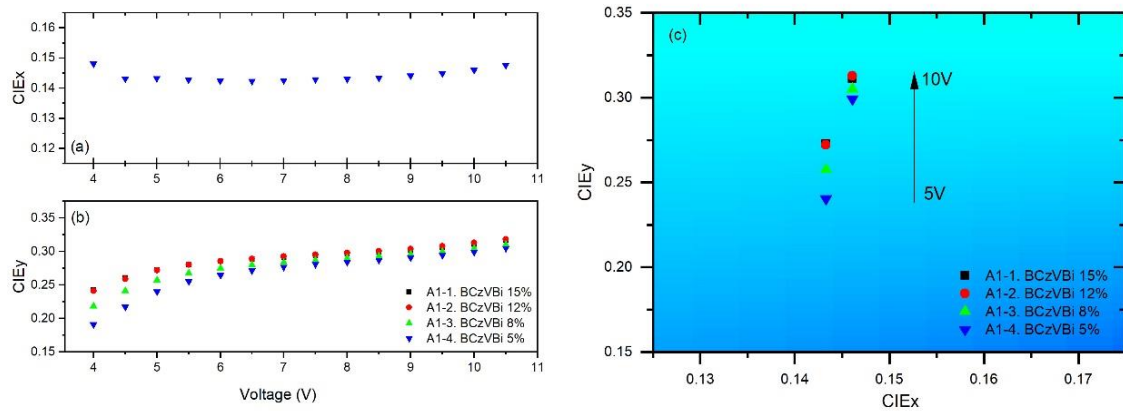


**Figure 5.6:** (a) CIE<sub>x</sub> and (b) CIE<sub>y</sub> color coordinates as a function of bias voltage and (c) CIE<sub>xy</sub> changes from 5 V to 10 V of devices A1-1 to A1-4.

**Table 5.3:** CIE<sub>xy</sub> color coordinates of device set A1 at 6 V and their variations when the voltage changes from 5 V to 10 V.

	CIE <sub>xy</sub> at 6 V	$\Delta$ CIE <sub>xy</sub>
Device A1-1	(0.143, 0.285)	(0.003, 0.038)
Device A1-2	(0.143, 0.286)	(0.004, 0.041)
Device A1-3	(0.142, 0.275)	(0.004, 0.047)
Device A1-4	(0.143, 0.255)	(0.003, 0.059)

### 5.2.2.2 Characterizations of the P-F EML Structure

As mentioned in the previous section, the fluorescent dopant molecules in the F-P EML structures play a role as additional hole transport channels, facilitating hole injection and transport into the EML region. When the arrangement of the two EMLs is switched, the different energy level alignment with neighboring organic materials gives rise to different carrier transport characteristics compared to the other EML structure despite the same doping concentration. Device performance including J-V-L characteristics and device efficiencies are summarized in Table 5.4 and Figure 5.7 shows current density and luminance as a function of the applied voltage. One can see that the current density of the devices remains almost the same and slightly increases at 5 % doping concentration. From the hole transport point of view, it is likely that holes can be transported via either host or dopant molecules by considering the HOMO energy level difference between BCzVBi and other neighboring materials (mCP, FIrpic and DPVBi) as seen in Figure 5.1 (b). In case of electrons, however, they are favorably injected and transported through DPVBi with a 0.1

eV LUMO energy level difference with BAq instead of BCzVBi, which has a higher energy barrier compared to DPVBi. Therefore, the transport of electrons is not as strongly affected by the presence of dopants or doping profiles as is hole transport. In addition to the current density, the luminance of device B1-4 is higher than other devices; however, there is no significant effect on various fluorescent doping concentration as can be seen in Figure 5.7 (b).

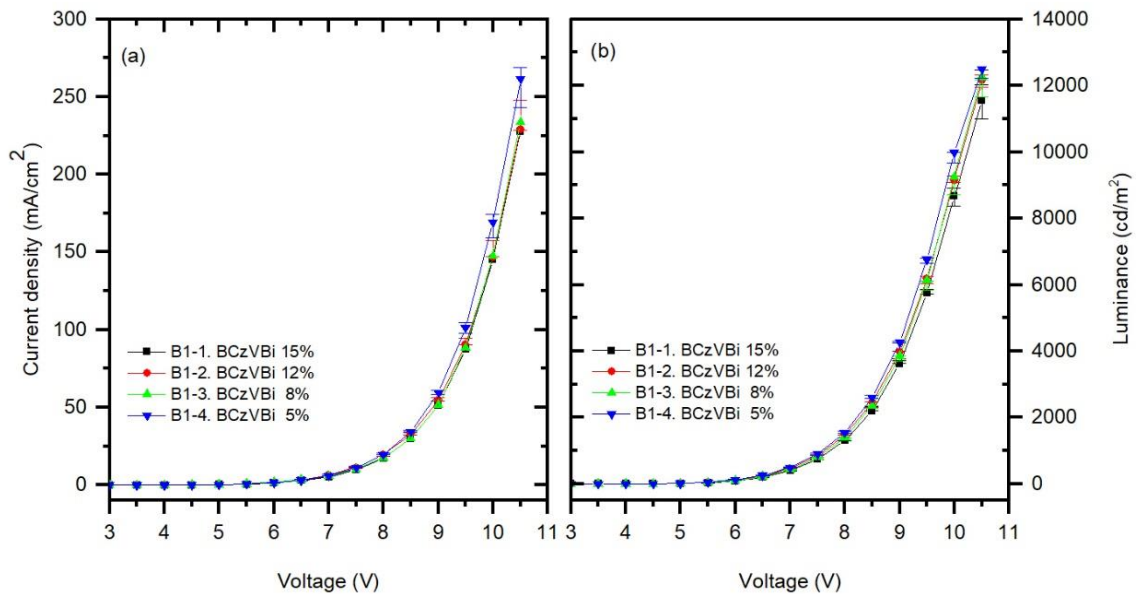


**Figure 5.7:** (a) Current density and (b) luminance of devices B1-1 to B1-4 as a function of the applied voltage.

The luminous efficiency of P-F EML devices as a function of current density is shown in Figure 5.8 and the semi-logarithmic inset graph shows the luminous efficiency when the current density is higher than 5 mA/cm<sup>2</sup>. Even though the maximum luminous efficiency, 8.17 cd/A, was achieved from device B1-4, at over 20 mA/cm<sup>2</sup> device B1-3

shows the highest luminous efficiency. Efficiency roll-off in a range of high current density is unavoidable; however, the most drastic efficiency roll-off was seen from device B1-4. The efficiency trend from B1-1 to B1-3 shows that increasing doping concentration results in lower efficiency due to the concentration quenching effect. Furthermore, the triplet exciton produced in the P-EML is possibly transferred to the triplet energy level in the F-EML because of the lower triplet energy level of BCzVBi than that of FIrpic (as given in Table 4.1) and consequently, the exciton can be dissipated non-radiatively. Also, additional efficiency degradation is found because of concentration quenching at 15 % doping concentration.

**Table 5.4:** J-V-L characteristics and efficiencies of devices in set B1 (w/ P-F EML structure). The values of current density and luminance were measured at 10 V.

Device	J (mA/cm <sup>2</sup> )	L ( $\times 10^3$ cd/m <sup>2</sup> )	Max LE (cd/A)
B1-1	145	8.67	7.63
B1-2	147	9.14	7.62
B1-3	148	9.25	7.90
B1-4	169	9.99	8.17

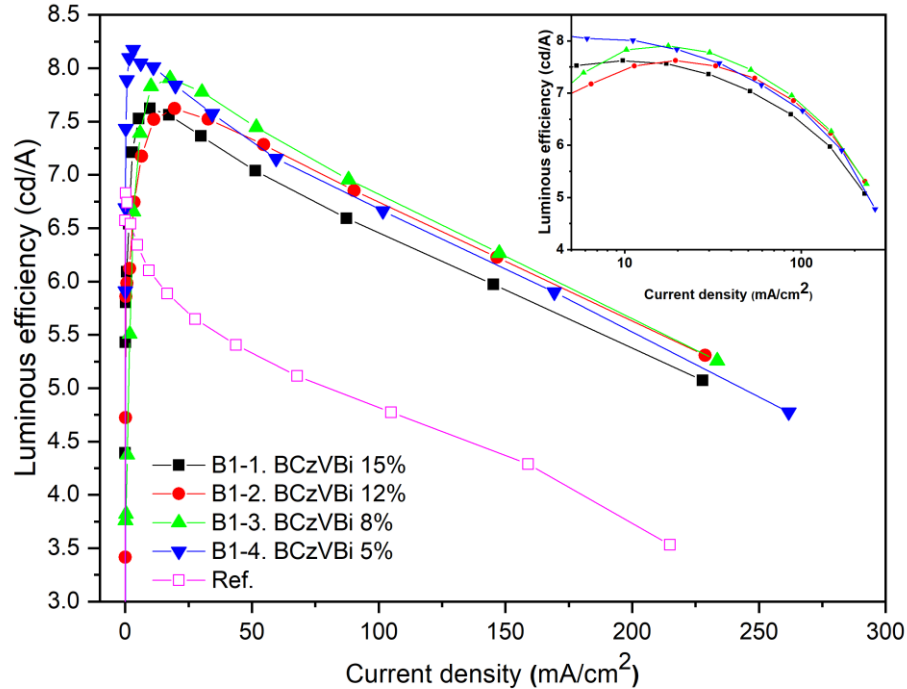


**Figure 5.8:** Luminous efficiency of devices B1-1 to B1-4 as a function of current density (Inset: luminous efficiency at current densities higher than 5 mA/cm<sup>2</sup> on a Log scale). The reference luminous efficiency is achieved from the blue fluorescent OLED with the single EML (DPVBi:BCzVBi (15 %)) as shown in Figure 4.5 (b).

As shown in Figure 5.9 (a), the intensity differences of the fluorescent emission between devices with various fluorescent doping profiles were not significant but the trend of intensity change at 448 nm is different to the F-P EML devices (A1 set), which enhanced with increasing doping concentration and voltage. The weak EL intensity from the F-EML results from increasing non-radiative decay due to the quenching effects at the F-EML. On the other hand, in the case of the phosphorescent emission, with increasing doping concentration the emission from the P-EML is slightly strengthened by a 12 % doping



concentration; however, it decreases at 15 % doping, which may be caused by the quenching effect from the F-EML. It is observed that in both EML structures one can tune their electron and hole recombination by adjusting the doping concentrations. Figure 5.9 (b) presents the EL spectra of device B1-4 with 5 % doping concentration as a function of the driving voltage. The increase in the density of electrons is less than that in the density of holes in the EMLs due to the nature of the hole transport type of DPVBi and the lower mobility of electrons compared to that of holes in organic materials. However, as the number of injected electrons into the EML region increases when the applied voltage increases, electron and hole recombination occurs more effectively in the EML region, which improves both fluorescence and phosphorescence.

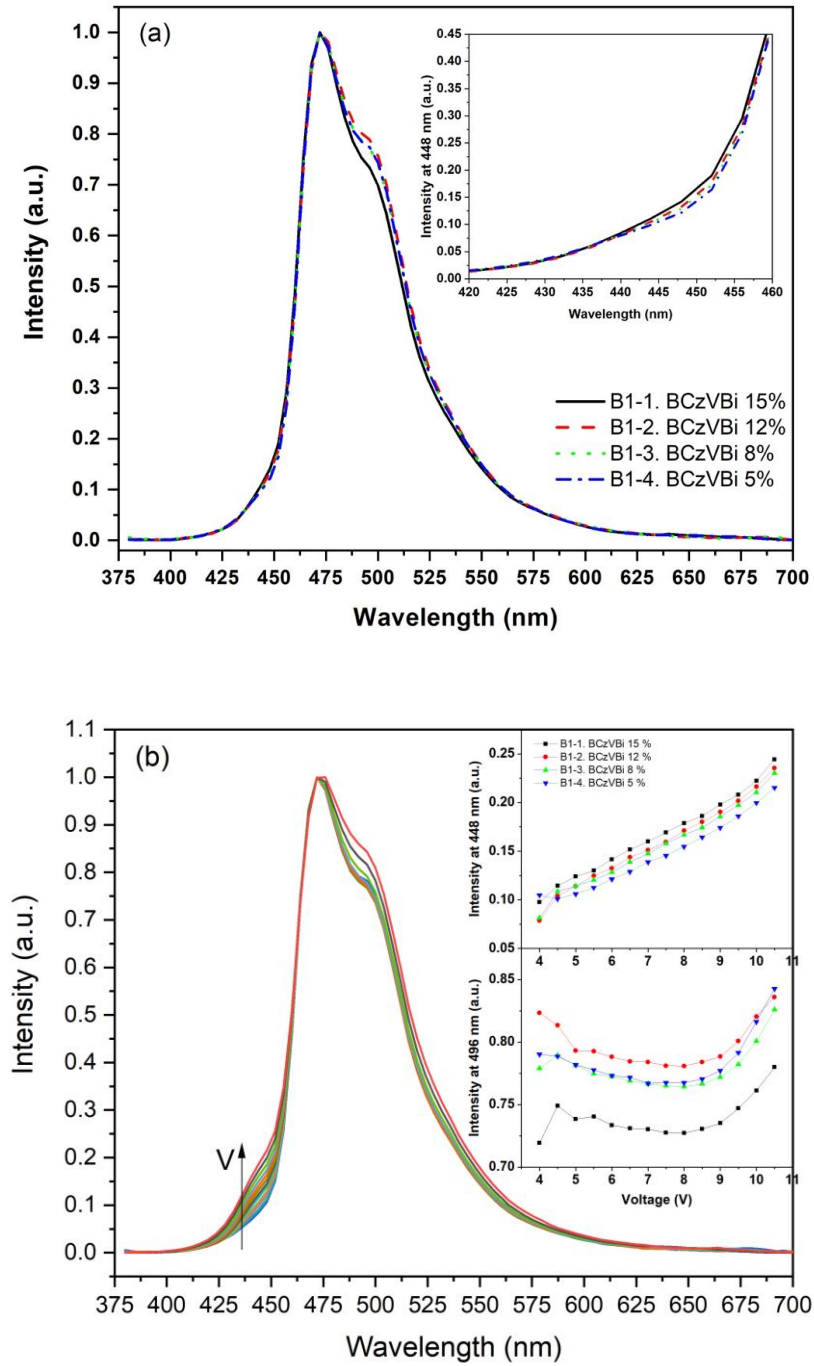


**Figure 5.9:** (a) EL spectra of devices B1-1 to B1-4 at 6 V (inset is plotted from 420 nm to 456 nm) and (b) EL spectra of device B1-4 as a function of voltage (The top and bottom insets are the EL intensity at 448 nm and 496 nm, respectively).

The CIE<sub>xy</sub> color coordinates as a function of applied voltage of devices B1-1 to B1-4 are shown in Figure 5.10 and their coordinates are displayed in Table 5.5. The CIE<sub>x</sub> coordinates of devices B1-1 to B1-4 show little change with increasing doping concentration while the CIE<sub>y</sub> coordinates of device B1-1 show slightly improved blue emission due to the lower phosphorescent emission compared to the other devices. The carrier mobility in organic layers is electric field dependent [82] and in general, electron mobility increases faster than hole mobility in organic layers [83]. When the applied voltage increases above 9 V, electron transport become more favorable so the probability for recombination further increases toward the P-EML, resulting in increasing CIE<sub>xy</sub> coordinates and the intensity at 496 nm.

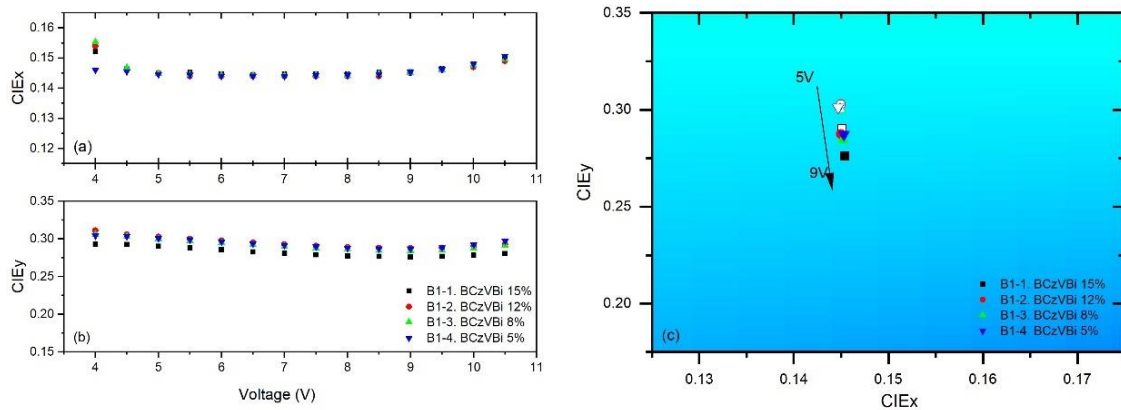


**Figure 5.10:** (a) CIE<sub>x</sub> and (b) CIE<sub>y</sub> color coordinates as a function of bias voltage of devices B1-1 to B1-4.

**Table 5.5:** CIE<sub>xy</sub> color coordinates of device set B1 at 6 V and their changes when the voltage changes from 5 to 9 V and 9 to 10.5 V.

Device	CIE <sub>xy</sub> at 6 V	$\Delta$ CIE <sub>xy,5-9V</sub>	$\Delta$ CIE <sub>xy,9-10.5V</sub>
B1-1	(0.145, 0.285)	(0.000, -0.014)	(0.004, 0.005)
B1-2	(0.144, 0.298)	(0.000, -0.016)	(0.004, 0.006)
B1-3	(0.144, 0.295)	(0.000, -0.016)	(0.005, 0.007)
B1-4	(0.144, 0.297)	(0.000, -0.014)	(0.006, 0.010)

The dominant emission in both the F-P and the P-F EML devices stem from the P-EML, but the relative intensity of fluorescence and phosphorescence varies according to the fluorescent doping concentration. In the two different EML structures, the intensity changes at 448 nm show a different tendency. To be specific, the intensity decreases and is saturated in the F-P EML structure while it increases in the other structure with increasing fluorescent doping concentration. Although the CIE<sub>y</sub> coordinates are greatly dependent on the intensity at 496 nm because of the predominant emission from phosphorescence, the additional fine control in CIE<sub>y</sub> coordinates can be realized by the fluorescence, which is controlled by the fluorescent doping concentration. Therefore, better emission balance between fluorescence and phosphorescence is expected by a fine control of the doping concentration depending on the EML structures.

Figure 5.11 shows the J-V-L characteristics and luminous efficiency of devices A1-4 and B1-4 with 5 % fluorescent doping concentration. Across all these characteristics, device B1-4 with the P-F EML structure shows better performance compared to device A1-4 with the F-P EML structure because hole blocking in the P-F EML structure is more

effective due to the large HOMO energy level difference between BCzVBi and BA1q. In contrast, in the F-P EML structure hole leakage to the cathode occurs due to the low energy difference between the BA1q and the P-EML, resulting in the degradation of device performance compared to the P-F EML structure. Another possible cause for performance degradation in the high current density regime could be the lower triplet energy level of BA1q compared to that of FIrpic. The created triplet excitons cannot be accumulated at the interface. Although the emission from both types of devices predominantly originates from the P-EML, more efficient recombination for emission is generated in the P-F EML structure. Hybrid blue OLEDs show improvement in luminous efficiency compared to 3.3 cd/A (at 172 mA/cm<sup>2</sup>) of blue fluorescent OLEDs with a single EML (DPVBi:BCzVBi (5 %)) reported by Kim et al. [84]. In addition, referring to Figures 5.4 and 5.8 the luminous efficiency of blue OLEDs enhanced by using the F- and P-EML. Also, it was shown that the color coordinates of our devices indicate enhanced blue emission with lower 'y' coordinate values because of fluorescent emission compared to the reported phosphorescent blue OLEDs with FIrpic show CIE<sub>xy</sub> coordinates of (0.17, 0.34) [8], [85].

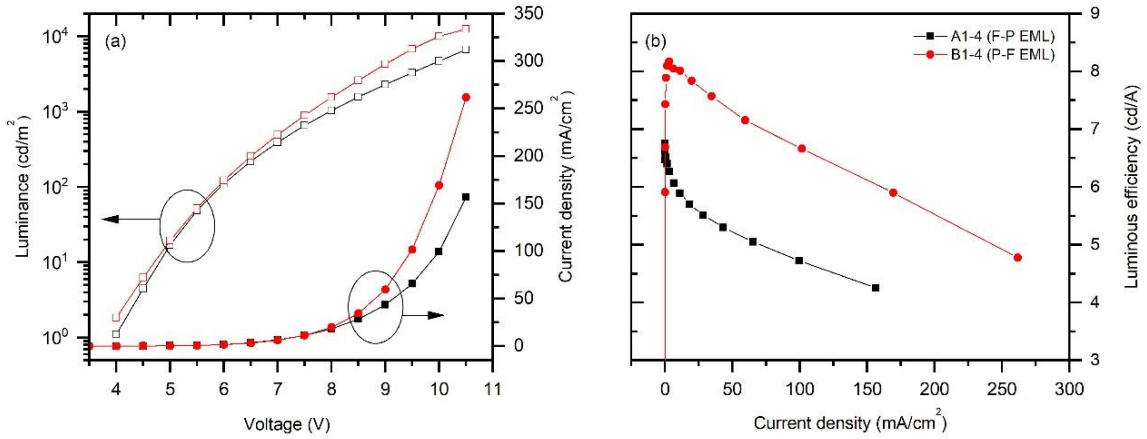


**Figure 5.11:** (a) Current density and luminance of devices A1-4 and B1-4 as a function of the driving voltage and (b) luminous efficiency of devices A1-4 and B1-4 as a function of current density.

### 5.2.3 Effects of Different Electron Transport Layers (ETLs)

To study the effect of different ETLs in blue OLEDs, the electron transport material BAQ is substituted with TPBi without changing any other materials. The device has the P-F EML structure and the phosphorescent and fluorescent doping concentrations are 8 % and 15 %, respectively. Both materials, BAQ and TPBi, have been widely used as an ETL because of their high electron mobility and low-lying HOMO energy levels. TPBi has a relatively deeper HOMO energy level (-6.2 eV) than BAQ (-5.9 eV). By using TPBi, more effective hole confinement at the interface of the EML and ETL can be realized.

**Table 5.6:** EL performance of blue OLEDs with the BA1q and TPBi.

ETL	J (mA/cm <sup>2</sup> )	L ( $\times 10^3$ cd/m <sup>2</sup> )	LE (cd/A)	CIExy
TPBi	57.2	4.12	7.77 (at 10.8 mA/cm <sup>2</sup> )	(0.149, 0.261)
BA1q	20.0	1.59	8.19 (at 11.2 mA/cm <sup>2</sup> )	(0.144, 0.277)

- The device structure is ITO/ NPB (70 nm)/ mCP:FIrpic (15 nm, 8 %)/ DPVBi:BCzVBi (15 nm, 15 %)/ ETL (30 nm)/Liq (2 nm)/ Al.
- The electron transport materials are TPBi and BA1q.
- The current density, luminance and CIExy coordinates are determined at 8 V.

Figure 5.12 displays OLED performance data including J-V-L characteristics, the emission spectra and efficiency of devices with different electron transport materials. The current density and luminance of the device with TPBi are higher because of a favorable electron flow toward the EMLs with the higher electron mobility of TPBi. Although the device with TPBi shows a higher efficiency in a lower current density regime ( $< 5$  mA/cm<sup>2</sup>), the efficiency of devices with TPBi becomes lower than that of BA1q structures with increasing current density. However, in terms of emission color, the fluorescent emission from the device with TPBi was strengthened, which results in a smaller CIExy coordinate and is attributed to hole blocking by TPBi.

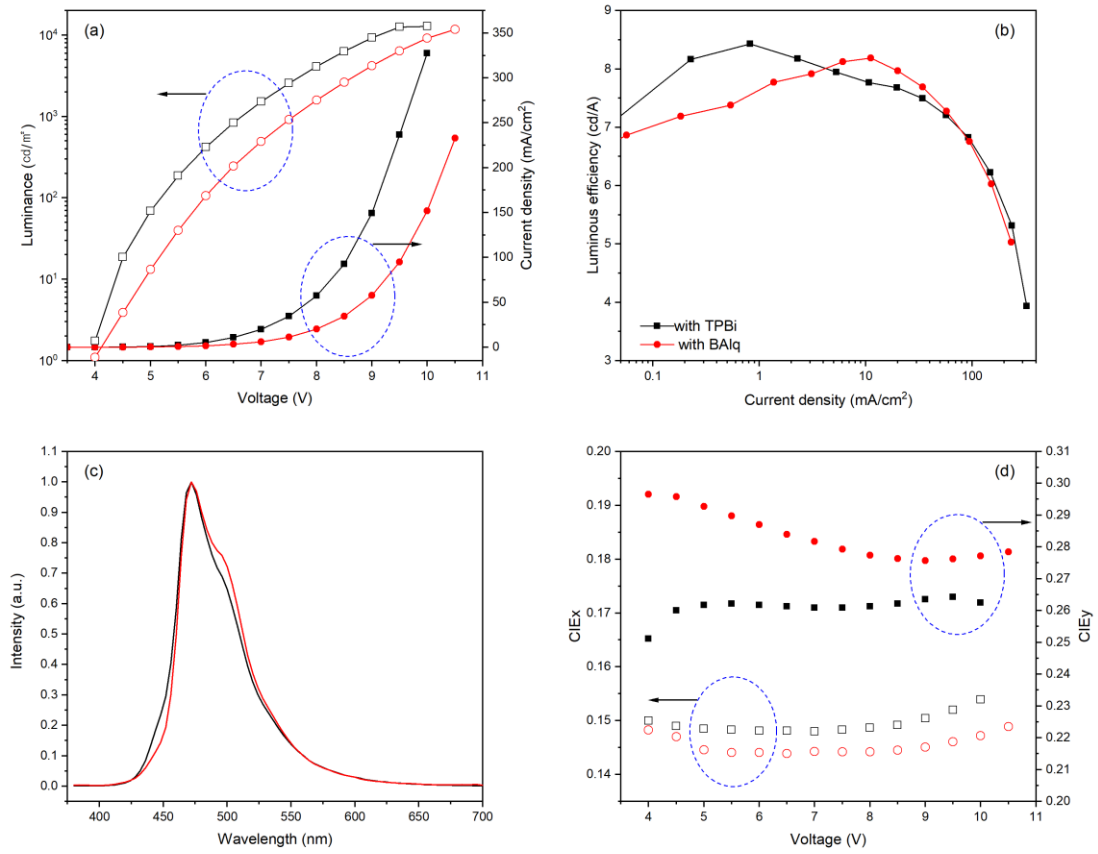


**Figure 5.12:** (a) J-V-L characteristics, (b) luminous efficiency (on a semi-log scale), (c) EL spectra at 6 V and (d) CIE<sub>xy</sub> color coordinates of devices with different electron transport materials, TPBi (black) and BAQ (red).



#### **5.2.4 Brief Summary of Blue OLEDs with Uniformly Doped Double EMLs**

Section 5.2 introduced blue OLEDs containing fluorescent and phosphorescent emitters with controlled doping concentrations and EML structures. Regardless of doping concentration and EML structure, the recombination zone was found to lie at the interface of F- and P-EMLs along with dominant phosphorescent emission; however, the relative contributions of fluorescence and phosphorescence differed depending on doping concentration and EML structure.

Firstly, the fluorescent dopant in the F-P EML structure plays a key role in creating hole transport channels due to the HOMO energy offset between the host and dopant materials. It was shown that the current density is enhanced with increasing doping concentration. The facilitating hole transport affects the location of exciton formation, and consequently the intensity of fluorescence decreases and that of phosphorescence increases with increasing fluorescent doping concentration. On the other hand, when switching the order of the F- and P-EMLs, devices have different heterojunction energy offsets, hence the effect of different doping concentrations on hole transport is not considerable, showing the intensity change with doping concentration is insignificant. When comparing two different EML structures, the P-F EML structure shows the higher device efficiency based on the stronger phosphorescent emission. Lastly, when the electron transport material BA1q is substituted with TPBi in the P-F EML structure, strengthened fluorescent emission was found due to the hole blocking by TPBi.

## 5.3 Step controlled Doped EMLs for Blue OLEDs

### 5.3.1 Device Fabrication: Device Structures and Doping Profiles

For device fabrication, the same preparation and vacuum deposition specifications given in the former section were adopted. The change in device structures is the use of a different ETL, TPBi. The schematic energy level diagrams of the organic layers in the blue OLEDs with TPBi are displayed in Figure 5.13 (a).

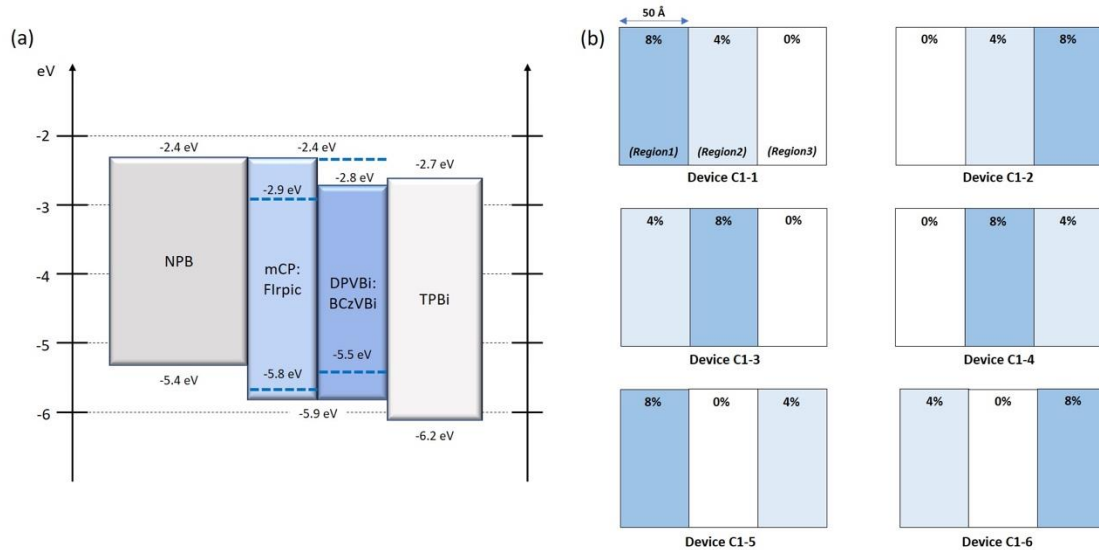


**Figure 5.13:** (a) Energy level diagrams of organic layers in blue OLEDs and (b) doping profiles of the P-EML in devices C1-1 to C1-6.

The devices are once more differentiated by the doping distribution in the emitting region. Compared to other device sets containing uniformly doped emitters over the entire emitting region, here the doping materials are either regularly or irregularly stepwise controlled. Although the total thickness of the EMLs is 30 nm, the phosphorescent dopant is varied at every 5 nm as shown in Figure 5.13 (b). Flrpic doping concentrations in the P-EML were regularly or irregularly stepwise controlled to 0, 4 and 8 % and the BCzVBi doping

concentration was fixed at 15 %. Table 5.7 summarizes the different doping distributions in each device.

**Table 5.7:** The step-controlled doping profiles in each device.

Device	Device C		Note
	P-EML	F-EML	
C1-1	8-4-0 %	15 %	<i>Phosphorescent doping-controlled</i>
C1-2	0-4-8 %		
C1-3	4-8-0 %		
C1-4	0-8-4 %		
C1-5	8-0-4 %		
C1-6	4-0-8 %		

- Thickness of each layer is 15 nm and the step-controlled doping concentration is varied every 5 nm. From the anode side each region having the different doping concentration is labelled as *Region 1- Region 2- Region 3*.

### 5.3.2. Analysis of Electroluminescent Spectra

The EL characteristics of the blue OLEDs with F- and P-EMLs originate from either or both emitters so that it is important to analyze the EL spectra for better understanding of the origin and contribution of each emitter. The EL spectra displayed in Figure 5.14 (a) and (b) were obtained from a BCzVBi-doped (fluorescent) and a FIrpic-doped (phosphorescent) blue OLED, respectively, where the applied voltage was 8 V. The insets in Figure 5.14 are schematic diagrams of the device structure of each device in a cross-sectional view. As shown in Figure 5.14 (a), the emission peaks from the fluorescent blue OLEDs were found at 448 and 472 nm. Along with those peaks, the main peak at 472 nm and shoulder peak at 496 nm were observed from the phosphorescent blue OLEDs. Due to the fact that both emitters have a common emission peak at 472 nm, the peaks at 448 nm and 496 nm provided further information on the emissive contribution of fluorescence and phosphorescence, respectively, from the fabricated OLEDs.

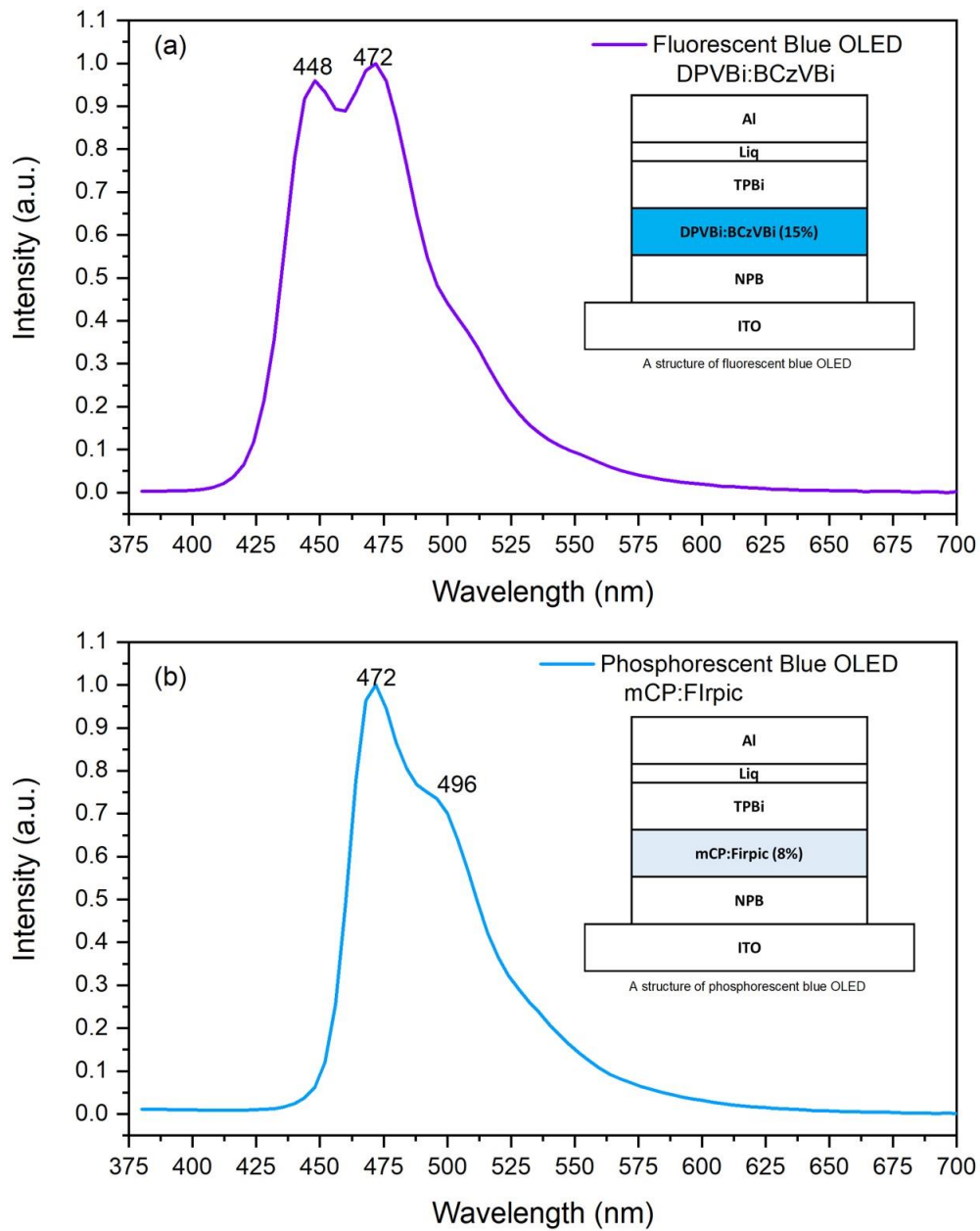


**Figure 5.14:** EL spectra at 8 V from fluorescent (a) and phosphorescent (b) blue OLEDs. The inset are schematic diagrams of device structures of the fluorescent and phosphorescent OLEDs and whose EML compositions are DPVBi doped with BCzVBi (15 %) and mCP doped with Firpic (8 %), respectively. Their common emission peak lies at 472 nm.

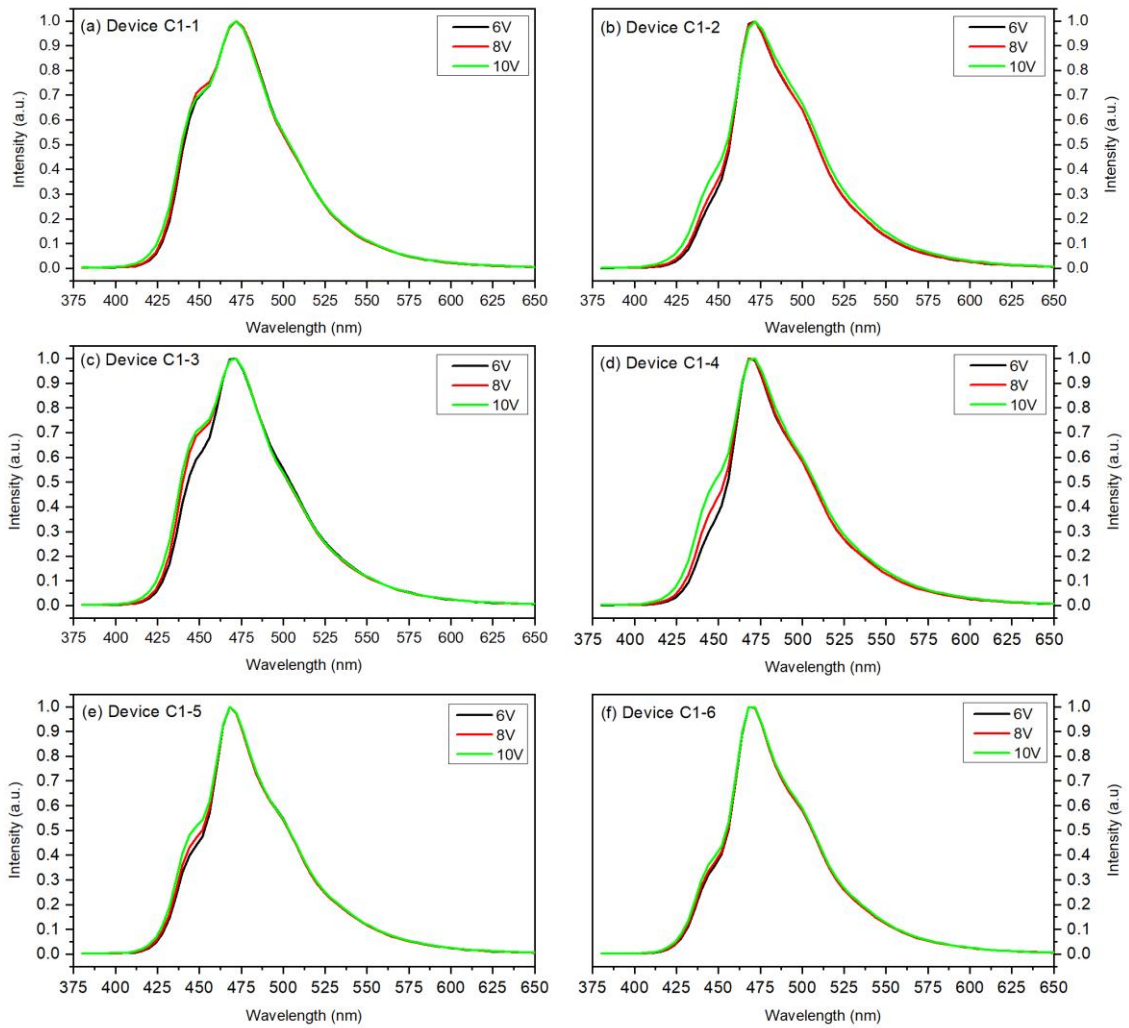


**Figure 5.15:** EL spectra of devices C1-1 to C 1-6 under the different applied voltages.

EL spectra of the given devices under voltages varied from 6 to 10 V are shown in Figure 5.15, and Table 5.8 summarizes the EL intensity at 448 nm and CIE<sub>xy</sub> coordinates at 6 and 10 V. It was observed that all the EL spectra shown in Figure 5.14 have one main peak and two shoulder peaks in common, which originated from fluorescent and phosphorescent emitters, meaning that the recombination zone was formed at the interface of F- and P-EMLs. The exciton formation is extended to *region 2* and slightly moved

toward the cathode side with increasing voltage, which is confirmed by comparing the intensity deduction at 448 nm. As can be seen in Figure 5.15, with increasing voltage, the intensity changes from phosphorescence are not significant; whereas, the intensity variation at 448 nm from the fluorescent emitter was more noticeable, indicating that the emission contribution from the F-EML increased. The fluorescent intensity was also characterized by where the non-doped region was placed and then its variation with increasing voltage was attributed to the spatially controlled phosphorescent doping concentrations.

**Table 5.8:** The EL intensity at 448 nm and CIE<sub>xy</sub> coordinates of each device at 6 and 10 V.

Device	At 6 V		At 10 V	
	EL intensity <sup>a</sup>	CIE <sub>xy</sub>	EL intensity <sup>a</sup>	CIE <sub>xy</sub>
C1-1	0.678 (-29.3 %)	(0.147, 0.186)	0.687 (-28.3 %)	(0.148, 0.182)
C1-2	0.302 (-68.5%)	(0.146, 0.243)	0.395 (-58.8 %)	(0.150, 0.239)
C1-3	0.590 (-38.5%)	(0.148, 0.196)	0.705 (-26.4 %)	(0.150, 0.181)
C1-4	0.347 (-63.8 %)	(0.149, 0.230)	0.505 (-47.3 %)	(0.152, 0.215)
C1-5	0.437 (-54.4 %)	(0.149, 0.208)	0.515 (-46.3 %)	(0.150, 0.199)
C1-6	0.359 (-62.6 %)	(0.147, 0.223)	0.396 (-58.7 %)	(0.149, 0.221)

- The intensity values at the given voltages are taken from the normalized EL spectra, meaning that they are the relative intensities to the ones at 472 nm.
- a. The EL intensity at a given voltage and the intensity deduction at 448 nm ( $(I_{448\text{nm.BCzVBi}} - I_{448\text{nm.Device C1-x}}) / I_{448\text{nm.BCzVBi}}$ ).

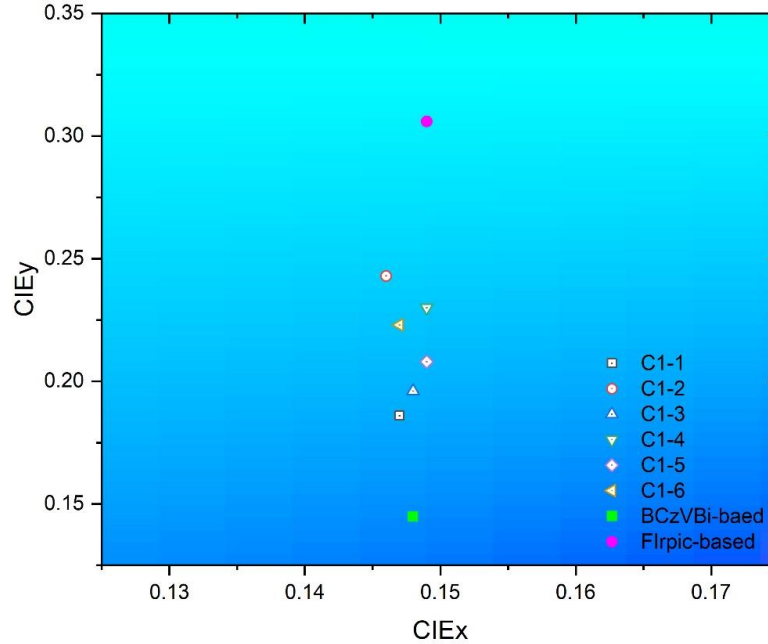


**Figure 5.16:** CIE color coordinates of devices C1-1 to C1-6 and BCzVbi- and Flrpic-doped devices at 6 V. The BCzVbi- and Flrpic-doped device structures are given in Figure 5.13.

The phosphorescent dopant material, Flrpic, is widely known for sky-blue emission. It is found that the cooperation of fluorescent and phosphorescent emitters in one device leads to deeper blue emission compared to the phosphorescent only device, as shown in Figure 5.16. Devices C1-1 and C1-3 have stronger fluorescent emission compared with the other devices, and the corresponding CIE coordinates at 10 V are (0.148, 0.182) and (0.150, 0.181), respectively. The relatively stronger fluorescent intensity was caused by the EML structure where the region without Flrpic was placed in *Region 3*. This non-doped region plays the role of an interlayer; hence the harvest of singlet and triplet excitons is realized through separate channels. Referring to Eq. 2.1 the rate of Förster energy transfer is reduced



by  $(1/R_{HD})^6$  where  $R_{HD}$  is the intermolecular distance between donor and acceptor; therefore, the non-doped region hinders Förster energy transfer of singlet excitons from the F- to the P-EML, which allows singlets to be effectively confined in the F-EML. It also suppresses Dexter energy transfer from triplet states in the P-EML to that in the F-EML, preventing triplet exciton loss through the non-radiative pathway when considering the triplet states of mCP, FIrpic, and BCzVBi are 2.9 [33], 2.62 [7], and 1.81 eV [34], respectively. Furthermore, referring to the CIE<sub>xy</sub> coordinates of uniformly doped blue OLEDs in Figure 5.12 (d), the step-controlled phosphorescent doping profile reduces the CIE<sub>xy</sub> coordinates, meaning that deeper blue emission can be achieved by controlling the phosphorescent contribution in the corresponding recombination zone.

Considering that, based on the location of the emission peaks, the EL spectra of devices originated from both the fluorescent and phosphorescent emitters, we have plotted EL spectra with a linear combination of the emission contributions of F- and P-EMLs. A cumulative spectrum in the form of a linear combination can be given as

$$C_F I_F + C_P I_P = I_{CS} \quad \text{Eq. 5.1}$$

where  $C$  is a fraction of fluorescence and phosphorescence intensity and the sum of  $C_F$  and  $C_P$  is 1.  $I$  is the EL intensity and  $F$ ,  $P$  and  $CS$  denote fluorescence, phosphorescence and cumulative spectrum. Device C1-1 shows a spectral emission ratio between fluorescence and phosphorescence ( $C_F:C_P$ ) of 70:30 while the ratio is 29:71 in the case of device C1-2, which indicates that phosphorescence is dominant. Figure 5.17 displays EL spectra of devices C1-1 and C1-2 at 8 V together with the cumulative spectra based on the ratio of linear combination. The small differences between the full and the cumulative spectra may

come from the possible intensity variations at the secondary peaks of BCzVbi and FIrpic. Table 5.9 summarizes the fractions of fluorescence and phosphorescence from devices C1-1 to C1-4.

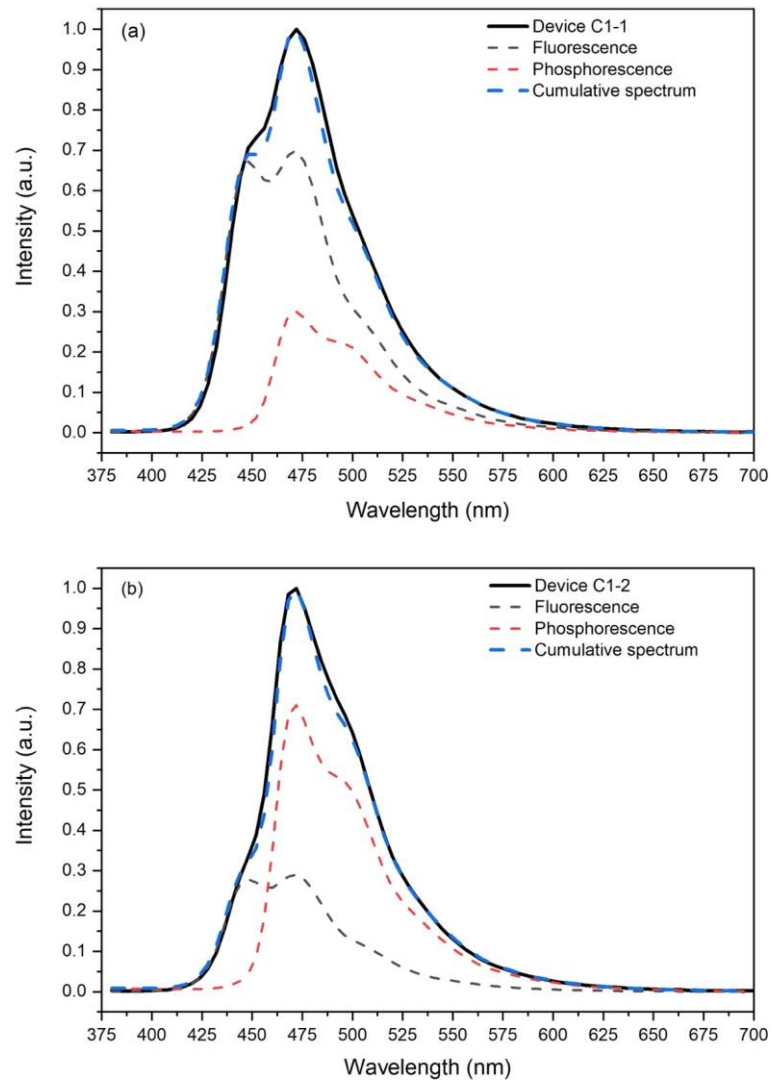


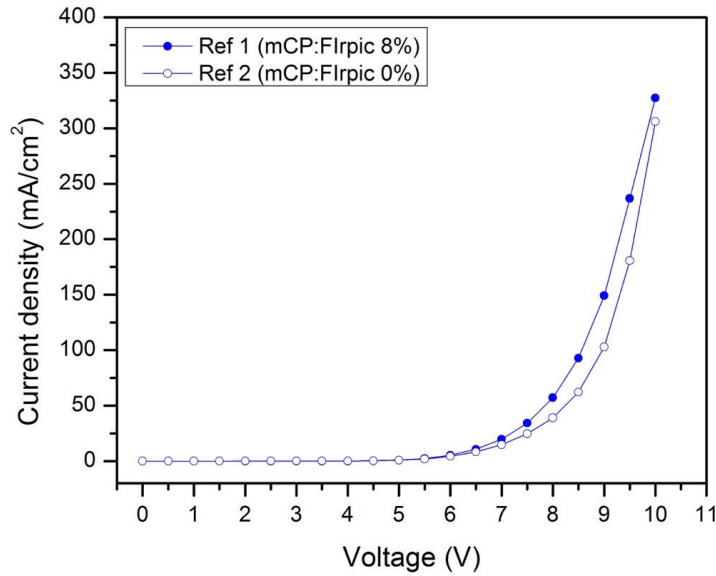
**Figure 5.17:** EL spectra of devices (a) C1-1 and (b) C1-2 at 8 V. The blue dashed lines are cumulative spectra of fluorescent and phosphorescent reference devices.

**Table 5.9:** Fraction of fluorescence ( $C_F$ ) and phosphorescence ( $C_P$ ) of devices C1-1 to C1-4 at 8 V.

Device	C1-1	C1-2	C1-3	C1-4
Fluorescence ( $C_F$ %)	70	29	68	39
Phosphorescence ( $C_P$ %)	30	71	32	61

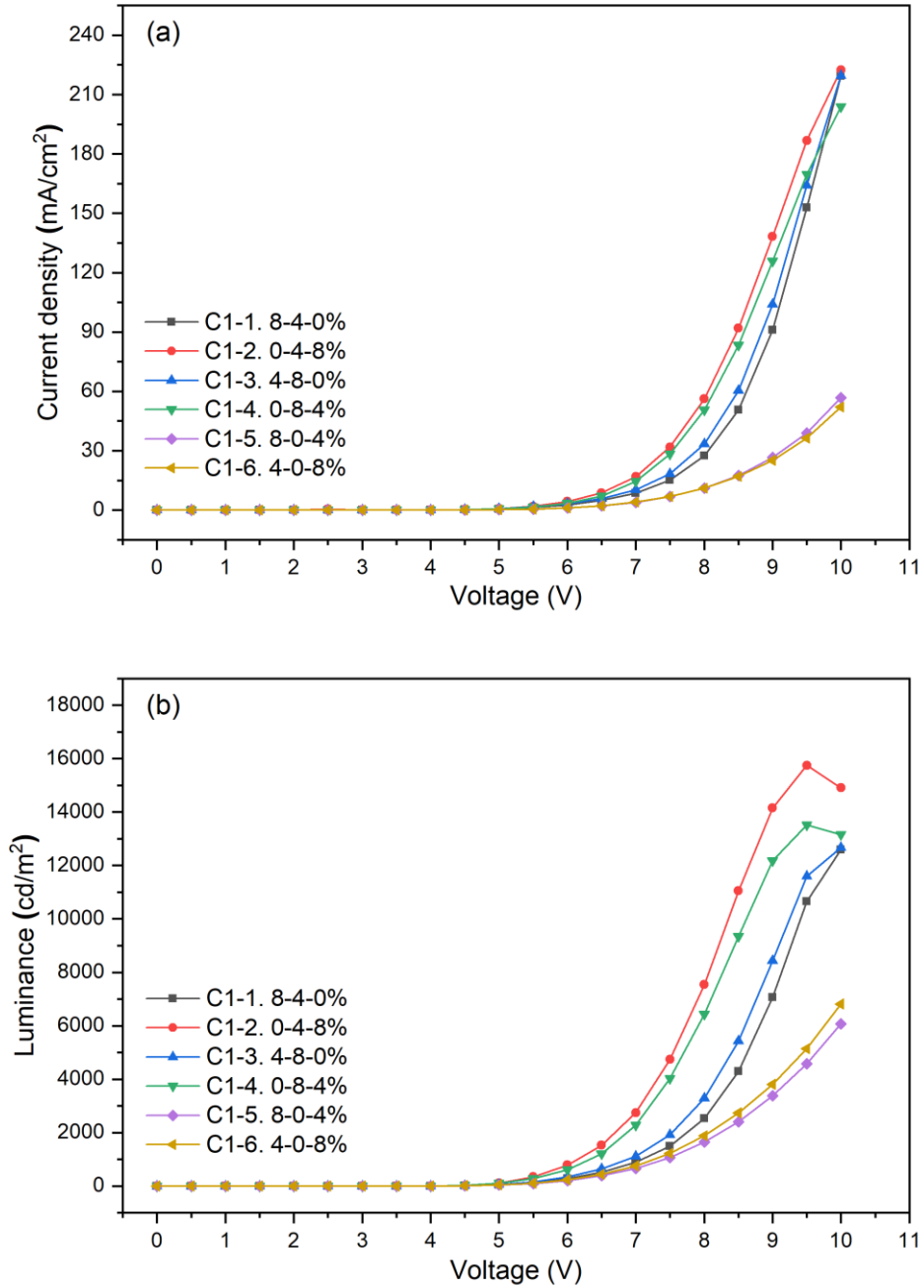
### 5.3.3 Electrical and Optical Properties

Figure 5.18 shows the current density of reference samples 1 and 2 whose P-EML is uniformly doped with 0 % and 8 %, respectively. The existence of the dopant molecules in the host material increased current density. When the FIrpic molecules are introduced, they act as transport routes for electrons with direct injection because of the 0.1 eV LUMO level difference between DPVBi and FIrpic. The more FIrpic – which is known as an electron type material [86] – is inserted, the shorter the distance becomes between molecules and more possible transport channels are introduced; therefore, current density increased with increasing doping concentration.



**Figure 5.18:** Current density as a function of applied voltage from reference samples 1 and 2 (the reference devices have the same device structure: ITO/ NPB/ mCP:Flrpic (0 % or 8 %)/ DPVBi:BCzVBi/ TPBi/ Liq/ Al).

The plots of current density and luminance as a function of applied voltage are displayed in Figure 5.19. It was found that the current density of the fabricated blue OLEDs was firstly determined by the location of the non-doped region in the P-EML. As is shown in Figure 5.19 (a), devices C1-2 and C1-4 that have the non-doped region in *Region 1*, exhibit higher current density than any other devices. In the case of holes, HOMO levels of mCP and Flrpic have only 0.1 eV difference so that the movement of holes is more likely to be affected by mCP, which is a carbazole-based material with high hole mobility [86]. From this aspect, the insertion of the non-doped region on the HTL side resulted in a widening of the hole transport region.



**Figure 5.19:** (a) Current density and (b) luminance versus the applied voltage of devices C1-1 to C1-6.

The average and standard deviations of current density, luminance and interpolated values of turn-on and operating voltages of devices C1-1 to C1-6 are summarized in Table 5.10. The results were obtained from 5 measurements. Turn-on and operating voltages are defined with luminance of 1 cd/m<sup>2</sup> and 1000 cd/m<sup>2</sup>, respectively. As indicated in Table 5.10, the turn-on voltage where devices start emitting was the highest when the non-doped region was in *Region 3* and it decreased as the region moved toward the anode side. In addition, devices C1-5 and C1-6 showed lower current density and higher operating voltages compared to other devices due to the trap effect by the dopants at the interface.

**Table 5.10 <sup>a</sup>:** Average and standard deviations in device performance including current density, turn-on and operating voltages and luminance.

Device	J <sup>b</sup> (mA/cm <sup>2</sup> )	L <sup>b</sup> (cd/m <sup>2</sup> )	Turn-on voltages <sup>c</sup> (V)	Operating voltages <sup>c</sup> (V)
C1-1	27.4 (± 2.3)	2551 (± 189.2)	4.08 (± 0.02)	7.10 (± 0.05)
C1-2	58.6 (± 6.3)	7385 (± 385.8)	3.81 (± 0.07)	6.19 (± 0.07)
C1-3	32.3 (± 2.5)	3244 (± 233.0)	4.03 (± 0.04)	6.88 (± 0.06)
C1-4	50.8 (± 1.7)	6532 (± 228.6)	3.78 (± 0.03)	6.32 (± 0.05)
C1-5	10.9 (± 1.0)	1650 (± 122.3)	3.99 (± 0.03)	7.41 (± 0.09)
C1-6	11.7 (± 1.3)	1930 (± 140.1)	3.92 (± 0.05)	7.24 (± 0.08)

- The given values are the average and standard deviation characterized by 5 measurements.
- The values of current density and luminance at 8 V.
- The turn-on and operating voltages are found by interpolation. Turn-on and operating voltages are defined as the voltage where the luminance is 1 cd/m<sup>2</sup> and 1000 cd/m<sup>2</sup>, respectively.

**Table 5.11:** Summary of luminous efficiency and roll-off in luminous efficiency for devices C1-1 to C1-6.

Device	Maximum LE (cd/A)	LE <sup>a</sup> (cd/A)		Roll-off <sup>b</sup> (%)	LE <sup>c</sup> (cd/A)
C1-1	10.7	10.3	8.04	21.9	8.53 ( $\pm 0.1$ )
C1-2	18.4	18.1	14.2	21.5	13.0 ( $\pm 0.9$ )
C1-3	11.1	11.0	8.82	19.8	9.42 ( $\pm 0.2$ )
C1-4	18.5	17.5	13.0	25.7	12.9 ( $\pm 0.3$ )
C1-5	19.3	15.9	10.8	32.1	11.4 ( $\pm 0.2$ )
C1-6	21.6	18.5	13.6	26.5	12.9 ( $\pm 0.3$ )

a. LE ( $\eta$ ) at 1000 and 6000 cd/m<sup>2</sup>.

b. LE roll-off was calculated by  $(\eta_{1000cd/m^2} - \eta_{6000cd/m^2})/\eta_{1000cd/m^2}$ .

c. LE ( $\eta$ ) at 50 mA/cm<sup>2</sup> are averaged over 5 measurements.

The maximum luminous efficiency, luminous efficiency at particular luminance (1,000 and 6,000 cd/m<sup>2</sup>) and efficiency roll-off are summarized in Table 5.11. In addition, the values of luminous efficiency at 50 mA/cm<sup>2</sup> are shown in Table 5.11 as averages and standard deviations. The luminance differed in accordance with the location of the non-doped region in the P-EML, similar to the current density. As mentioned earlier, the recombination zone was found at the interface of the F- and P-EMLs, and hence the FIrpic doping concentration adjacent to the F-EML affected the luminance along with the effect of the non-doped region. To be specific, when comparing devices with matching non-doped layer locations, a higher luminance was observed when the 8% doping area was located closer to the F-EML. As a result, devices C1-2 and C1-6 have higher luminance than

devices C1-4 and C1-5, respectively. The higher concentration of the FIrpic dopant as highly emissive sites explains the higher luminance.

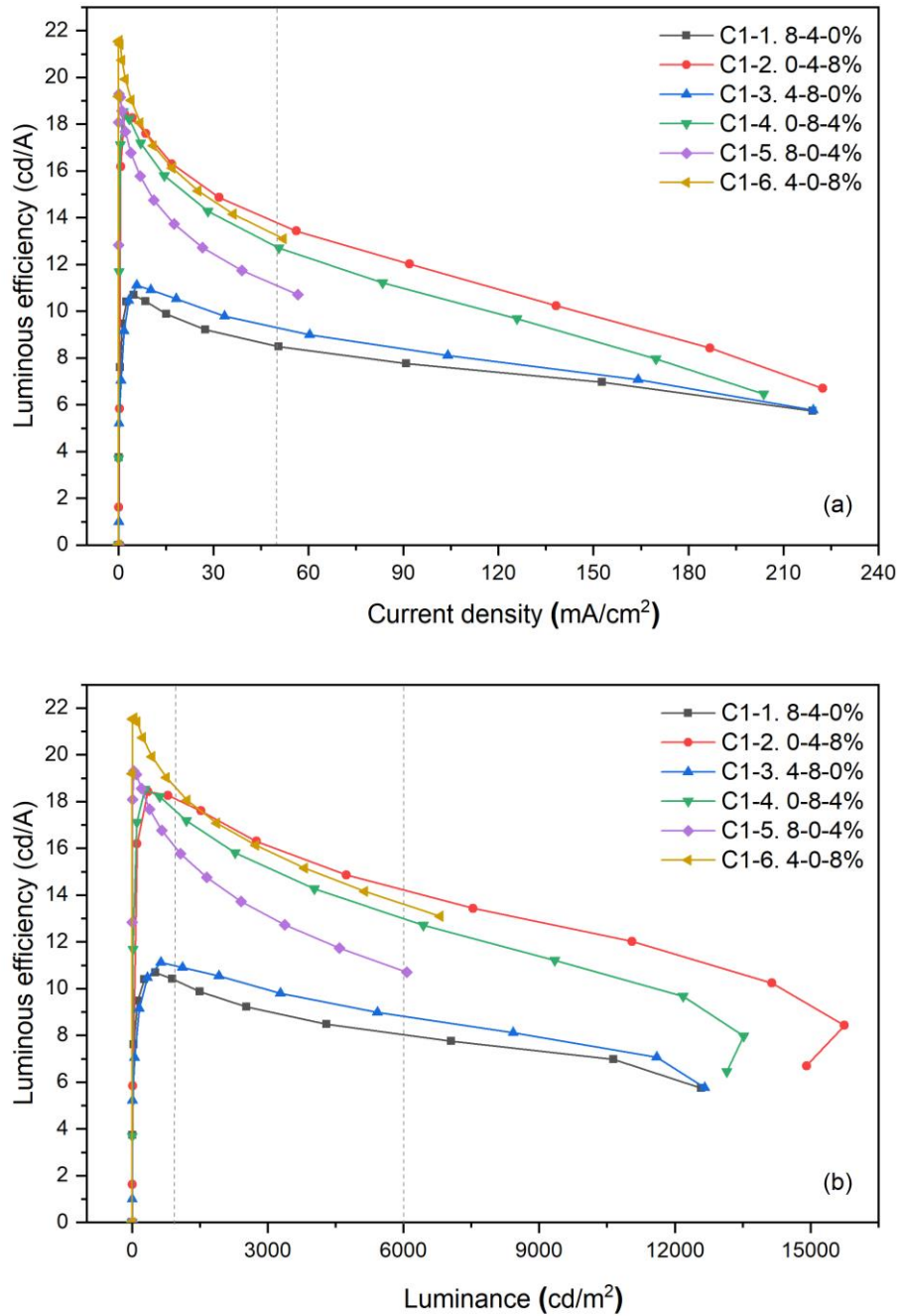


**Figure 5.20:** Luminous efficiency as a function of (a) current density and (b) luminance (The dotted vertical lines indicate 50 mA/cm<sup>2</sup>, 1,000 and 6,000 cd/m<sup>2</sup>).



Figure 5.20 (a) and (b) show the luminous efficiency with increasing current density and luminance, respectively, in devices C1-1 to C1-6. When the carriers are directly injected and form excitons within the FIrpic, the higher FIrpic doping concentration in the emitting region means there are more possible emissive spots in devices. The triplet energy level of mCP is higher than that of FIrpic so the undesired back-energy transfer from FIrpic to mCP would be suppressed and triplet excitons can be confined at the dopant molecules. The maximum luminous efficiency was found from device C1-6; however, with increasing current density, device C1-6 shows drastic roll-off in luminous efficiency. At current densities higher than  $10 \text{ mA/cm}^2$ , device C1-2 has a higher luminous efficiency than any other device. Firstly, the location of the non-doped region changed the trends of luminous efficiency with increasing current density. Among three doping tiers in the P-EML the doping concentration in *Regions 2* and *3* also affected the device efficiency because the formation of a recombination zone occurred at the interface of the F- and P-EMLs and expanded to *Regions 2* and *3* in the P-EML. That is why higher efficiencies were found in devices C1-2 and C1-6, where *Region 3* was doped with the higher phosphorescent doping concentration at 8 %.

Previous work by Yoo et al. reported that the efficiency roll-off from a phosphorescent blue OLED consisting of FIrpic (8 %) doped into mCP was 20 % when current density increased from 30 to  $60 \text{ mA/cm}^2$  [87]. In the case of the devices in this work, the efficiency roll-off of devices C1-1 to C1-4 in the same current density range is 9.0, 11, 9.6, 13 %, respectively, which indicates reduced efficiency roll-off when both fluorescent and phosphorescent emitters are involved in the emission. From the aspect of

efficiency roll-off in terms of luminance, devices C1-5 and C1-6 showed a larger efficiency roll-off than any other device, particularly, the largest roll-off in luminous efficiency was observed from device C1-5 with the value of 32.1 %. This significant efficiency roll-off is a result of the narrow recombination zone limited to *Region 3* in the P-EML, leading to a high triplet exciton accumulation. The movement of the recombination zone with the applied voltage is verified again with the tendency of the efficiency roll-off among devices. Hence, broadening the recombination region is one of the ideas to reduce the density of triplet excitons at high current densities, leading to less efficiency roll-off by bimolecular annihilations. In the case of devices C1-1 and C1-3, their luminous efficiency was lower than any other devices while the efficiency roll-off of device C1-3 was the lowest at 19.8 %. This can be explained by the predominant contribution to luminance from the F-EML by singlet excitons. Because of the theoretically limited IQE of singlet excitons, devices C1-1 and C1-3 showed lower luminous efficiency compared to any other device; however, the undesirable exciton loss was effectively blocked by the mCP region and the loss by annihilations was reduced by singlet excitons with shorter lifetime.

### **5.3.4 Brief Summary of Blue OLEDs with Step-controlled Doping Profiles**

In Section 5.3, dual-EML blue OLEDs with regularly or irregularly step-controlled phosphorescent doping concentrations are introduced. It is worth noting that the determination of the fluorescent intensities at 448 nm and their variation as a function of voltage can be explained by different spatial FIrpic concentrations, bringing about different carrier distributions in the P-EML and varied phosphorescence contribution. Moreover, the width of the recombination zone could be changed in devices with the different doping profiles, which was connected to device efficiency roll-off by means of bimolecular annihilation. The doping conditions next to the F-EML and the position of the non-doped region have great impact on the electrical and optical properties. Among the six devices in this study, device C1-2, with a regularly stepwise phosphorescent doping concentration, showed the best performance in terms of current density and luminance despite showing a relatively stronger phosphorescent intensity. Although device C1-3 had the second lowest luminous efficiency over the entire driving current density, the lowest efficiency roll-off, 19.8 % was observed and its EML structure is beneficial for obtaining strong fluorescence. It was found that there was a trade-off between efficiency and color due to the properties of the fluorescent and phosphorescent emitters and more research to achieve a better balance of the two emitters will be required.

## **Chapter 6.**

# **Various Host Combinations in Triple Emitting Layers for Blue OLEDs**

The study for this chapter is based on blue OLEDs with triple EMLs which were composed of various host material combinations without changing the blue dopant materials and their concentrations. We will discuss the blue OLEDs' electrical and optical performance depending on the triple EMLs' configurations by the different host combinations, the change of layer thickness and the use of interlayers.

The research work in this chapter has been published in the paper entitled "Hybrid Blue Organic Light Emitting Diodes with Fluorescent and Phosphorescent Emitters along with an Interlayer," *Science of Advanced Materials*, Volume 8, Number 2, 2016, pp. 301-306.

[DOI: <https://doi.org/10.1166/sam.2016.2483>]

## 6.1 Introduction

Light generation in OLEDs occurs by electron and hole recombination; therefore, an additional structural design to confine excitons within EMLs should be considered to further improve efficiency. In general, the diffusion length of triplet excitons can be as long as 100 nm, which is much longer than the typical 10 nm of singlet excitons. Also, their excited state lifetime is of the order of  $\sim \mu\text{s}$ , which is sufficient to diffuse to adjacent layers [51], [88], [89], and therefore the employment of charge blocking materials with a high triplet energy level is important for confining triplet excitons inside the recombination zone. In the case of a hybrid EML structure, which is made up of both fluorescent and phosphorescent EMLs, inserting an interlayer between fluorescent and phosphorescent EMLs can block undesirable energy transfer to adjacent layers, causing non-radiative decay.

When multiple EMLs are applied to OLEDs, controlling the location of the recombination zone is crucial to achieve a desirable color emission and to improve efficiency [68], [90]–[92]. The location of the recombination zone in OLEDs can be tuned by the variation in layer thickness and doping concentration [93] as well as the control in charge transport properties of host materials [94]. When any host material has a certain polarity in charge transport, the exciton formation is narrow and created at the interface between the EML and the other side of charge transport layer [94].

In this chapter, blue OLEDs with triple EMLs consisting of fluorescent and phosphorescent emitters are introduced. Their device architectures are differentiated by various combinations of host materials, the use of interlayers, and the thickness of each EML to understand how different device structures affect electrical and optical properties

of devices. The investigation concentrates particularly on the color quality and efficiency of blue OLEDs.

## 6.2 Device Fabrication: Device Structures and Doping Profiles

Unlike the previous chapter, the blue OLED devices have triple EMLs and each device has a different EML configuration by varying the host material combinations. The standard device structure of blue OLEDs introduced in this chapter is as follows: *ITO / NPB (70 nm)/ triple EMLs (30 nm without interlayers and 33 nm with interlayers)/ TPBi (30 nm)/ Liq (2 nm)/ Al (100 nm)*. For the P-EMLs, mCP (p-type), and TPBi (n-type) are used as host materials and doped with FIrpic (8 %). The host material for the F-EML is DPVBi and doped with BCzVBi (15 %). The triple EMLs are composed of two P- and one F-EMLs and specifically, the F-EML is sandwiched by the two P-EMLs. The sum of thickness of two P-EMLs and the thickness of the F-EML is kept at 15 nm. The interlayer is mCP and is 1.5 nm thick each. The details of the triple EML configurations and their corresponding host combinations are listed in Table 6.1.

**Table 6.1:** List of triple EML structures.

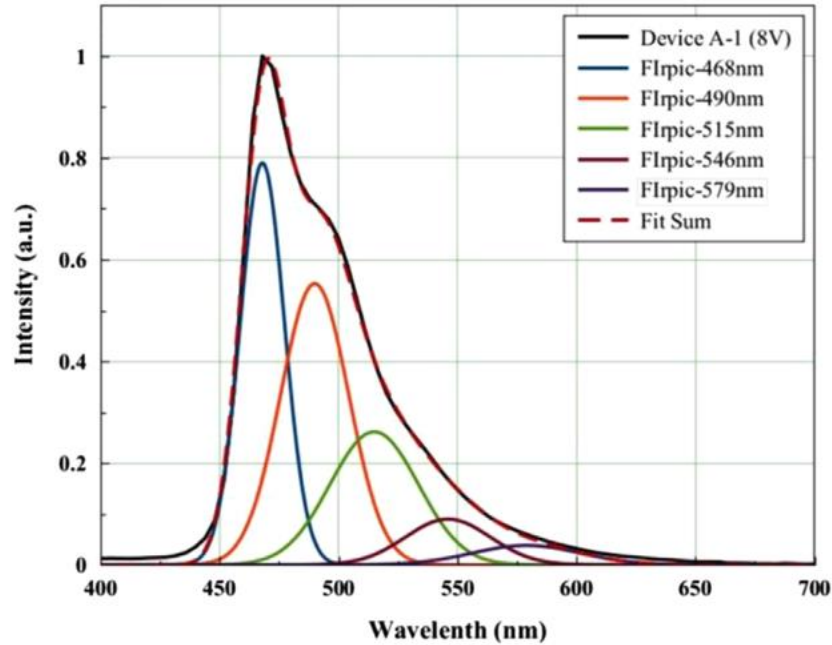
Device	Triple EML Structure	Host Material Combination
E1-1	mCP:FIrpic (8 %)/ mCP/ DPVBi:BCzVBi (15 %)/ mCP/ TPBi:FIrpic (8 %)	p-F-n
E1-2	mCP:FIrpic (8 %)/ mCP/ DPVBi:BCzVBi (15 %)/ mCP/ mCP:FIrpic (8 %)	p-F-p
E1-3	TPBi:FIrpic (8 %)/ mCP/ DPVBi:BCzVBi (15 %)/ mCP/ mCP:FIrpic (8 %)	n-F-p
E1-4	TPBi:FIrpic (8 %)/ mCP/ DPVBi:BCzVBi (15 %)/ mCP/ TPBi:FIrpic (8 %)	n-F-n

- ‘p’ and ‘n’ represent the phosphorescent EML with p (hole transport)-type and n (electron transport)-type host materials, respectively and ‘F’ indicates the fluorescent EML.
- The thickness of each P-EML is 7.5 nm and that of the F-EML is 15 nm.

### 6.3. Characterization of Devices with Various Host Combinations

#### 6.3.1 Deconvoluted EL Spectra for Understanding the Origin of Emission

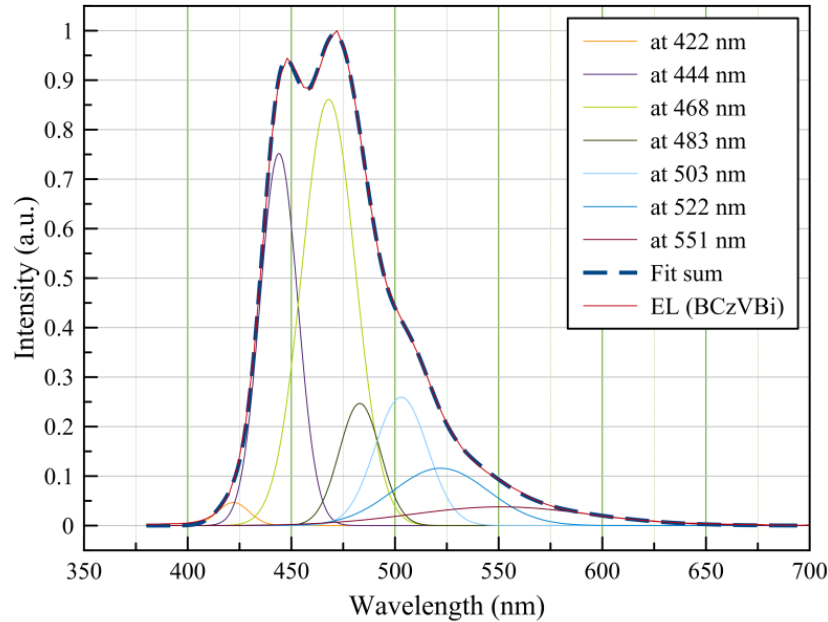
Luminescence is attributed to electronic transitions and each luminescent material shows different characteristics. Each electronic state has a series of vibrational states and the typical spacing of vibrational energies is on the order of 0.1 eV [95]. To investigate the origin of blue emission in devices, deconvolution of the EL spectra by Gaussian peak fitting was carried out. The previous work by Yoo et al. reported that the deconvoluted peaks from the FIrpic-doped devices were observed at 468, 490, 515, 546 and 579 nm, as given in Figure 6.1 [87].



**Figure 6.1:** The deconvoluted EL spectrum by Gaussian peak fitting of (a) a FIrpic-doped OLED with the structure: ITO/ NPB (70 nm)/ mCP:FIrpic (30 nm, 8 %)/ TPBi (30 nm)/ Liq (2 nm)/ Al. (Reprinted with permission from [87]).

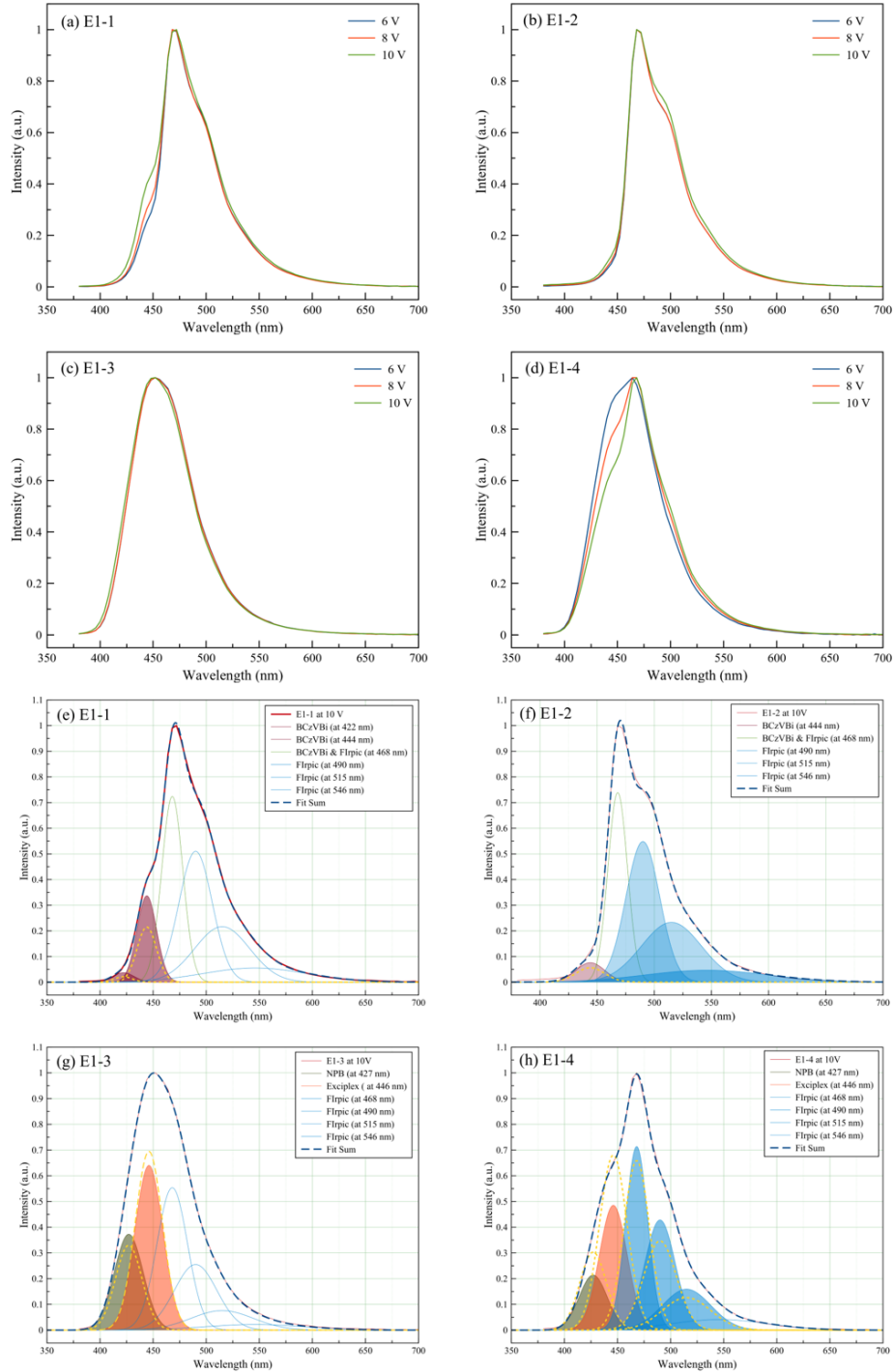
On the other hand, as seen in Figure 6.2 the Gaussian peaks at 422, 444, 468, 483, 503, 522 and 551 nm correspond to the BCzVBi-doped devices. A common Gaussian peak was found at 468 nm from the given deconvoluted EL spectra and hence, other peaks are meaningful to analyze the origin of blue emission and recombination zones of devices. The first Gaussian peak originates from the electronic transition from the lowest singlet state to the ground state ( $S_{10} \rightarrow S_{00}$ ) of BCzVBi, which was found at the wavelength where the absorption and PL spectra intersected as shown in Figure 4.2. The subsequent two peaks are related to Förster energy transfer between host and dopant materials [43], [84].





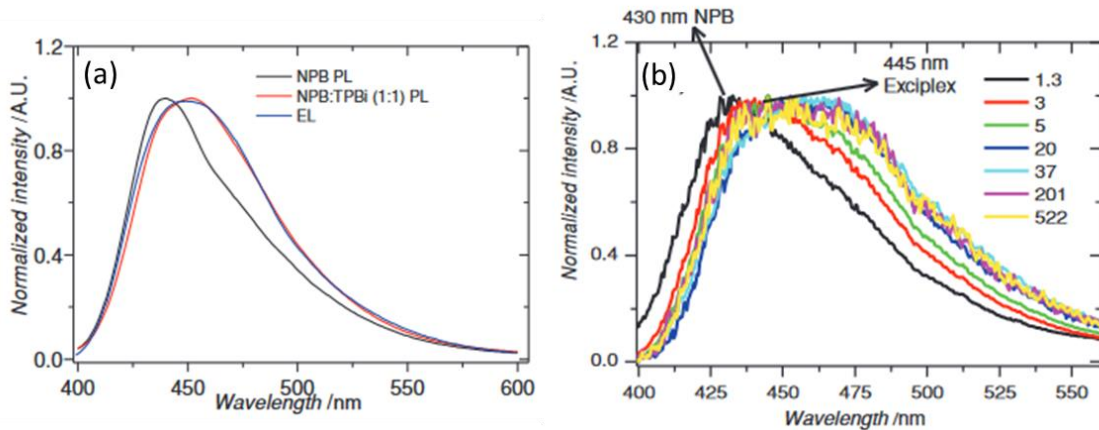
**Figure 6.2:** The deconvoluted EL spectrum by Gaussian peak fitting of a BCzVBi-doped OLED with the structure: ITO/ NPB (70 nm)/ DPVBi:BCzVBi (30 nm, 15%)/ TPBi (30 nm)/ Liq (2 nm)/ Al.

Figure 6.3 shows the EL spectra of devices E at 6, 8 and 10 V and their deconvoluted EL spectra by Gaussian peak fitting. The Gaussian peaks were plotted for each device at 6 V with dotted lines and at 10 V with solid lines. The blue emission of device E1-1 originates from both F- and P-EMLs as seen from the Gaussian peaks at 422 and 444 nm from BCzVBi and the rest from FIrpic. Figure 6.3 (a) shows that the intensity of fluorescence at 444 nm increases because exciton formation more favorably happens at the F-EML when the applied voltage increases. In the case of device E1-2, mainly phosphorescent emission is generated and there is no significant change with increasing voltage as shown in Figure 6.4 (b). mCP and DPVBi are hole transport-type host materials, and consequently the exciton formation is more likely to occur at the n-type P-EML.



**Figure 6.3:** (a)-(d) EL spectra of devices E1-1 to E1-4 at 6, 8 and 10 V, respectively and (e)-(h) Gaussian peak fitting of each device at 10 V. The dotted lines in the Gaussian peak fitting indicate the Gaussian peaks at 6 V.

Unlike the first two devices, devices E1-3 and E1-4, however, exhibit Gaussian peaks at 427 and 446 nm which cannot explain the origin of emission based on the indicated peaks from Flrpic (phosphorescence) and BCzVBi (fluorescence)-doped devices. This is because the electron and hole recombination in these devices tends to occur at the interface of the HTL and EML by exciplex due to the high energy offset. Jankus et al. reported that a device with an NPB:TPBi (1:1) film showed the exciplex emission at 445 nm which is a red-shifted NPB emission from 430 nm as shown in Figure 6.4 [96].



**Figure 6.4:** (a) PL spectra of NPB and NPB:TPBi (1:1) films and EL spectrum of the device whose structure is ITO /NPB (30 nm) /NPB:TPBi (35 nm)/ TPBi (35 nm)/LiF (1 nm)/Al(100 nm). (b) Time-resolved spectra from NPB:TPBi (1:1) film excited with 355 nm pulsed laser and recorded with gated intensified charged coupled device (iCCD) camera. Indicated numbers are camera opening times after excitation in nanoseconds (delay time), the integration times are  $\sim 1/10$ th of the delay time. Adapted with permission from [96].

The EL results of devices E1-3 and E1-4 elucidate the fact that there is no fluorescent emission achieved from BCzVBi when the n-type host material is located at the HTL side due to carrier distribution. In device E1-4 the intensity of the peaks at 427 and 446 nm

decreases and that from the phosphorescence slightly increases when the applied voltage increases, due to the fact that the recombination zone moves to the P-EML of the HTL side. Figure 6.5 provides the EL spectra comparison of device E1-4 and 2 references which consist of only the P-EMLs. Ref 2 with the n-type host material placed at the HTL showed emission in the shorter wavelength region (colored region in Figure 6.5), and hence the emission is affected by the F-EML.

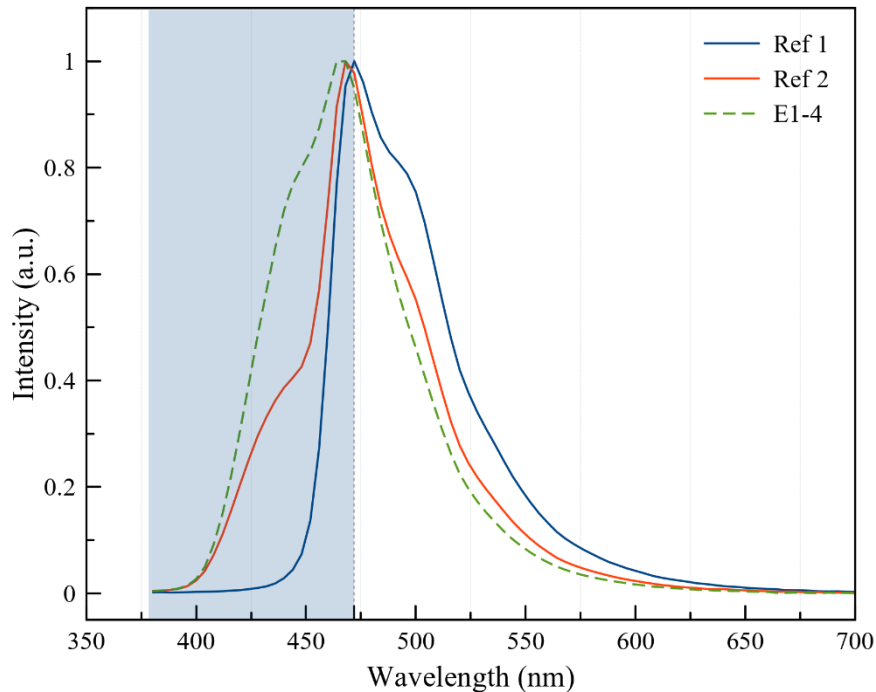


**Figure 6.5:** Comparison of EL spectra between the phosphorescent emitter only devices and E1-4. The EML structure of Ref. 1 is mCP:FIrpic (8 %)/ CBP:FIrpic (8 %)/ TPBi:FIrpic (8 %) while that of Ref. 2 is TPBi:FIrpic (8 %)/ CBP:FIrpic (8 %)/ mCP:FIrpic (8 %).

CIE<sub>xy</sub> color coordinates as a function of voltage for devices E1-1 to E1-4 and their changes from 5 to 10 V are shown in Figure 6.6. The CIE y-coordinates varied depending

on the EML configurations. The CIE<sub>xy</sub> coordinate variations when the voltage increases from 5 V to 10 V is relatively large in devices E1-1 and E1-4, which are (0.002, -0.017) and (-0.004, 0.032), respectively. When only p- or n-type phosphorescent host material is used, carriers are prone to dominantly move to the one side so that there is no significant color variation with voltage. Device E1-3 shows the best performance possessing the lowest y-coordinate, (0.150, 0.110) at 6 V and is the most stable as a blue emitting device in the range of driving voltages. Device E1-4 still accomplishes the standard value for blue emission even though there is a large variation in its y coordinate with increasing the contribution of phosphorescent emission.

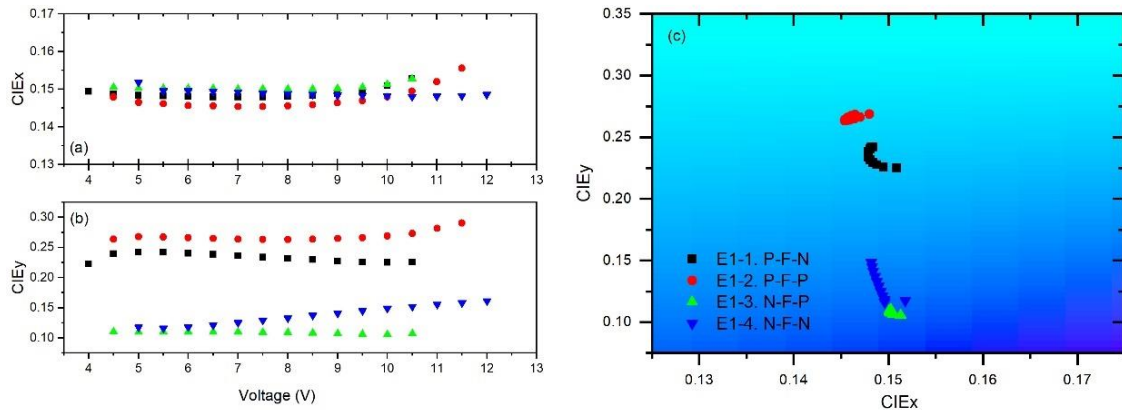


**Figure 6.6:** (a) CIE<sub>x</sub> and (b) CIE<sub>y</sub> color coordinates as a function of bias voltage and (c) CIE<sub>xy</sub> changes from 5 V to 10 V of devices E1-1 to E1-4.

### 6.3.2 Electrical and Optical Properties

The current density as a function of voltage is displayed in Figure 6.7 and it is shown that the characteristics of current density in devices E1-1 to E1-4 are greatly affected by which type of host material was placed beside the charge transport layers. Although dopant sites can become additional transport channels for charge carriers in doped OLEDs, the carrier transport in organic layers is mainly determined by the properties of host materials because all devices have the same phosphorescent doping concentration. The n-type host material is the same one for the ETL, indicating that there is no energy barrier between two layers; therefore, electron transport toward the EMLs is more facilitated by the structure. Based on this aspect, the current density of devices E1-1 and E1-3 is higher than that of the other two devices. Contrary to the previous case, placing the p-type host material next to the ETL is energetically unfavorable for charge transport. In particular, the lowest current density of device E1-4 stems from the unfavorable host material combination with adjacent charge transport materials. The electrical and optical properties of devices E1-1 to E1-4 are summarized in Table 6.2.

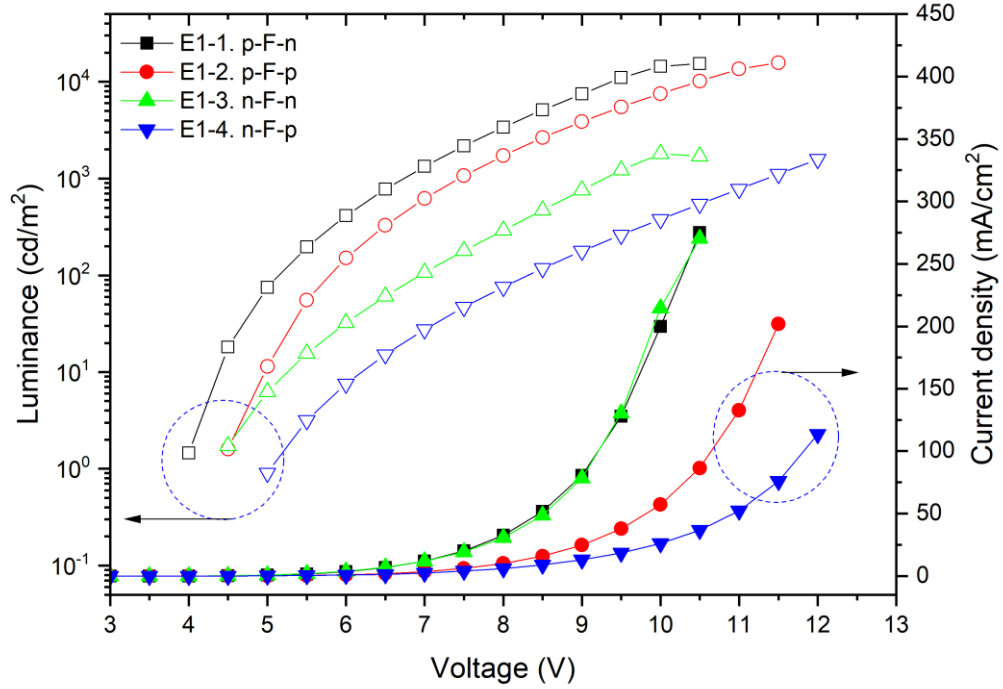


**Figure 6.7:** Current density and luminance as a function of voltage from devices E1-1 to E1-4.

**Table 6.2:** J-V-L characteristics and device efficiency of devices E1-1 to E1-4.

Device	J (mA/cm <sup>2</sup> ) <sup>a</sup>	L (×10 <sup>3</sup> cd/m <sup>2</sup> ) <sup>b</sup>	LE max (cd/A)	LE (cd/A) <sup>c</sup>
E1-1	200	14.5	11.8	9.26
E1-2	57.2	7.54	17.6	11.8
E1-3	214	1.80	0.97	0.97
E1-4	26.1	0.38	1.48	1.46

a. Current density at 10 V.

b. Luminance at 10 V.

c. Luminous efficiency of devices A to D at 80.6, 86.5, 78.4 and 75.9 mA/cm<sup>2</sup>, respectively.

Figure 6.7 shows the luminance with increasing voltage and indicates that the tendency of luminance between devices is different compared to that of current density. Although device E1-3 has the highest current density (together with device E1-1), its luminance is much lower than device E1-1. This is because the hole transport toward the EML side is hindered by the large HOMO energy barrier between the HTL and EML in device E1-3, resulting in a carrier imbalance in the EML region. Also, it should be considered that the absence of effective electron blocking toward the anode side can cause a current leakage. Figure 6.8 shows the luminous efficiency versus current density of devices E1-1 to E1-4. Device E1-2 with the p-F-p combination has the highest luminous efficiency based on the predominant phosphorescent emission but a significant efficiency roll-off with increasing current density is found. Bimolecular annihilation such as triplet-triplet or triplet-polaron annihilation is an inevitable phenomenon due to a high local density of excitons in phosphorescent OLEDs [97]–[99]. In this respect, the efficiency roll-off of device E1-2 is the largest because of the dominant phosphorescent emission, resulting in bimolecular annihilation with increasing current density. However, the roll-off is alleviated by the contribution of the fluorescent emission compared to that of reference 1 as shown in Figure 6.8. Device E1-1 shows the second highest luminous efficiency among the four devices but the roll-off of its efficiency is lower than of device E1-2. The difference in luminous efficiency between devices E1-1 and E1-2 decreases with increasing current density because the strengthened exciton formation in the fluorescent EML in device E1-2 reduces the density of triplet excitons in the EML preventing triplet-triplet or triplet-polaron annihilation. The trade-off between efficiency and efficiency roll-off by the



incorporation of the fluorescence is unavoidable; however, controlling the contribution of fluorescence and phosphorescence with voltage can be helpful to balance between the efficiency and its roll-off.

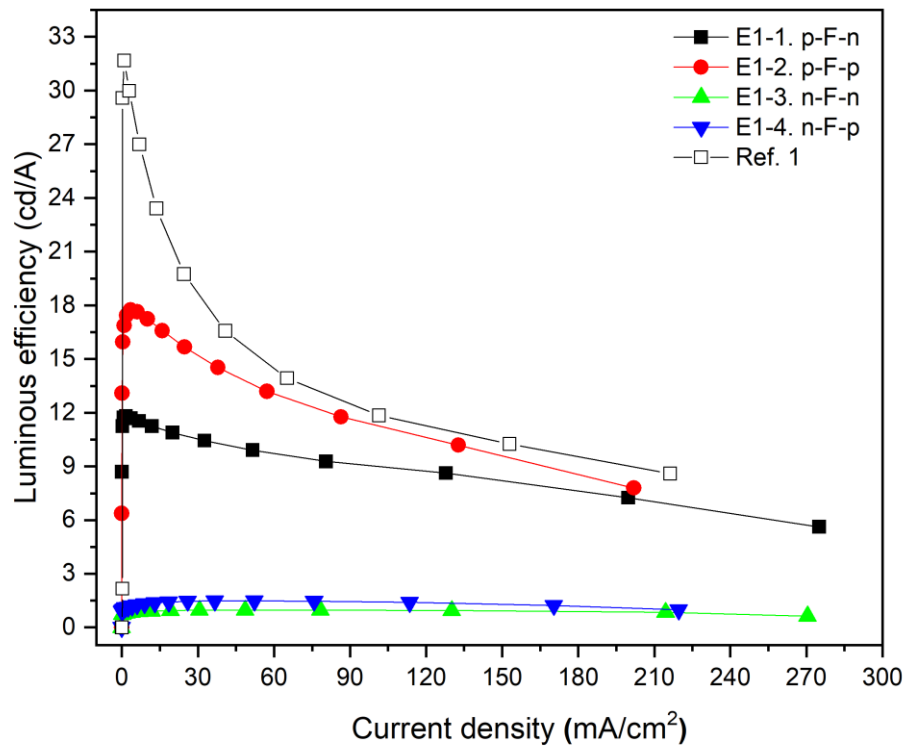


**Figure 6.8:** Luminous efficiency of devices E1-1 to 1-4 and Ref. 1. The EML structure of Ref. 1 is given in Figure 6.5.

### 6.3.3 Effects of Different EML Thicknesses in the p-F-n EML Structure

To study the effects of different EML thickness the F- and P-EML thicknesses of device E1-1 were changed from 15 nm and 7.5 nm, respectively to 10 nm each. The total EML thickness is kept constant. When each EML has the same thickness of 10 nm, the total thickness ratio of F- and P-EMLs becomes 1:2. Figure 6.9 shows the device performances of the two devices. The luminous efficiency at 20 mA/cm<sup>2</sup> of the two devices is 14.9 and 10.9 cd/A and 1.3 times improved when the total P-EML thickness increases. The difference of CIE y-coordinates between two devices increases at a higher voltage due to the further increase in the fluorescent intensity from device E1-1.

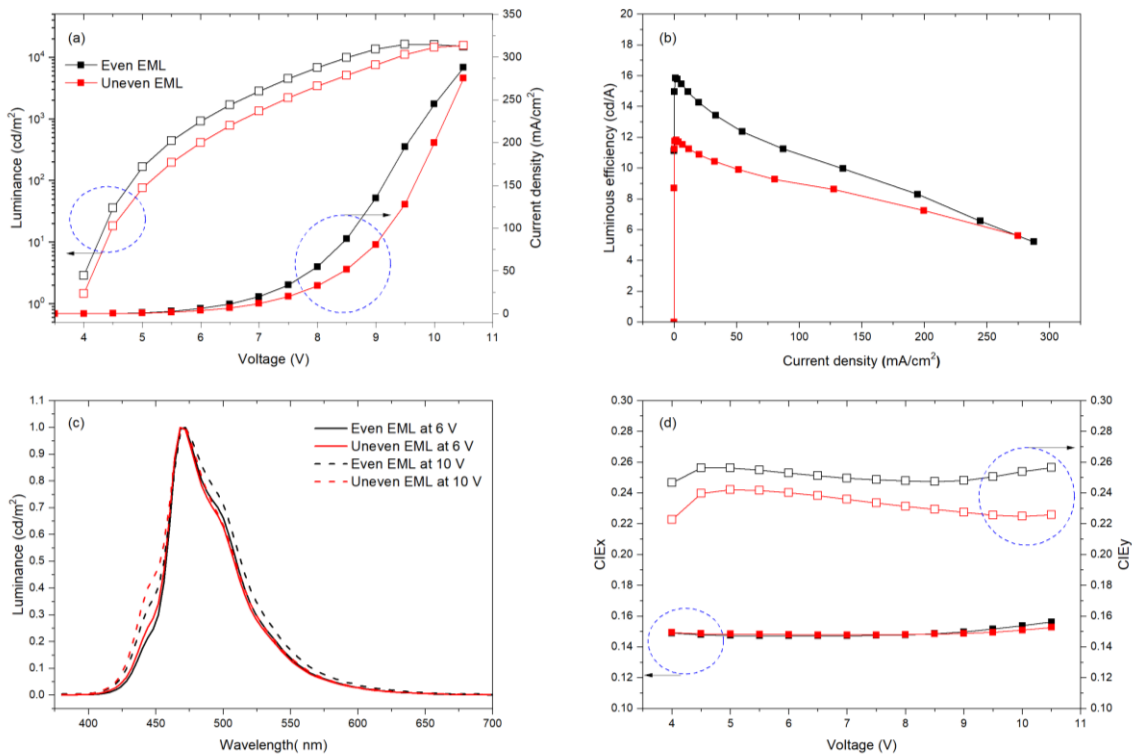


**Figure 6.9:** (a) J-V-L characteristics, (b) luminous efficiency (c) EL spectra at 6 and 10 V and (d) CIE<sub>xy</sub> coordinates as a function of voltage of devices with even EML thickness (black) and E1-1 (red).

### 6.3.4 Effects of mCP Interlayers in the p-F-n EML Structure

The utilization of an appropriate interlayer between the P- and F-EMLs is important to optimize exciton harvesting by preventing triplet exciton quenching toward neighboring layers with a lower triplet energy state. The triplet energy state of the blue fluorescent emitter is 1.81 eV [34] which is lower than that of FIrpic [7]. As mentioned earlier, in these devices mCP was chosen as an interlayer whose triplet energy state is 2.9 eV [33]. The device structure without the interlayer is the same as device E1-1 except for the absence of the interlayer, mCP, between EMLs. As shown in Figure 6.10, the use of the interlayer improves device efficiency to about 1.4 times higher at 20 mA/cm<sup>2</sup> in the p-F-n structure. To optimize the device performance, the use of interlayer is indispensable to block undesirable triplet exciton quenching by Dexter energy transfer, particularly if the triplet energy state of the blue fluorescent emitting materials is lower than that of neighboring phosphorescent emitting materials. In terms of emission color, the fluorescent intensity of device E1-1 is lower than that of the device without the interlayer, implying that the interlayer is not thick enough to prevent Förster energy transfer from the F- to P-EMLs. To prohibit the Förster energy transfer between two EMLs, the interlayer thickness needs to be larger than the Förster radius (~3 nm) [100]. Referring to the step-controlled blue OLEDs in Section 5.3, devices showed enhanced fluorescent intensity when the non-doped area (5 nm) acting as an interlayer was placed at the right next to the P-EML, resulting from the separate emission channels at each EML. Further research on the effect of interlayer thickness would be required to optimize device performances.

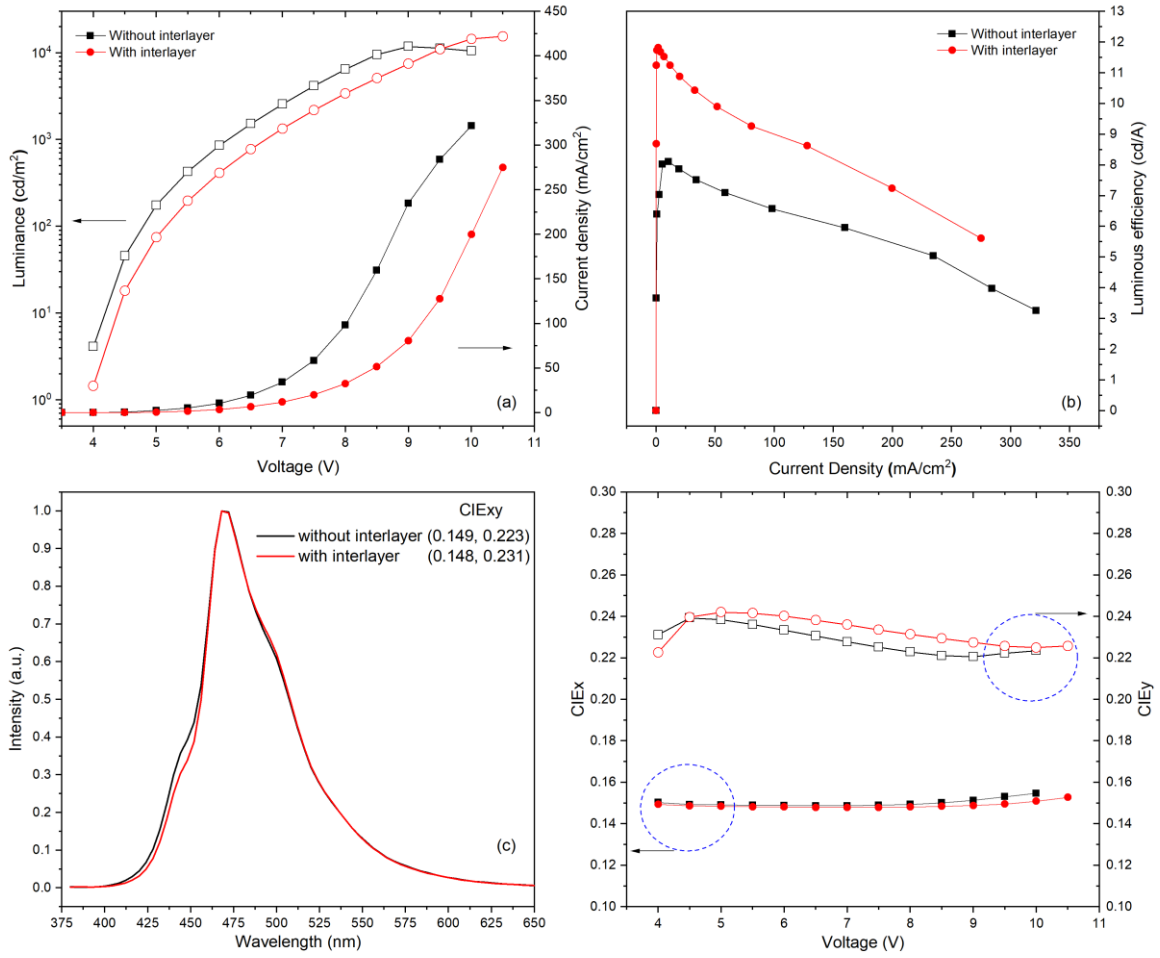


**Figure 6.10:** (a) J-V-L characteristics, (b) luminous efficiency and (c) EL spectra at 8 V and (d) CIExy coordinates of devices E1-1 with (red) or without (black) the interlayer, mCP.

## 6.4 Summary

A new architecture of triple-EML blue OLEDs with fluorescent and phosphorescent emitters was introduced. For the study of structural effects on device performance, the EML configurations are differentiated by various combinations of the host materials. The origin of the emission was studied based on Gaussian peak fitting and the fluorescence from device E1-1 with a p-F-n EML structure was strengthened with increasing voltage due to the host material combination to facilitate carrier transport toward the F-EML. When the n-type host material was placed at the HTL side, the exciton formation was generated at the HTL side because of the unfavorable hole transport at the large energy barrier. Therefore, the emission occurred at the interface between the HTL and the n-type EML. In the case of device E1-2, the strongest phosphorescent emission was found, which undergoes significant efficiency roll-off due to triplet-triplet or triplet-polaron annihilations. When the total P-EML thickness became larger, the efficiency increased 1.3 times. It was shown that the utilization of the interlayer caused the efficiency improvement by preventing triplet exciton quenching toward the neighboring materials with the lower triplet energy state; however, there was no enhancement in the color emission because it is not sufficient to avoid Förster energy transfer between the F- and P-EMLs.

# **Chapter 7.**

## **Conclusions and Suggestions for Future Study**

### **7.1 Conclusions**

This thesis is mainly focused on blue OLEDs whose architectural key feature is the use of both fluorescent and phosphorescent emitters in a device. The device structures of blue OLEDs were engineered not simply by varying layer composition but also by tailoring the doping concentration to study device operation and electrical and optical performance. The important findings derived from the experiments and analysis presented in the thesis can be summarized as follows:

In Chapter 5, blue OLEDs with double EMLs were introduced and their EML structure designs were varied by controlling doping concentrations and by switching the order of the F- and P-EML. Although the relative emission contribution from F- and P-EMLs varied depending on doping concentration and EML structure, it was seen that the dominant emission originated from the P-EML. The fluorescent dopants in the F-P EML structured devices played a distinct role as additional transport channels and hence devices

showed a strengthened phosphorescent emission with increasing fluorescent doping concentration. On the other hand, the transport effect of the fluorescent dopant in the P-F EML structure became insignificant and the change in the fluorescent intensity with doping concentration was negligible. However, when compared to the other EML structures, the devices with the P-F EMLs had higher device efficiency based on the stronger phosphorescent emission. If the ETL is replaced with TPBi in the P-F EML structure, the fluorescent emission intensity increased due to the hole blocking by TPBi.

When the phosphorescent doping concentration of the blue OLEDs is regularly or irregularly controlled by 0, 4 and 8 %, the phosphorescent doping concentration at the interface of F- and P-EMLs and the placement of the non-doped (0 %) area in the P-EML determine the electrical and optical performance of the devices. The fluorescent emission and their variation as a function of voltage can be described by different spatial distributions of the phosphorescent dopant and particularly, when the non-doped area is next to the F-EML, this acts as an interlayer, resulting in stronger fluorescent emission.

In Chapter 6, triple-EML blue OLEDs were proposed and the effect of different host material combinations, layer thicknesses and interlayers in the triple-EML blue OLEDs were investigated. The location of the n-type phosphorescent host affects device performance in current density and recombination zones. Moreover, the utilization of the interlayer prevents triplet exciton quenching to the neighboring materials with the lower triplet energy state. Deconvoluted EL spectra based on Gaussian fitting were used to understand the origin of the fluorescent and phosphorescent emission.

## **7.2 Suggestions for Future Study**

The incorporation of both fluorescent and phosphorescent emitters in EMLs is one of the common design concepts for white OLEDs, called hybrid white OLEDs; however, most research work for blue OLEDs used only either of the two emitters rather than both in a single device. This thesis presented blue OLEDs with fluorescent and phosphorescent emitters and showed their performance changes with different doping profiles and EML compositions. Although this research work suggested and showed blue OLEDs with fluorescent and phosphorescent emitters, there is still room to improve device performance with respect to color purity (and stability with voltage) and device efficiency and to study in-depth the mechanisms of device operation and degradation. Some suggestions to expand the presented research work are given below.

### **7.2.1 Device Characterization Relative to the Presented Research**

This research work had sought to determine the respective emissive contribution from F-and P-EMLs by deconvoluting EL spectra of devices as well as by comparing the EL intensity at certain wavelengths. Therefore, complementary studies such as time-resolved luminescent spectroscopy measurements can be undertaken for in-depth understanding of the dynamics of singlet and triplet excitons and ultimately of the efficiency roll-off caused by bimolecular or exciton-polaron interactions.

In addition, the precise probing of the recombination zone in the EMLs would be beneficial for a better understanding on the origin of emission within two EMLs and for realizing the control in the emission zone. The profiling of the recombination zone can be



carried out by inserting a sensing layer [60], [101]. The position of the sensing layer is changed within the EML and the position-dependent EL intensity of the sensing material is monitored to study the recombination zone in each device [52], [60], [101]–[104]. It is necessary that the sensing layer itself should not affect any charge transport characteristics of the devices.

### **7.2.2 Material Selection**

The optimal material selection is important to enhance device efficiency and quality of emission color. Blue emitters are categorized into three types: fluorescent, phosphorescent and delayed fluorescent emitters [105]. From the efficiency point of view, the theoretical maximum IQE of the fluorescent emitters is limited to 25 % based on spin statistics. The fluorescent dopant in this thesis has a low triplet energy level and so the observed losses were unavoidable due to the fact that triplet excitons in conventional fluorescent emitters are “lost” to fluorescence by a non-radiative transition. Even though this effect was moderated by using an interlayer, using different types of blue fluorescent emitters that prevent these losses can be more effective because of the elimination of an additional step for interlayer deposition. Blue delayed fluorescent emitters, achieving emission from the singlet excited state by an up-conversion (TADF) or a down-conversion (triplet-triplet fusion, TTF) leading to a reverse intersystem crossing [106] can be candidates to resolve this problem. Because triplet excitons in these two cases are still involved for emission, the theoretical IQE in the TTF-based device is 62.5 % and that in the TADF-based device is 100 %. The most common TTF blue fluorescent emitters are

anthracene- and pyrene-based materials [106]. It has been shown that the EQE from the TTF-based device reached 14.8 %, which is superior to that (~5 %) of common blue fluorescent emitters [106], [107].

Furthermore, the thesis showed that the non-doped mCP layer played a role as an interlayer by blocking an undesirable energy transfer between the fluorescent and phosphorescent EMLs, resulting in the increase in device efficiency. The result of Chapter 6 indicated that the different types of host materials influence the carrier transport characteristics. Based on these results, further investigations by fine controlling the layer thickness and/or by replacing different charge transport type materials can be conducted to optimize the device performance.

From the color point of view, the emission spectrum of FIrpic shows the maximum peak at 472 nm and extends from 450 nm to over 600 nm owing to vibrational levels [108], implying that it is detrimental to deep blue emission. Other available blue phosphorescent emitters with a blue-shifted emission compared to FIrpic, are FIr6, Iridium (III) bis(4,6-difluorophenylpyridinato)(5-(pyridine-2-yl)-1,2,4-triazolate) (FIRTaz), Iridium (III) bis(4,6-difluorophenylpyridinato)(5-(pyridine-2-yl)-tetrazolate) (FIRN4), and tris((3,5-difluoro-4-cyanophenyl)-pyridine) iridium (FCNIr) whose emission peaks are placed at 458 [109], 460 [110], 459 [111] and 448 nm [112], respectively. The CIE coordinates of FIr6 and FCNIr are (0.16, 0.26) [85] and (0.15, 0.19) [111], respectively, which shows a potential improvement for blue emission.

### 7.2.3 The Adoption for White OLEDs

White OLEDs have had a lot of attention as a promising candidate for environmentally friendly and energy-saving lighting [113]–[122]. Color temperature tunable white OLEDs have been demonstrated [123]–[125], which is desirable for sunlight-style illumination by comparison with the conventional lighting sources, such as incandescent bulbs and fluorescent tubes with a fixed color temperature [123], [126]. The correlated color temperature (CCT) is strongly connected to the relative intensity of blue emission in the white spectrum [127] and has physiological and psychological impacts on human beings [125]. High CCT light stimulates the cortisol secretion, which makes people awake and active [128]–[130]; therefore, it allows people to be more focused and productive at work [128], [129] and is beneficial during working hours. However, high CCT light inhibits melatonin secretion [131]–[133], which disrupts the human circadian clock and increases the growth of cancer cells [131]. Photochemical damage to the retina can also be caused by deep blue emission.

For white OLEDs, there are two different ways to generate white emission, which are using two complementary or three primary color mixtures. For either way, blue is an indispensable component. In the case of the two-color approach using yellow phosphorescent emitters, blue emitters possessing CIE coordinates ( $x < 0.2$ ,  $y < 0.2$ ) are required to achieve a reasonable white emission [134]. As was shown in Chapters 4 and 5, from the color aspects, the CIE results of blue OLEDs seem to be far from the NTSC standard of deep blue emission for display applications, which is (0.14, 0.08), mainly because of the predominant emission from the P-EML.

The research work on blue OLEDs with both fluorescent and phosphorescent emitters in this thesis can be extended as a new approach towards white emission. Because the CCT of white OLEDs can be controlled by the relative contribution of blue emission to the white emission, the variation in emission peaks as well as EL intensity along with the movement in recombination zones between blue F- and P-EMLs may bring out a different insight into controlling the CCT of white OLEDs. The spectral results of blue OLEDs in the thesis showed the change in the fluorescent and/or phosphorescent intensities when the voltage is changed. It has been reported that the insertion of charge modulation layers leads to a fine control the location of the recombination zone with applied voltage by managing the flows of electrons and holes in the EMLs [59], [113], [135], [136]. Jou et al. reported, as is shown in Figure 7.1, CCT tunable white OLEDs with a combination of double sky-blue (FIrpic) and one orange EMLs along with 1,3,5-tri(m-pyrid-3-yl-phenyl)benzene (TmPyPB) as the charge modulation layer [125], [137].

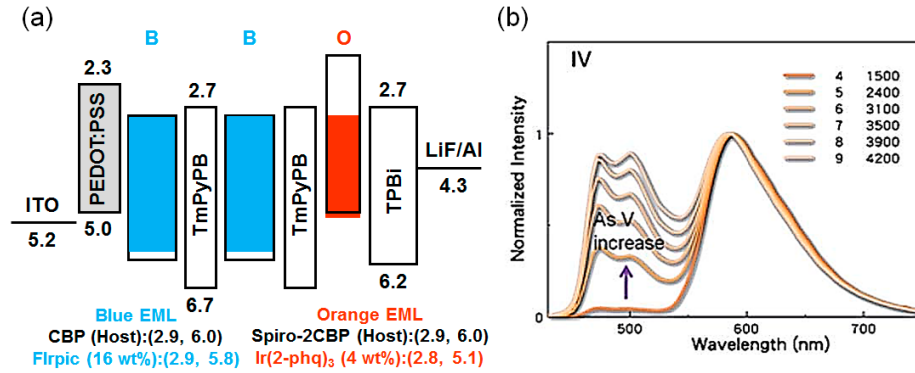


**Figure 7.1:** (a) Schematic energy level diagram of CCT tunable white OLED by Jou's group and (b) EL spectra of the given device from 4 V to 9 V on 1 V interval (The CCT changed from 1,500 K to 4,200 K). Reprinted with permission from [125].

Xia et al. in 2016 reported tunable white OLEDs with two different blue emitters, N,N'-(4,4'-(1E,1'E)-2,2'-(1,4-phenylene) bis(ethene-2,1-diyl)bis(4,1-phenylene))-bis(2-ethyl-6-methyl-N-phenylaniline) (BUBD-1) and BCzVBi [138]. The white OLED with BUBD-1 (device A) showed a 3,000-10,000 K CCT range and CRI 75-78 while that with BCzVBi (device B) showed a wider CCT variation of 2,500-15,000 K and a higher CRI of 94-97 when the applied voltage is 4-10 V, which indicates that a deep blue emitter enables one to realize high color rendering index (CRI) and broader color temperature variation for white OLEDs [138]. Although further material and thickness optimization will be required, incorporating fluorescent and phosphorescent blue emitters could open another channel to realize CCT tunable white OLEDs.

# References

- [1] M. Pope, H. P. Kallmann, and P. Magnante, “Electroluminescence in organic crystals,” *J. Chem. Phys.*, vol. 38, no. 8, pp. 2042–2043, 1963.
- [2] C. W. . W. Tang and S. A. Vanslyke, “Organic electroluminescent diodes,” *Appl. Phys. Lett.*, vol. 51, no. 12, pp. 913–915, 1987.
- [3] J. H. Burroughes, D. D. C. Bradley, A. R. Brown, R. N. Marks, K. Mackay, R. H. Friend, P. L. Burns, and A. B. Holmes, “Light-emitting diodes based on conjugated polymers,” *Nature*, vol. 347, pp. 539–541, 1990.
- [4] M. A. Baldo, D. F. O’Brien, Y. You, A. Shoustikov, S. Sibley, M. E. Thompson, and S. R. Forrest, “High efficiency phosphorescent emission from organic electroluminescent devices,” *Nature*, vol. 395, pp. 151–154, 1998.
- [5] A. Endo, K. Sato, K. Yoshimura, T. Kai, A. Kawada, H. Miyazaki, and C. Adachi, “Efficient up-conversion of triplet excitons into a singlet state and its application for organic light emitting diodes,” *Appl. Phys. Lett.*, vol. 98, no. 8, p. 083302, 2011.
- [6] C. Adachi, T. Tsutsui, and S. Saito, “Blue light-emitting organic electroluminescent devices,” *Appl. Phys. Lett.*, vol. 56, no. 9, pp. 799–801, 1990.
- [7] C. Adachi, R. C. Kwong, P. Djurovich, V. Adamovich, M. A. Baldo, M. E. Thompson, and S. R. Forrest, “Endothermic energy transfer: A mechanism for generating very efficient high-energy phosphorescent emission in organic materials,” *Appl. Phys. Lett.*, vol. 79, no. 13, pp. 2082–2084, 2001.

- [8] S. Tokito, T. Iijima, Y. Suzuri, H. Kita, T. Tsuzuki, and F. Sato, "Confinement of triplet energy on phosphorescent molecules for highly-efficient organic blue-light-emitting devices," *Appl. Phys. Lett.*, vol. 83, no. 3, pp. 569–571, 2003.
- [9] H. Sasabe, E. Gonmori, T. Chiba, Y.-J. Li, D. Tanaka, S.-J. Su, T. Takeda, Y.-J. Pu, K. Nakayama, and J. Kido, "Wide-Energy-Gap Electron-Transport Materials Containing 3,5-Dipyridylphenyl Moieties for an Ultra High Efficiency Blue Organic Light-Emitting Device," *Chem. Mater.*, vol. 20, no. 19, pp. 5951–5953, 2008.
- [10] S. Schols, *Device architecture and materials for organic light-emitting devices: targeting high current densities and control of the triplet concentration*. Springer Science & Business Media, 2011.
- [11] J. Singh, "Radiative recombination and lifetime of a triplet excitation mediated by spin-orbit coupling in amorphous semiconductors," *Phys. Rev. B - Condens. Matter Mater. Phys.*, vol. 76, no. 8, pp. 1–11, 2007.
- [12] T. Förster, "Transfer mechanisms of electronic excitation energy," *Radiat. Res. Suppl.*, vol. 2, pp. 326–339, 1960.
- [13] D. L. Dexter, "A theory of sensitized luminescence in solids," *J. Chem. Phys.*, vol. 21, no. 5, pp. 836–850, 1953.
- [14] R. H. Fowler and L. Nordheim, "Electron emission in intense electric fields," *Proc. R. Soc. Lond. A*, vol. 119, no. 781, pp. 173–181, 1928.
- [15] O. W. Richardson, "Electron emission from metals as a function of temperature," *Phys. Rev.*, vol. 23, no. 2, pp. 153–155, 1924.
- [16] W. Schottky, "Vereinfachte und erweiterte Theorie der Randschicht-gleichrichter,"

- Zeitschrift für Phys. A Hadron. Nucl.*, vol. 118, no. 9, pp. 539–592, 1942.
- [17] P. N. Murgatroyd, “Theory of space-charge-limited current enhanced by Frenkel effect,” *J. Phys. D. Appl. Phys.*, vol. 3, no. 2, pp. 151–156, 1970.
- [18] P. Mark and W. Helfrich, “Space-charge-limited currents in organic crystals,” *J. Appl. Phys.*, vol. 33, no. 1, pp. 205–215, 1962.
- [19] S. L. M. Van Mensfoort, V. Shabro, R. J. De Vries, R. A. J. Janssen, and R. Coehoorn, “Hole transport in the organic small molecule material  $\alpha$ -NPD: Evidence for the presence of correlated disorder,” *J. Appl. Phys.*, vol. 107, no. 11, p. 113710, 2010.
- [20] J.-S. Kim, M. Granström, R. H. Friend, N. Johansson, W. R. Salaneck, R. Daik, W. J. Feast, and F. Cacialli, “Indium-tin oxide treatments for single- and double-layer polymeric light-emitting diodes: The relation between the anode physical, chemical, and morphological properties and the device performance,” *J. Appl. Phys.*, vol. 84, no. 12, pp. 6859–6870, 1998.
- [21] C. C. I. Wu, C. C. I. Wu, J. C. Sturm, and A. Kahn, “Surface modification of indium tin oxide by plasma treatment: An effective method to improve the efficiency, brightness, and reliability of organic light emitting devices,” *Appl. Phys. Lett.*, vol. 70, no. 11, pp. 1348–1350, 1997.
- [22] S. Fujita, T. Sakamoto, K. Ueda, K. Ohta, and S. Fujita, “Surface treatment of indium-tin-oxide substrates and its effects on initial nucleation processes of diamine films,” *Jpn. J. Appl. Phys.*, vol. 36, no. 1 A, pp. 350–353, 1997.
- [23] J. S. Kim, F. Cacialli, and R. Friend, “Surface conditioning of indium-tin oxide



- anodes for organic light-emitting diodes,” in *Thin Solid Films*, 2003, vol. 445, no. 2, pp. 358–366.
- [24] A. Köhler and H. Bässler, “Fundamentals of Organic Semiconductor Devices,” in *Electronic Processes in Organic Semiconductors*, John Wiley and Sons, 2015, pp. 307–388.
- [25] M. Zhu and C. Yang, “Blue fluorescent emitters: Design tactics and applications in organic light-emitting diodes,” *Chem. Soc. Rev.*, vol. 42, no. 12, pp. 4963–4976, 2013.
- [26] D. H. Huh, G. W. Kim, G. H. Kim, C. Kulshreshtha, and J. H. Kwon, “High hole mobility hole transport material for organic light-emitting devices,” *Synth. Met.*, vol. 180, no. 15, pp. 79–84, 2013.
- [27] W. Y. Hung, T. H. Ke, Y. T. Lin, C. C. Wu, T. H. Hung, T. C. Chao, K. T. Wong, and C. I. Wu, “Employing ambipolar oligofluorene as the charge-generation layer in time-of-flight mobility measurements of organic thin films,” *Appl. Phys. Lett.*, vol. 88, no. 6, p. 064102, 2006.
- [28] J. W. Kang, D. S. Lee, H. D. Park, Y. S. Park, J. W. Kim, W. I. Jeong, K. M. Yoo, K. Go, S. H. Kim, and J. J. Kim, “Silane- and triazine-containing hole and exciton blocking material for high-efficiency phosphorescent organic light emitting diodes,” *J. Mater. Chem.*, vol. 17, no. 35, pp. 3714–3719, 2007.
- [29] M. Gmelch, H. Thomas, F. Fries, and S. Reineke, “Programmable transparent organic luminescent tags,” *Sci. Adv.*, vol. 5, no. 2, p. eaau7310, 2019.
- [30] L. Xiao, Z. Chen, B. Qu, J. Luo, S. Kong, Q. Gong, and J. Kido, “Recent Progresses

- on Materials for Electrophosphorescent Organic Light-Emitting Devices,” *Adv. Mater.*, vol. 23, no. 8, pp. 926–952, 2011.
- [31] C. Hosokawa, H. Higashi, H. Nakamura, and T. Kusumoto, “Highly efficient blue electroluminescence from a distyrylarylene emitting layer with a new dopant,” *Appl. Phys. Lett.*, vol. 67, p. 3853, 1995.
- [32] M.-H. Tsai, Y.-H. Hong, C.-H. Chang, H.-C. Su, C.-C. Wu, A. Matoliukstyte, J. Simokaitiene, S. Grigalevicius, J. V. Grazulevicius, and C.-P. Hsu, “3-(9-Carbazolyl)carbazoles and 3,6-Di(9-carbazolyl)carbazoles as Effective Host Materials for Efficient Blue Organic Electrophosphorescence,” *Adv. Mater.*, vol. 19, no. 6, pp. 862To – 866, 2007.
- [33] X. Ren, J. Li, R. J. Holmes, P. I. Djurovich, S. R. Forrest, and M. E. Thompson, “Ultrahigh Energy Gap Hosts in Deep Blue Organic Electrophosphorescent Devices,” *Chem. Mater.*, vol. 16, no. 23, pp. 4743–4747, 2004.
- [34] J. C. Deaton, M. E. Kondakova, D. J. Giesen, W. J. Begley, and D. Y. Kondakov, “Hybrid oled with fluorescent and phosphorescent layers,” US Patent: US020080286610A1, 2008.
- [35] I. Tanaka, Y. Tabata, and S. Tokito, “Förster and Dexter energy-transfer processes in fluorescent BA1q thin films doped with phosphorescent Ir(ppy)<sub>3</sub> molecules,” *J. Appl. Phys.*, vol. 99, no. 7, p. 073501, 2006.
- [36] J. H. Jou, S. Kumar, A. Agrawal, T. H. Li, and S. Sahoo, “Approaches for fabricating high efficiency organic light emitting diodes,” *J. Mater. Chem. C*, vol. 3, no. 13, pp. 2974–3002, 2015.

- [37] C. Hosokawa, H. Tokailin, H. Higashi, and T. Kusumoto, "Electroluminescence of distyrylbenzene derivatives," *Acta Polytech. Scand. Appl. Phys. Ser.*, no. 170, pp. 219–222, 1990.
- [38] H. Higashi, C. Hosokawa, H. Tokailin, and T. Kusumoto, "Special Articles on Organic and Inorganic Optical Materials. Studies on Emitting Materials of Organic EL Cells.," *Nippon KAGAKU KAISHI*, vol. 10, pp. 1162–1167, 1992.
- [39] C. Hosokawa, H. Tokailin, H. Higashi, and T. Kusumoto, "Electroluminescence device," European Patent 0373582A1, 1990.
- [40] F.-I. Wu, P.-I. Shih, M.-C. Yuan, A. K. Dixit, C.-F. Shu, Z.-M. Chung, and E. W.-G. Diau, "Novel distyrylcarbazole derivatives as hole-transporting blue emitters for electroluminescent devices," *J. Mater. Chem.*, vol. 15, no. 44, pp. 4753–4760, 2005.
- [41] C. Hosokawa, H. Tokailin, H. Higashi, and T. Kusumoto, "Transient electroluminescence from hole transporting emitting layer in nanosecond region," *Appl. Phys. Lett.*, vol. 63, no. 10, pp. 1322–1324, 1993.
- [42] N. Liu, W. X. Shi, Y. M. Zhou, and X. A. Cao, "Impact of Dopant Aggregation on the EL of Blue Fluorescent Host-Dopant Emitters," *IEEE Electron Device Lett.*, vol. 40, no. 5, pp. 750–753, 2019.
- [43] Q. Du, W. Wang, S. Li, D. Zhang, W. Li, and W. Zheng, "Study on blue organic light-emitting diodes doped with 4,4'-bis (9-ethyl-3carbazovinylylene)-1,1'-biphenyl in various host materials," *Opt. Commun.*, vol. 366, pp. 253–259, 2016.
- [44] B. M. Lee, H. H. Yu, Y. H. Kim, N. H. Kim, J. A. Yoon, W. Y. Kim, and P. Mascher, "Highly efficient blue organic light-emitting diodes using dual emissive layers with

- host-dopant system,” *J. Photonics Energy*, vol. 3, no. 1, p. 033598, 2013.
- [45] B. M. Lee, H. H. Yu, Y. H. Kim, N. H. Kim, J. A. Yoon, P. Mascher, and W. Y. Kim, “Highly efficient blue organic light-emitting diodes using dual emissive layers with host-dopant system,” in *Photonics North 2012*, 2012, p. 841221.
- [46] G. He, “Organic Semiconductor Electroluminescent Materials,” in *Organic optoelectronic materials*, Lecture No., Y. Li, Ed. Springer, Cham, 2015, pp. 241–302.
- [47] Y. Kawamura, K. Goushi, J. Brooks, J. J. Brown, H. Sasabe, and C. Adachi, “100% phosphorescence quantum efficiency of Ir (III) complexes in organic semiconductor films,” *Appl. Phys. Lett.*, vol. 86, no. 7, pp. 1–3, 2005.
- [48] Q. Wang, J. Ding, D. Ma, Y. Cheng, L. Wang, X. Jing, and F. Wang, “Harvesting Excitons Via Two Parallel Channels for Efficient White Organic LEDs with Nearly 100% Internal Quantum Efficiency: Fabrication and Emission-Mechanism Analysis,” *Adv. Funct. Mater.*, vol. 19, no. 1, pp. 84–95, 2009.
- [49] T. Tsuzuki and S. Tokito, “Highly Efficient and Low-Voltage Phosphorescent Organic Light-Emitting Diodes Using an Iridium Complex as the Host Material,” *Adv. Mater.*, vol. 19, no. 2, pp. 276–280, 2007.
- [50] M.-F. Wu, S.-J. Yeh, C.-T. Chen, H. Murayama, T. Tsuboi, W. S. Li, I. Chao, S. W. Liu, and J.-K. Wang, “The Quest for High-Performance Host Materials for Electrophosphorescent Blue Dopants,” *Adv. Funct. Mater.*, vol. 17, no. 12, pp. 1887–1895, 2007.
- [51] C. Adachi, M. A. Baldo, M. E. Thompson, and S. R. Forrest, “Nearly 100% internal

- phosphorescence efficiency in an organic light emitting device,” *J. Appl. Phys.*, vol. 90, no. 10, pp. 5048–5051, 2001.
- [52] J. Lee, J.-I. Lee, J. Y. Lee, and H. Y. Chu, “Stable efficiency roll-off in blue phosphorescent organic light-emitting diodes by host layer engineering,” *Org. Electron.*, vol. 10, no. 8, pp. 1529–1533, 2009.
- [53] S. W. Liu, X. W. Sun, and H. V. Demir, “Graded-host phosphorescent light-emitting diodes with high efficiency and reduced roll-off,” *AIP Adv.*, vol. 2, no. 1, p. 012192, 2012.
- [54] S. J. Lee, S. E. Lee, D. H. Lee, J. R. Koo, H. W. Lee, S. S. Yoon, J. Park, and Y. K. Kim, “Effect of broad recombination zone in multiple quantum well structures on lifetime and efficiency of blue organic light-emitting diodes,” *Jpn. J. Appl. Phys.*, vol. 53, no. 10, p. 101601, 2014.
- [55] J. S. Kang, J. A. Yoon, S. Il Yoo, J. W. Kim, S. Yi, F. Zhu, K. W. Cheah, and W. Y. Kim, “Luminous efficiency enhancement in blue phosphorescent organic light-emitting diodes with an electron confinement layers,” *Opt. Mater. (Amst.)*, vol. 47, pp. 78–82, 2015.
- [56] J. Liu, J. Wang, S. Huang, H.-A. Chen, and G. He, “Improved efficiency of blue phosphorescence organic light-emitting diodes with irregular stepwise-doping emitting layers,” *Phys. status solidi*, vol. 210, no. 3, pp. 489–493, 2013.
- [57] S. E. Lee, H. W. Lee, S. J. Lee, J. R. Koo, D. H. Lee, H. J. Yang, H. J. Kim, S. S. Yoon, and Y. K. Kim, “Effect of stepwise doping on lifetime and efficiency of blue and white phosphorescent organic light emitting diodes,” *J. Nanosci. Nanotechnol.*,

- vol. 15, no. 2, pp. 1456–1459, 2015.
- [58] L. Yang, X. Wang, Z. Kou, and C. Ji, “Improved efficiency in blue phosphorescent organic light-emitting diodes by the stepwise doping structure,” *Opt. Mater. (Amst)*., vol. 66, pp. 399–403, 2017.
- [59] Q. Wang, C. L. Ho, Y. Zhao, D. Ma, W. Y. Wong, and L. Wang, “Reduced efficiency roll-off in highly efficient and color-stable hybrid WOLEDs: The influence of triplet transfer and charge-transport behavior on enhancing device performance,” *Org. Electron.*, vol. 11, no. 2, pp. 238–246, 2010.
- [60] Y. Zhang, J. Lee, and S. R. Forrest, “Tenfold increase in the lifetime of blue phosphorescent organic light-emitting diodes,” *Nat. Commun.*, vol. 5, p. 5008, 2014.
- [61] N. Chopra, J. Lee, Y. Zheng, S. Eom, J. Xue, F. So, N. Chopra, J. Lee, Y. Zheng, S. Eom, and J. Xue, “High efficiency blue phosphorescent organic light-emitting device High efficiency blue phosphorescent organic light-emitting device,” *Appl. Phys. Lett.*, vol. 93, no. 14, p. 143307, 2008.
- [62] X. Gong, J. C. Ostrowski, G. C. Bazan, D. Moses, and A. J. Heeger, “Red electrophosphorescence from polymer doped with iridium complex,” *Appl. Phys. Lett.*, vol. 81, no. 20, pp. 3711–3713, 2002.
- [63] M. A. Baldo, C. Adachi, and S. R. Forrest, “Transient analysis of organic electrophosphorescence. II. Transient analysis of triplet-triplet annihilation,” *Phys. Rev. B - Condens. Matter Mater. Phys.*, vol. 62, no. 16, pp. 10967–10977, 2000.
- [64] D. F. O’Brien, M. A. Baldo, M. E. Thompson, and S. R. Forrest, “Improved energy transfer in electrophosphorescent devices,” *Appl. Phys. Lett.*, vol. 74, no. 3, pp. 442–

- 444, 1999.
- [65] V. Cleave, G. Yahioglu, P. Le Barny, R. H. Friend, and N. Tessler, “Harvesting Singlet and Triplet Energy in Polymer LEDs,” *Adv. Mater.*, vol. 11, no. 4, pp. 285–288, 1999.
- [66] S. E. Lee, H. W. Lee, D. H. Lee, H. J. Yang, S. J. Lee, J. R. Koo, H. J. Kim, S. S. Yoon, and Y. K. Kim, “Enhanced hybrid blue organic light emitting diodes with a multi-emitting layer using fluorescent and phosphorescent emitters,” *Mol. Cryst. Liq. Cryst.*, vol. 601, no. 1, pp. 223–230, 2014.
- [67] S. E. Lee, H. W. Lee, J. W. Lee, K. M. Hwang, S. N. Park, S. S. Yoon, and Y. K. Kim, “Optimization of hybrid blue organic light-emitting diodes based on singlet and triplet exciton diffusion length,” *Jpn. J. Appl. Phys.*, vol. 54, no. 6S1, p. 06FG09, 2015.
- [68] G. W. Kim, H. W. Bae, R. Lampande, I. J. Ko, J. H. Park, C. Y. Lee, and J. H. Kwon, “Highly efficient single-stack hybrid cool white OLED utilizing blue thermally activated delayed fluorescent and yellow phosphorescent emitters,” *Sci. Rep.*, vol. 8, p. 16263, 2018.
- [69] T. Zheng and W. C. H. Choy, “High Efficiency Blue Organic LEDs Achieved By an Integrated Fluorescence-Interlayer-Phosphorescence Emission Architecture,” *Adv. Funct. Mater.*, vol. 20, no. 4, pp. 648–655, 2010.
- [70] H. S. Bang, H. S. Jeong, D. C. Choo, and T. W. Kim, “Enhancement of the luminance efficiency in blue organic light-emitting devices fabricated utilizing a hybrid phosphorescence and fluorescence emitting layer,” in *Thin Solid Films*, 2011,

- vol. 519, no. 15, pp. 5249–5252.
- [71] B. M. Lee, N. H. Kim, J. A. Yoon, S. E. Lee, Y. K. Kim, W. Y. Kim, and P. Mascher, “Luminescence characteristics of hybrid dual emitting layers in blue organic light-emitting diodes by controlling the fluorescent doping concentration,” *J. Lumin.*, vol. 148, pp. 72–78, 2014.
- [72] B. M. Lee, J. Kim, G. J. Yun, W. Y. Kim, and P. Mascher, “Study on hybrid blue organic light emitting diodes with step controlled doping profiles in phosphorescent emitting layer,” *Opt. Mater. (Amst.)*, vol. 86, pp. 498–504, 2018.
- [73] B. M. Lee, S. Il Yoo, J. S. Kang, J. A. Yoon, W. Y. Kim, and P. Mascher, “Hybrid blue organic light emitting diodes with fluorescent and phosphorescent emitters along with an interlayer,” *Sci. Adv. Mater.*, vol. 8, no. 2, pp. 301–306, 2016.
- [74] F. Huang, P.-I. Shih, C.-F. Shu, Y. Chi, and A. K.-Y. Jen, “Highly Efficient Polymer White-Light-Emitting Diodes Based on Lithium Salts Doped Electron Transporting Layer,” *Adv. Mater.*, vol. 21, no. 3, pp. 361–365, 2009.
- [75] M. Uchida, C. Adachi, T. Koyama, and Y. Taniguchi, “Charge carrier trapping effect by luminescent dopant molecules in single-layer organic light emitting diodes,” *J. Appl. Phys.*, vol. 86, no. 3, pp. 1680–1687, 1999.
- [76] D. Monroe, “Hopping in exponential band tails,” *Phys. Rev. Lett.*, vol. 54, no. 2, pp. 146–149, 1985.
- [77] V. I. Arkhipov, P. Heremans, E. V. Emelianova, G. J. Adriaenssens, and H. Bässler, “Charge carrier mobility in doped semiconducting polymers,” *Appl. Phys. Lett.*, vol. 82, no. 19, pp. 3245–3247, 2003.



- [78] S.-W. Feng and H.-C. Wang, "X Carrier Transport and Recombination Dynamics in Disordered Organic Light Emitting Diodes."
- [79] Y. Y. Yimer, P. A. Bobbert, and R. Coehoorn, "Charge transport in disordered organic host-guest systems: effects of carrier density and electric field," *J. Phys. Condens. Matter*, vol. 20, no. 33, p. 335204, 2008.
- [80] X. Zhang, F. Wei, X. Liu, W. Zhu, X. Jiang, and Z. Zhang, "Study on energy relation between blue and red emissive layer of organic light-emitting diodes by inserting spacer layer," *Thin Solid Films*, vol. 518, no. 23, pp. 7119–7123, 2010.
- [81] Y. S. Seo and D. G. Moon, "Highly efficient white light-emitting devices by direct excitation of phosphorescent guest molecules," *J. Phys. D. Appl. Phys.*, vol. 43, no. 30, p. 305101, 2010.
- [82] W. Brütting, S. Berleb, and A. G. Mückl, "Device physics of organic light-emitting diodes based on molecular materials," *Org. Electron.*, vol. 2, no. 1, pp. 1–36, 2001.
- [83] T.-Y. Cheng *et al.*, "Carrier transport and Recombination Mechanism in Blue phosphorescent organic Light-emitting Diode with Hosts Consisting of Cabazole- and triazole-Moiety," *Sci. Rep.*, vol. 9, p. 3654, 2019.
- [84] Y.-H. Kim, W. Y. Kim, and C.-B. Moon, "Energy transfer between host and dopant molecules in blue organic light-emitting devices," *J. Appl. Phys.*, vol. 110, no. 3, p. 034501, 2011.
- [85] R. J. Holmes, B. W. D'Andrade, S. R. Forrest, X. Ren, J. Li, and M. E. Thompson, "Efficient, deep-blue organic electrophosphorescence by guest charge trapping," *Appl. Phys. Lett.*, vol. 83, no. 18, pp. 3818–3820, 2003.

- [86] V. Adamovich, J. Brooks, A. Tamayo, A. M. Alexander, P. I. Djurovich, B. W. D'Andrade, C. Adachi, S. R. Forrest, and M. E. Thompson, "High efficiency single dopant white electrophosphorescent light emitting diodes," *New J. Chem.*, vol. 26, no. 9, pp. 1171–1178, 2002.
- [87] S. Il Yoo, J. A. Yoon, N. H. Kim, J. W. Kim, J. S. Kang, C.-B. Moon, and W. Y. Kim, "Improvement of efficiency roll-off in blue phosphorescence OLED using double dopants emissive layer," *J. Lumin.*, vol. 160, pp. 346–350, 2015.
- [88] S. H. Rhee, C. S. Kim, M. Song, K. B. Chung, and S. Y. Ryu, "Effects of position of exciton-blocking layer on characteristics of blue phosphorescent organic light-emitting diodes," *ECS Solid State Lett.*, vol. 3, no. 10, pp. R49–R52, 2014.
- [89] K. S. Yook and J. Y. Lee, "Organic Materials for Deep Blue Phosphorescent Organic Light-Emitting Diodes," *Adv. Mater.*, vol. 24, no. 24, pp. 3169–3190, 2012.
- [90] M. Berggren, O. Inganäs, G. Gustafsson, J. Rasmusson, M. R. Andersson, T. Hjertberg, and O. Wennerström, "Light-emitting diodes with variable colours from polymer blends," *Nature*, vol. 372, no. 6505, pp. 444–446, 1994.
- [91] M. C. Gather, R. Alle, H. Becker, and K. Meerholz, "On the Origin of the Color Shift in White-Emitting OLEDs," *Adv. Mater.*, vol. 19, no. 24, pp. 4460–4465, 2007.
- [92] Y. Yang and Q. Pei, "Voltage controlled two color light-emitting electrochemical cells," *Appl. Phys. Lett.*, vol. 68, no. 19, pp. 2708–2710, 1996.
- [93] B. W. D'Andrade, M. E. Thompson, and S. R. Forrest, "Controlling Exciton Diffusion in Multilayer White Phosphorescent Organic Light Emitting Devices," *Adv. Mater.*, vol. 14, no. 2, pp. 147–151, 2002.

- [94] D. J. Gaspar and E. Polikarpov, *OLED fundamentals: materials, devices, and processing of organic light-emitting diodes*. CRC press, 2015.
- [95] V. Bulović, M. A. Baldo, and S. R. Forrest, “Excitons and Energy Transfer in Doped Luminescent Molecular Organic Materials,” in *Organic Electronic Materials: Conjugated Polymers and Low Molecular Weight Organic Solids*, Springer, Berlin, Heidelberg, 2001, pp. 391–441.
- [96] V. Jankus, C.-J. Chiang, F. Dias, and A. P. Monkman, “Deep Blue Exciplex Organic Light-Emitting Diodes with Enhanced Efficiency; P-type or E-type Triplet Conversion to Singlet Excitons?,” *Adv. Mater.*, vol. 25, no. 10, pp. 1455–1459, 2013.
- [97] N. C. Giebink and S. R. Forrest, “Quantum efficiency roll-off at high brightness in fluorescent and phosphorescent organic light emitting diodes,” *Phys. Rev. B - Condens. Matter Mater. Phys.*, vol. 77, no. 23, 2008.
- [98] S. Reineke, K. Walzer, and K. Leo, “Triplet-exciton quenching in organic phosphorescent light-emitting diodes with Ir-based emitters,” *Phys. Rev. B - Condens. Matter Mater. Phys.*, vol. 75, no. 12, 2007.
- [99] D. Song, S. Zhao, Y. Luo, and H. Aziz, “Causes of efficiency roll-off in phosphorescent organic light emitting devices: Triplet-triplet annihilation versus triplet-polaron quenching,” *Appl. Phys. Lett.*, vol. 97, no. 24, p. 243304, 2010.
- [100] Y. Sun, N. C. Giebink, H. Kanno, B. Ma, M. E. Thompson, and S. R. Forrest, “Management of singlet and triplet excitons for efficient white organic light-emitting devices,” *Nature*, vol. 440, no. 7086, pp. 908–912, 2006.
- [101] P. S. Kuttipillai, S. Mukhopadhyay, A. Sokolov, K. L. Kearns, W. H. H. Woodward,

- and R. R. Lunt, "Mapping recombination profiles in single-, dual-, and mixed-host phosphorescent organic light emitting diodes," *Org. Electron.*, vol. 57, pp. 28–33, 2018.
- [102] C. H. Hsiao, J.-H. Lee, and C. A. Tseng, "Probing recombination-rate distribution in organic light-emitting devices with mixed-emitter structure," *Chem. Phys. Lett.*, vol. 427, no. 4–6, pp. 305–309, 2006.
- [103] K. S. Yook and J. Y. Lee, "Recombination zone study of phosphorescent organic light-emitting diodes with triplet mixed host emitting structure," *J. Ind. Eng. Chem.*, vol. 16, no. 2, pp. 181–184, 2010.
- [104] T. A. Beierlein, B. Ruhstaller, D. J. Gundlach, H. Riel, S. Karg, C. Rost, and W. Rieß, "Investigation of internal processes in organic light-emitting devices using thin sensing layers," *Synth. Met.*, vol. 138, no. 1–2, pp. 213–221, 2003.
- [105] H. Uoyama, K. Goushi, K. Shizu, H. Nomura, and C. Adachi, "Highly efficient organic light-emitting diodes from delayed fluorescence," *Nature*, vol. 492, no. 7428, pp. 234–238, 2012.
- [106] Y. Im, S. Y. Byun, J. H. Kim, D. R. Lee, C. S. Oh, K. S. Yook, and J. Y. Lee, "Recent Progress in High-Efficiency Blue-Light-Emitting Materials for Organic Light-Emitting Diodes," *Adv. Funct. Mater.*, vol. 27, no. 13, p. 1603007, 2017.
- [107] S. J. Cha, N. S. Han, J. K. Song, S. R. Park, Y. M. Jeon, and M. C. Suh, "Efficient deep blue fluorescent emitter showing high external quantum efficiency," *Dye. Pigment.*, vol. 120, pp. 200–207, 2015.
- [108] E. Baranoff and B. F. E. Curchod, "FIrpic: Archetypal blue phosphorescent emitter

- for electroluminescence,” *Dalton Transactions*, vol. 44, no. 18. Royal Society of Chemistry, pp. 8318–8329, 14-May-2015.
- [109] A. Endo, K. Suzuki, T. Yoshihara, S. Tobita, M. Yahiro, and C. Adachi, “Measurement of photoluminescence efficiency of Ir(III) phenylpyridine derivatives in solution and solid-state films,” *Chem. Phys. Lett.*, vol. 460, no. 1–3, pp. 155–157, 2008.
- [110] S.-C. Yeh, M.-F. Wu, C.-T. Chen, Y.-H. Song, Y. Chi, M.-H. Ho, S.-F. Hsu, and C. H. Chen, “New Dopant and Host Materials for Blue-Light-Emitting Phosphorescent Organic Electroluminescent Devices,” *Adv. Mater.*, vol. 17, no. 3, pp. 285–289, 2005.
- [111] T. Tsuboi, H. Murayama, S. J. Yeh, M. F. Wu, and C.-T. Chen, “Photoluminescence characteristics of blue phosphorescent Ir<sup>3+</sup>-compounds FIrpic and FIrN4 doped in mCP and SimCP,” *Opt. Mater. (Amst)*, vol. 31, no. 2, pp. 366–371, 2008.
- [112] S. H. Kim, J. Jang, S. J. Lee, and J. Y. Lee, “Deep blue phosphorescent organic light-emitting diodes using a Si based wide bandgap host and an Ir dopant with electron withdrawing substituents,” *Thin Solid Films*, vol. 517, no. 2, pp. 722–726, 2008.
- [113] S. Reineke, F. Lindner, G. Schwartz, N. Seidler, K. Walzer, B. Lüssem, and K. Leo, “White organic light-emitting diodes with fluorescent tube efficiency,” in *Materials Research Society Symposium Proceedings*, 2010, vol. 1212, pp. 17–22.
- [114] F. Zhao and D. Ma, “Approaches to high performance white organic light-emitting diodes for general lighting,” *Materials Chemistry Frontiers*, vol. 1, no. 10. Royal Society of Chemistry, pp. 1933–1950, 2017.

- [115] R. Meerheim, B. Lüssem, and K. Leo, “Efficiency and stability of p-i-n type organic light emitting diodes for display and lighting applications,” *Proc. IEEE*, vol. 97, no. 9, pp. 1606–1626, 2009.
- [116] L. Duan, J. Qiao, Y. Sun, and Y. Qiu, “Strategies to Design Bipolar Small Molecules for OLEDs: Donor-Acceptor Structure and Non-Donor-Acceptor Structure,” *Adv. Mater.*, vol. 23, no. 9, pp. 1137–1144, 2011.
- [117] K. Hong and J. L. Lee, “Recent developments in light extraction technologies of organic light emitting diodes,” *Electronic Materials Letters*, vol. 7, no. 2, pp. 77–91, 2011.
- [118] C. Adachi, “Third-generation organic electroluminescence materials,” *Japanese Journal of Applied Physics*, vol. 53, no. 6, Japan Society of Applied Physics, 2014.
- [119] Y. Tao, K. Yuan, T. Chen, P. Xu, H. Li, R. Chen, C. Zheng, L. Zhang, and W. Huang, “Thermally Activated Delayed Fluorescence Materials Towards the Breakthrough of Organoelectronics,” *Adv. Mater.*, vol. 26, no. 47, pp. 7931–7958, 2014.
- [120] W. Song and J. Y. Lee, “Degradation Mechanism and Lifetime Improvement Strategy for Blue Phosphorescent Organic Light-Emitting Diodes,” *Adv. Opt. Mater.*, vol. 5, no. 9, p. 1600901, 2017.
- [121] X. Cai and S.-J. Su, “Marching Toward Highly Efficient, Pure-Blue, and Stable Thermally Activated Delayed Fluorescent Organic Light-Emitting Diodes,” *Adv. Funct. Mater.*, vol. 28, no. 43, p. 1802558, 2018.
- [122] J. Guo, Z. Zhao, and B. Z. Tang, “Purely Organic Materials with Aggregation-Induced Delayed Fluorescence for Efficient Nondoped OLEDs,” *Adv. Opt. Mater.*,

- vol. 6, no. 15, p. 1800264, 2018.
- [123] J.-H. Jou, M.-H. Wu, S.-M. Shen, H.-C. Wang, S.-Z. Chen, S.-H. Chen, C.-R. Lin, and Y.-L. Hsieh, “Sunlight-style color-temperature tunable organic light-emitting diode,” *Appl. Phys. Lett.*, vol. 95, no. 1, p. 013307, 2009.
- [124] C. W. Joo, J. Moon, J. H. Han, J. W. Huh, J. Lee, N. S. Cho, J. Hwang, H. Y. Chu, and J.-I. Lee, “Color temperature tunable white organic light-emitting diodes,” *Org. Electron.*, vol. 15, no. 1, pp. 189–195, 2014.
- [125] J.-H. Jou, H.-C. Wang, S.-M. Shen, S.-H. Peng, M.-H. Wu, S.-H. Chen, and P.-H. Wu, “Highly efficient color-temperature tunable organic light-emitting diodes,” *J. Mater. Chem.*, vol. 22, no. 16, pp. 8117–8120, 2012.
- [126] J.-H. Jou, C.-Y. Hsieh, J.-R. Tseng, S.-H. Peng, Y.-C. Jou, J. H. Hong, S.-M. Shen, M.-C. Tang, P.-C. Chen, and C.-H. Lin, “Candle Light-Style Organic Light-Emitting Diodes,” *Adv. Funct. Mater.*, vol. 23, no. 21, pp. 2750–2757, 2013.
- [127] J. Lee, T. W. Koh, H. Cho, S. Hofmann, S. Reineke, J.-H. Lee, J.-I. Lee, S. Yoo, K. Leo, and M. C. Gather, “Color temperature tuning of white organic light-emitting diodes via spatial control of micro-cavity effects based on thin metal strips,” *Org. Electron.*, vol. 26, pp. 334–339, 2015.
- [128] W. J. M. van Bommel, “Non-visual biological effect of lighting and the practical meaning for lighting for work,” *Appl. Ergon.*, vol. 37, no. 4, pp. 461–466, 2006.
- [129] R. Kuller and L. Wetterberg, “Melatonin, cortisol, EEG, ECG and subjective comfort in healthy humans: Impact of two fluorescent lamp types at two light intensities,” *Int. J. Light. Res. Technol.*, vol. 25, no. 2, pp. 71–80, 1993.

- [130] P. R. Mills, S. C. Tomkins, and L. J. Schlangen, “The effect of high correlated colour temperature office lighting on employee wellbeing and work performance,” *J. Circadian Rhythms*, vol. 5, no. 1, p. 2, 2007.
- [131] S. M. Pauley, “Lighting for the human circadian clock: Recent research indicates that lighting has become a public health issue,” *Med. Hypotheses*, vol. 63, no. 4, pp. 588–596, 2004.
- [132] G. C. Brainard, B. A. Richardson, T. S. King, and R. J. Reiter, “The influence of different light spectra on the suppression of pineal melatonin content in the syrian hamster,” *Brain Res.*, vol. 294, no. 2, pp. 333–339, 1984.
- [133] S. W. Lockley, G. C. Brainard, and C. A. Czeisler, “High Sensitivity of the Human Circadian Melatonin Rhythm to Resetting by Short Wavelength Light,” *J. Clin. Endocrinol. Metab.*, vol. 88, no. 9, pp. 4502–4502, 2003.
- [134] S. L. Lai, S. L. Tao, M. Y. Chan, T. W. Ng, M. F. Lo, C. S. Lee, X. H. Zhang, and S. T. Lee, “Efficient white organic light-emitting devices based on phosphorescent iridium complexes,” *Org. Electron.*, vol. 11, no. 9, pp. 1511–1515, 2010.
- [135] J.-H. Jou, J.-R. Tseng, K.-Y. Tseng, W.-B. Wang, Y.-C. Jou, S.-M. Shen, Y.-L. Chen, W.-Y. Hung, S.-Z. Chen, T.-Y. Ding, and H.-C. Wang, “High-efficiency host free deep-blue organic light-emitting diode with double carrier regulating layers,” *Org. Electron.*, vol. 13, no. 12, pp. 2893–2897, 2012.
- [136] J. H. Seo, J. S. Park, S. J. Lee, B. M. Seo, K. H. Lee, J. K. Park, S. S. Yoon, and Y. K. Kim, “Codoped spacer ratio effect of hybrid white organic light-emitting diodes,” *Curr. Appl. Phys.*, vol. 11, no. 3, pp. 564–567, 2011.



- [137] J.-H. Jou, S. Kumar, M. Singh, Y.-H. Chen, C.-C. Chen, and M.-T. Lee, “Carrier Modulation Layer-Enhanced Organic Light-Emitting Diodes,” *Molecules*, vol. 20, no. 7, pp. 13005–13030, 2015.
- [138] Y. Xia, O. Y. Wan, and K. W. Cheah, “OLED for human centric lighting,” *Opt. Mater. Express*, vol. 6, no. 6, p. 1905, 2016.